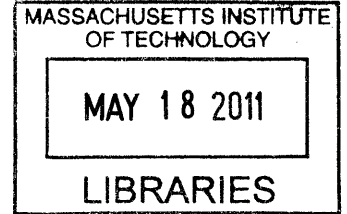# Thermal Conductivity from First-Principles in Bulk, Disordered, and Nanostructured Materials

by

Jivtesh Garg

B.Tech., Mechanical Engineering
Indian Institute of Technology, Chennai, 1999

M.S., Mechanical Engineering
University of Minnesota, 2002

Submitted to the Department of Mechanical Engineering
in partial fulfillment of the requirements for the degree of

Doctor of Philosophy in Mechanical Engineering

at the

MASSACHUSETTS INSTITUTE OF TECHNOLOGY

February 2011

Author . . . .
Department of Mechanical Engineering
Jan 27, 2011

Certified by . . . .
. . . .
Nicola Marzari
Professor of Materials Science and Engineering
Thesis Supervisor

Accepted by . . . .
. . .
David Hardt
Ralph E. and Eloise F. Cross Professor of Mechanical Engneering
Chairman, Department Committee on Graduate Students

Thermal Conductivity from First-Principles in Bulk, Disordered, and Nanostructured Materials

by

Jivtesh Garg

Abstract

Thermal conductivity is an important transport property that plays a vital role in applications such as high efficiency thermoelectric devices as well as in thermal management of electronics. We present a first-principles approach based on density-functional perturbation theory (DFPT) to predict the thermal conductivity of semiconducting materials. Heat in these materials is conducted by lattice vibrations (phonons). The most important ingredients in the prediction of thermal conductivity in such materials are the second- and third-order derivatives of energy with respect to atomic displacements. Typically, these are derived using empirical potentials which do not produce the correct harmonic and anharmonic behavior, necessary to accurately compute phonon frequencies and relaxation times. We obtain these derivatives from quantum mechanics through DFPT, and use them along with the solution of the phonon Boltzmann transport equation to predict thermal conductivity. We apply the approach to isotopically pure silicon and germanium as well as materials with disorder such as silicon-germanium alloys and show how this leads to excellent agreement between computed and experimentally measured values. The approach is also applied to predict thermal transport in nanostructured materials such as superlattices.

In isotopically pure silicon and germanium, phonons scatter only through the three-phonon anharmonic scattering processes. Using the single-mode relaxation time approximation and estimating the scattering rate of these processes based on the force constants derived from DFPT, excellent agreement is obtained between computed and measured values of thermal conductivity. The approach predicts that in isotopically pure silicon, more than 90% of the heat is conducted by phonons of mean free path larger than 40 nm, providing avenues to lower thermal conductivity through nanostructuring.

To predict thermal transport in disordered silicon-germanium alloys of any composition, we make use of the phonon modes of an average crystal which has the two atom unit cell and average mass and force constants appropriate for that composition. The disorder is taken to lead to elastic two-phonon scattering in addition to the three-phonon scattering present in pure materials. The idea was first proposed

by Abeles in 1963; however we are able to compute all the ingredients from first-principles. The force constants for the composition $Si_{0.5}Ge_{0.5}$ are obtained by using the virtual crystal where the atomic potential at each site is an average of the silicon and germanium potentials. We demonstrate how this approach can be used to guide design of nanostructured materials to further lower thermal conductivity.

In superlattices, we again use the virtual crystal to obtain the second-order and third-force constants. Computed thermal conductivity is found to lower with increase in superlattice period; however, the predicted values are higher than experimentally measured values, and we discuss the cause of this discrepancy. In the limit of very small period superlattice, we find that thermal conductivity can increase dramatically and can exceed that of isotopically pure silicon. This cause of this unexpected result is discussed, and its implications for high thermal conductivity materials, important for applications in thermal management of electronics.

Thesis Supervisor: Nicola Marzari
Title: Professor of Materials Science and Engineering

Acknowledgments

This work would not have been possible without the support of many people and I wish to express my thanks to all of them.

First and foremost I express my deep gratitude towards my thesis supervisor Prof. Nicola Marzari for his strong support and kindness throughout the course of this work. I immensely enjoyed working in his group and am deeply thankful to him for giving me the opportunity to pursue research on a problem that I was keenly interested in. He fully inspired and motivated me and helped me develop a better understanding of my research field. I also thank my thesis committee members Prof. Gang Chen and Prof. David M. Parks for their insightful comments and suggestions that helped me think in new ways about thermal conduction at nanoscale. Discussions with Prof. Marco Fornari contributed greatly to my research and I am thankful to him. I owe a special thanks to Dr. Nicola Bonini from whom I had the opportunity to learn a great deal about phonon calculations and to Dr. Boris Kozinsky and for helpful discussions on several subtle aspects of the work. I am also thankful to Prof. Giulia Galli and Dr. Davide Donadio for the opportunity to work with them for a few weeks at UC Davis. Working with them allowed me to learn the application of molecular dynamics to thermal conduction and made me aware of certain unique and challenging aspects of thermal conductivity in disordered systems. I thank Prof. G.P. Srivastava for showing keen interest in my work and for answering many of my questions. I also greatly benefited by working with the members of the Quasiamore group and am grateful to them - Dr. Francesca Baletto, Dr. Timo Thonhauser, Dr. Brandon Wood, Dr. Arash Mostofi, Dr. Young-Su Lee, Dr. Ismaila Dabo, Dr. Heather Kulik, Dr. Davide Ceresoli, Dr. Oliviero Andreussi, Dr. Samed Halilov, Dr. Xiaofeng Qian, Dr. Dmitri Volja, Dr. Andrea Feretti, Dr. Nicholas E. Singh Miller, Elise Li, Sejoong Kim, Nicolas Poilvert, Nicéphore Bonnet and Matteo Salvetti - for their positive energy, great enthusiasm and friendliness. I also owe deep thanks to Kathryn Simons for her constant help and support.

I give many thanks to my parents, my brother and my sister for their useful advice

and their constant encouragement.

Finally, I thank all my friends and colleagues for being a source of great joy and happiness during the years at MIT.

Contents

List of Figures

9

12

13

14

List of Tables

Chapter 1

Introduction

Thermal conductivity plays a critical role in many applications such as microelectronic and nanoelectronic devices [1] and in thermoelectric refrigeration and power generation [2]. In nanoelectronics, for example, the progression of Moore's law, which predicts that the number of transistors that can be placed inexpensively on an integrated circuit doubles every two years, has led to increasing chip power dissipation and heat chip heat fluxes have been predicted to exceed 150 W/cm^2 [3, 4]. This, along with the non-uniform distribution of chip power dissipation, creates localized hot spots, that reduce device reliability and performance. High thermal conductivity leads to improved heat spreading thereby reducing the hot spot temperatures, and is thus critically important for thermal management of electronics.

Thermoelectric devices allow direct conversion of heat rejected to environment as waste energy into useful electric power and can thus play a key role in achieving higher energy efficiency. The energy conversion efficiency of a thermoelectric device is often characterized by the dimensionless figure of merit $ZT = S^2\sigma T/k$ [5] where S, σ, k and T are the Seebeck coefficient, electrical conductivity, thermal conductivity and average operating temperature, respectively. The energy conversion efficiency η [5] is related to the figure of merit ZT as

$$\eta = \frac{\sqrt{1 + ZT} - 1}{\sqrt{1 + ZT} + T_C/T_H}(1 - \frac{T_C}{T_H})$$

(1.1)

19

where T_H and T_C are the hot-end and cold-end temperatures, respectively, across a thermoelectric device. Thus for a T_H=750 K and T_C=300 K, a material with a ZT of 1 would have a maximum thermoelectric energy conversion efficiency of 14%, while for ZT=3, the conversion efficiency increases to about 25%. For several decades, however, the ZT in bulk semiconducting materials was found to be significantly lower than the above values, making these thermoelectric devices too inefficient to be of any practical use. For example, the ZT in heavily doped n-type single crystal silicon is about 0.01 at room temperature [6] while that of bulk p-type silicon-germanium alloys is measured to be about 0.62 [7].

Nanotechnology has led to renewed interest in thermoelectrics. High thermal conductivity in thermoelectric devices leads to parasitic heat loss that reduces the energy conversion efficiency. Figure of merit ZT is therefore inversely proportional to thermal conductivity and lower thermal conductivity leads to higher ZT. Heat in semiconducting materials is conducted by quantized lattice vibrations called phonons and one of the most promising avenues to increase ZT beyond ~ 1 has been to reduce thermal conductivity through enhanced phonon scattering following alloying, surface roughening or nanostructuring [8, 9, 10]. For example, reduced thermal conductivity led to an improved ZT of about 0.6 in surface-rough silicon nanowires [10], 60 times higher than bulk silicon. Similarly ZT of p-type Bi_2Te_3/Sb_2Te_3 superlattice was measured to be about 2.4 [11], a sharp increase over the corresponding bulk materials. In silicon-germanium alloys, the thermal conductivity is significantly lower than both silicon and germanium due to disorder. Thermal conductivity below the bulk alloy value has been achieved by the use of different approaches such as alloy nanocomposites and inclusion of nanoparticles. For example, embedding [12] ErAs nanoparticles in $In_{0.53}Ga_{0.47}As$ was found to result in a thermal conductivity reduction of nearly a factor of 2 below the alloy limit and a corresponding increase in the thermoelectric figure of merit by a factor of 2. A combination of above approaches could be used to design a high ZT material.

An understanding of the relative importance of different approaches in scattering phonons is important for designing materials with reduced thermal conductivity. The

parameter that typically determines if nanostructuring can lead to lower thermal conductivity in a material is the phonon mean free path defined as the product of phonon group velocity and phonon relaxation time. If significant heat is conducted in a material by phonons of mean free path of about a micron (1μm) or larger then the thermal conductivity can be reduced by introducing additional scattering mechanisms like grain boundaries at nanometer length scales. Costs associated with designing a nanostructured material with lower thermal conductivity can be reduced significantly if these phonon mean free paths are known *a priori*.

The work in this thesis is focussed on accurate prediction of thermal conductivity in pure, disordered and nanostructured materials using a first-principles approach based on density-functional perturbation theory [13, 14, 15] and phonon Boltzmann equation (PBE) [16]. The approach involves determining fundamental properties such as phonon frequencies, group velocities, Bose-Einstein populations and phonon relaxation times from first-principles to compute thermal conductivity. Through explicit knowledge of the above quantities, important parameters such as phonon mean free paths are determined and these are then used to provide guidelines for the design of low thermal conductivity materials, important for applications such as thermo-electrics.

In this work, the relaxation time of a phonon mode is computed based on its scattering through all possible channels over the entire Brillouin zone. Such a detailed description of the scattering processes can be used to gain insight into atomic configurations that lead to reduced phonon-phonon scattering and higher phonon relaxation times. Through above this work also provides ways to achieve higher thermal conductivity, important for thermal management of electronics.

The most important ingredients that determine the thermal conductivity in semi-conducting materials are the second-order and third-order derivatives of energy with respect to atomic displacements also called the second-order (or harmonic) and third-order (or anharmonic) interatomic force constants (IFCs). Second-order (harmonic) force constants determine phonon frequencies, group velocities and Bose-Einstein populations, while third-order (anharmonic) force constants are needed to estimate the

phonon relaxation times based on phonon-phonon scattering processes. Accurate prediction of thermal conductivity is often made difficult due to the challenge involved in accurately estimating these interatomic force constants.

In the past empirical potentials have been used to obtain the harmonic (second-order) and anharmonic (third-order) force constants. These empirical interatomic potentials (EIP) are typically fit to experimental properties of materials such as second-order elastic constants and crystal structure. However the potentials are almost never fit to any property related to the anharmonicity of the crystal. Broido et al. [17] computed the thermal conductivity of silicon using force constants derived from several different empirical potentials, including, Stillinger-Weber [18], Tersoff [19] and environment dependent [20] potentials. They reported that none of the potentials provided satisfactory agreement with experimentally measured values of thermal conductivity due to the incorrect anharmonic behaviour.

Molecular dynamics simulations have also been used to study thermal transport [21]. In these simulations as well, interatomic interactions are calculated with the use of empirical interatomic potentials (EIP). Once again lack of the proper anharmonic behaviour in the interatomic potentials used, causes MD simulations to have limited predictive power. Moreover the classical treatment of atomic motion, makes MD simulations to be applicable at temperatures typically much higher than 300K.

Anharmonicity is necessary for finite thermal conductivity in a perfect crystal, an observation first made by Peierls [22] in 1929. In a perfect harmonic crystal, phonons do not interact with each other, and application of a perturbation such as a temperature gradient can cause a non-equilibrium phonon population to persist in time. Anharmonicity allows three-phonon interactions through which phonon populations can reach equilibrium. An accurate description of thermal conductivity in a material therefore requires an accurate knowledge of both the harmonic and anharmonic terms in the expansion of energy with respect to atomic displacements.

These interatomic force constants can be obtained with great accuracy from first-principles through the use of density-functional perturbation theory (DFPT) [13, 14,

15]. DFPT is a linear response approach and relies upon the use of "$2n+1$" theorem, which states that the knowledge of the electronic wave function up to order n in the external perturbation is sufficient to determine the energy derivatives with respect to the strength of the perturbation up to order $2n + 1$. This implies that a first order perturbation in the wave functions is sufficient to evaluate the second-order and third-order derivatives of energy.

Giannozzi *et al.* [23] used the density-functional perturbation theory to compute the lattice dynamical properties and second-order interatomic force constants of Si and Ge and obtained excellent agreement between computed and experimentally measured phonon dispersions. This demonstrated the accuracy of the second-order force constants obtained through DFPT. The first attempt to use a first-principles approach to describe anharmonic scattering in Si was made by Narasimhan and Vanderbilt [24] who fitted a Keating model [25] to a few frozen phonon calculations. However, the first truly ab initio calculation of the linewidth (inverse of phonon relaxation time) of a phonon mode at the Γ point was performed by Debernardi *et al.* [13] who obtained anharmonic interatomic force constants by extending density-functional perturbation theory using the "$2n + 1$" theorem [26]. By using the lowest order three-phonon processes, Debernardi *et al.* [13] obtained excellent agreement between the calculated and experimental Raman linewidths for Si and Ge up to temperatures well above the room temperature. Similar results for Raman linewidths were subsequently obtained by Lang *et al.* [27]. These results show that the use of DFPT also leads to accurate third-order interatomic force constants.

For the calculation of thermal conductivity, the knowledge of phonon linewidth at just the Γ point is insufficient. Phonon relaxation times of thousands of wave vectors **q** in the entire Brillouin zone are needed to compute thermal conductivity. While computation of the linewidth of phonon mode at Γ requires knowledge of anharmonic coupling only between the wave-vectors $\mathbf{0}$, q' and $-q'$, where q' varies over the entire Brillouin zone, estimate of the linewidth of a phonon mode of arbitrary wave-vector q requires knowledge of anharmonic coupling constants between three different wave-vectors q, q' and q''. These were first obtained by Deinzer *et al.* [28], who used them

along with the second-order force constants to compute the linewidth of phonon mode of arbitrary wave-vector q.

Broido *et al.* [29] obtained the anharmonic interatomic force constants using the approach outlined by Deinzer *et al.* [28] and solved the phonon Boltzmann equation exactly using an iterative process [30, 17] to compute the thermal conductivity of isotopically pure Si^{28} and Ge^{70}. This first-principles approach, free of any adjustable parameters, was found to yield an excellent agreement between the calculated and experimentally measured thermal conductivities. Subsequent application of this approach to diamond resulted in a similar good agreement between theory and experiment [31]. In this thesis we first compute the thermal conductivity of isotopically pure Si^{28} and Ge^{70} following the approach outlined by Broido *et al.* [29]. We compute the second-order and third-order interatomic force constants from first-principles using density-functional perturbation theory as implemented in the Quantum-ESPRESSO package [32]. Comparison between the computed and experimentally measured values as well as those obtained by Broido *et al.* [29] allows for a benchmarking of our approach. We subsequently use this first-principles approach to predict thermal conductivity in disordered materials such as silicon-germanium alloys as well as nanostructured materials such as superlattices.

The work by Broido [29] demonstrated the success of a first-principles approach to predict thermal conductivity in ordered materials. However, prediction of thermal conductivity in disordered materials is more challenging. To predict thermal conductivity of silicon-germanium alloys, Skye *et al.* [33] performed non-equilibrium molecular dynamics simulations using the Stillinger-Weber potential [18] to simulate Si-Si and Ge-Ge interactions. To treat Si-Ge interactions a geometric mean of the interaction parameters for the pure substances was used. MD simulations confirmed that mass difference played a significantly larger role in phonon scattering than the differences in the chemical bonds introduced by alloying. However the predicted thermal conductivity was found to be lower than experimental value by a factor ranging between 4 and 6. Moreover while experiments showed the temperature dependence of thermal resistivity to be between $T^{1/2}$ and T, MD simulations performed at 300 K

and 500 K showed thermal resistivity to be almost independent of temperature.

In this work we explore the applicability of a first-principles approach to predict thermal conductivity in disordered materials. The structure of SiGe alloys has been shown to be truly random both experimentally and theoretically [34, 35] with no significant long or short range chemical ordering. This random distribution together with the difference between Si and Ge atoms in mass and size makes them good candidates for a first-principles study. The materials are simple insulators at low temperatures, having no electronic contribution to the thermal conductivity. Secondly, experimental data [36, 37, 38, 39, 40, 7, 41, 42] are available for thermal conductivity of SiGe alloy crystals with relatively large grain sizes and small amounts of impurity atoms. This allows an easy comparison between the calculated and experimental values. Thirdly, it is known that in SiGe alloys, mass disorder plays a dominant role in phonon scattering compared to strain disorder [39, 33]. This allows the structure of the alloys to be simulated with the use of virtual crystal approximation (where the atomic potential at each site is taken to be the average of the Si and Ge potentials) [43, 44] making the first principles analysis computationally feasible.

The figure of merit (ZT) of superlattices has been measured to be significantly higher than corresponding bulk materials [11]. This is due to a significant decrease in thermal conductivity in these materials. Extensive work has been done to explain this reduction. Chen [45] developed models on the effective thermal conductivity of periodic thin-film structures in the parallel direction based on the Boltzmann transport equation and found that the atomic scale interface roughness was the major cause for the measured reduction in superlattice thermal conductivity. However Hyldgaard and Mahan [46] attributed the decrease in superlattice thermal conductivity to a lower phonon group velocity due to the confinement of phonon modes. In the above analysis, an approximation known as constant relaxation time approximation was used. A first-principles approach to compute thermal conductivity, where the phonon frequencies, group velocities, populations and relaxation times are explicitly computed using the phonon modes of the superlattice can provide new insights into the parameters controlling thermal transport in these materials.

25

The outline of the thesis is presented below.

In Chapter 2 we give a brief account of the methods used to obtain the interatomic force constants. We explain the "$2n+1$" theorem and give an account of the different extensions which allow computation of second-order and third-order derivatives of energy with respect to different atomic displacements.

In Chapter 3, we present the theory of thermal conductivity and describe the phonon Boltzmann equation (PBE). We describe the computation of the phonon dispersions from the second-order force constants, and also demonstrate how anharmonic force constants lead to three-phonon scattering. Using the single-mode relaxation time approximation to solve the phonon Boltzmann transport equation, we estimate phonon relaxation times and compute thermal conductivity. We compare the thermal conductivity computed using this approach with experimentally reported values. Finally we present the full self-consistent solution of the phonon Boltzmann equation using an iterative process.

In Chapter 4, we address the thermal conductivity of silicon-germanium alloys. We first attempt to compute the thermal conductivity using the same approach used for isotopically pure silicon. However, to incorporate disorder we use large supercells instead of the 2-atom unit cell of silicon. We discuss the validity of the virtual crystal approximation and show that this approach fails to yield the alloy thermal conductivity in the limit of an infinitely large supercell. We next present another approach, where the disordered crystal is replaced with an ordered one, with the average mass and potential of Si and Ge, and disorder is treated as a perturbation. This idea was first proposed by Abeles [39] in 1963. We however now compute all the ingredients in this model from first-principles, and show that the use of this approach leads to excellent agreement with experimentally measured values. We next present the phonon mean free paths in this system and demonstrate the feasibility of nanostructuring to further lower thermal conductivity.

In Chapter 5, we study thermal conductivity in superlattices. We present the variation of superlattice thermal conductivity with period thickness, and discuss the cause of the observed behaviour. We also discuss the discrepancy between computed

and experimentally measured values of superlattice thermal conductivity. We present an interesting effect in the limit of very small period superlattices where we find that the computed thermal conductivity is substantially higher than superlattices of larger period lengths and even exceeds the bulk thermal conductivity of both the materials comprising the superlattice. We discuss the reason behind this unexpected increase and its implications for thermal management of electronics.

Chapter 2

Density-functional perturbation theory

2.1 Introduction

Density functional theory provides a computationally efficient approach to solve the quantum-mechanical problem that governs the properties of matter. In 1964, Hohenberg and Kohn [47] demonstrated that all properties of the nondegenerate ground state of a system of interacting electrons are completely determined by its electron density $n[r]$. From this work density-functional theory evolved as a conceptually and practically useful method for studying the electronic properties of many-electron systems.

Their work, that became the theoretical basis of DFT, builds on the two following fundamental theorems [47]:

Theorem 1 *For any system of interacting particles in an external potential $V_{ext}(\boldsymbol{r})$, the potential $V_{ext}(\boldsymbol{r})$ is determined uniquely, except for a constant, by the ground state particle density $n_o(\boldsymbol{r})$.*

Theorem 2 *A universal functional for the energy $F[n(\boldsymbol{r})]$, expressed in terms of the density $n(\boldsymbol{r})$ can be defined, valid for any external potential $V_{ext}(\boldsymbol{r})$. For any particular $V_{ext}(\boldsymbol{r})$, the exact ground state energy of the system is the global minimum value of*

this functional, and the density $n(\boldsymbol{r})$ that minimized the functional is the exact ground state density $n_o(\boldsymbol{r})$.

In the Kohn-Sham [48] formulation of density-functional theory, the total energy of an electronic system in an external field v_{ext} , is given by:

$$E[n] = \sum_\alpha \epsilon_\alpha - \frac{1}{2} \int \frac{n(r)n(r')}{|r-r'|} dr\,dr' + E_{xc}[n] - \int \frac{\delta E_{xc}[n]}{\delta n(r)} n(r) dr \qquad (2.1)$$

In the above equation $\partial E_{xc}[n]/\partial n(r)$ indicates the functional derivative of the exchange and correlation energy $E_{xc}[n]$, ϵ_α are the eigenvalues of the Kohn-Sham one-particle equations:

$$H|\psi_\alpha\rangle = \epsilon_\alpha |\psi_\alpha\rangle \qquad \langle\psi_\alpha|\psi_\alpha\rangle = 1 \qquad (2.2)$$

The self consistent Hamiltonian H is given by

$$H = -\frac{1}{2}\nabla^2 + v_{ext} + \frac{1}{2} \int \frac{n(r)n(r')}{|r-r'|} dr\,dr' + E_{xc}[n]. \qquad (2.3)$$

The ground state density of the system is :

$$n(r) = \sum_\alpha \psi_\alpha^\star(r)\psi_\alpha(r) \qquad (2.4)$$

where the summation involves all the occupied Kohn-Sham orbitals.

As the Hamiltonian depends upon the Kohn-Sham orbitals through the charge density, the above system of equations has to be solved self-consistently. To do this, a trial density is assumed to begin the process. Using this, Eq. 2.2 is solved for the eigenfunctions. Using these eigenfunctions, a new charge density is computed using Eq. 2.4. This new density is used to compute the Hamiltonian through Eq. 2.3 and then solve Eq. 2.2 again. This process is continued until a self-consistent solution is obtained. This allows the computation of the ground state density along with the corresponding energy.

2.2 $2n + 1$ theorem and density-functional perturbation theory

The use of perturbation theory in the density functional framework was made possible by Baroni, Giannozzi and Testa [14]. They provided an efficient scheme to compute the first-order correction to the wavefunction and second-order correction to the energy. Later, Gonze and Vigneron [49] showed, through the use of $2n + 1$ theorem, that the first-order correction to the wavefunction is the only quantity that was needed to compute the correction to the energy up to third-order. The $2n + 1$ theorem states that the knowledge of all the corrections to the wavefunction up to ψ^n is sufficient to determine all corrections to the energy up to E^{2n+1}. Thus the $2n + 1$ theorem allows one to determine the third derivatives of the energy with respect to the strength of the perturbation, if the linear response of a system to an external perturbation is known.

In this section we analyse the response of the system under a perturbation. When the external potential depends on a parameter λ, we can perform a Taylor expansion and express the potential in terms of higher order terms:

$$v_{ext}(r, \lambda) \equiv v_{ext}^{(0)}(r) + \lambda v_{ext}^{(1)}(r) + \lambda^2 v_{ext}^{(2)}(r) + ... \tag{2.5}$$

Also the Kohn-Sham wave functions may be expanded in the same way:

$$\psi(r, \lambda) = \psi^{(0)} + \lambda \psi^{(1)} + \lambda^2 \psi^{(2)} + ..., \tag{2.6}$$

and the same applies to the corresponding energy functional:

$$E[n, \lambda] = E^{(0)}[n] + \lambda E^{(1)}[n] + \lambda^2 E^{(2)}[n] + \lambda^3 E^{(3)}[n]....... \tag{2.7}$$

The scheme to obtain the first-order correction to wave-function and second-order correction to energy is outlined below.

First, the second-order correction to the energy can be computed from the Hellman-

Feynman theorem, which states that the generalized force associated with a variation of the external parameter is given by the ground-state expectation value of the derivative of $v_{ext}(r, \lambda)$:

$$\frac{\partial E[n, \lambda]}{\partial \lambda} = \int n(r, \lambda) \frac{\partial v_{ext}(r, \lambda)}{\partial \lambda} dr \qquad (2.8)$$

In the above $n(r, \lambda)$ is the electronic ground state density. Taking the derivative of the above equation with respect to λ yields the second-order correction to the energy:

$$E^{(2)}[n] = \int \left(\frac{1}{2} n^{(1)}(r) v_{ext}^{(1)}(r) + n^{(0)}(r) v_{ext}^{(2)}(r) \right) dr, \qquad (2.9)$$

where $n^{(0)}$ is the unperturbed electronic ground-state density, $n^{(1)}(r)$ is the first derivative with respect to λ, $v_{ext}^{(1)}(r)$ and $v_{ext}^{(2)}(r)$ are the first and second derivatives, respectively, of the external potential with respect to λ.

In order to order to evaluate the above expression, the first-order derivative of the charge density $n^{(1)}(r)$ and thus the first-order change in the eigenfunctions need to be known. These are obtained by taking the derivative of Eq. 2.2 and self consistently solving the resulting equation:

$$\left(H^{(0)} - \epsilon_\alpha^{(0)} \right) |\psi_\alpha^{(1)}\rangle = - \left(H^{(1)} - \epsilon_\alpha^{(1)} \right) |\psi_\alpha^{(0)}\rangle. \qquad (2.10)$$

The above equation is also called the *Sternheimer* equation [50]. In the above $H^{(1)}$ is the first-order correction to Hamiltonian and depends upon the first-order eigenfunctions through the first-order charge density

$$H^{(1)} = v_{ext}^{(1)} + \int \frac{\delta^2 E_I[n]}{\delta n(r) \delta n(r')} n^{(1)}(r') dr', \qquad (2.11)$$

where the "interaction energy" $E_I[n]$ is defined as:

$$E_I[n] = \frac{1}{2} \int \frac{n(r)n(r')}{|r - r'|} dr dr' + E_{xc}[n]. \qquad (2.12)$$

The first-order correction to the Kohn-Sham eigenvalues is given by

$$\epsilon_\alpha^{(1)} = \langle \psi_\alpha^{(0)} | H^{(1)} | \psi_\alpha^{(0)} \rangle, \tag{2.13}$$

where the first-order wavefunction has to satisfy the following orthogonality condition:

$$Re \langle \psi_\alpha^{(0)} | \psi_\alpha^{(1)} \rangle = 0. \tag{2.14}$$

The first-order correction to charge density is related to the first-order wavefunction through :

$$n^{(1)}(r) = \sum_\alpha \left[\psi_\alpha^{(1)*}(r) \psi_\alpha^{(0)}(r) + \psi_\alpha^{(0)*}(r) \psi_\alpha^{(1)}(r) \right]. \tag{2.15}$$

Similar to the solution of Kohn-Sham equations, the above set of equations has to be solved iteratively as well. The first iteration is typically begun by using $H^{(1)} = v_{ext}^{(1)}$. Using this, Eq. 2.10 is solved for the first-order wavefunctions $\psi_\alpha^{(1)}$. Knowledge of the first-order wavefunctions allows computing the first-order correction to the charge density $n^{(1)}$ through Eq. 2.14. This can then be used to compute the new first-order Hamiltonian $H^{(1)}$ through Eq. 2.11, which then along with Eq. 2.10 yields the new first-order wavefunctions. This process is repeated until self-consistency is achieved. Using the converged first-order charge density, the second-order correction to energy can be computed through Eq. 2.9.

Using the $2n + 1$ theorem of perturbation theory, Gonze and Vigneron [49] then derived the third-order derivatives of the energy from the knowledge of the first-order wavefunctions. The resulting expression is presented below:

$$E^{(3)} = \sum_\alpha \left[\langle \psi_\alpha^{(1)} | H^{(1)} - \epsilon_\alpha^{(1)} | \psi_\alpha^{(1)} \rangle \right] +$$
$$\int v_{ext}^{(2)}(r) n^{(1)}(r) dr + \int v_{ext}^{(3)}(r) n^{(0)}(r) dr + \tag{2.16}$$
$$\frac{1}{6} \int \frac{\delta^3 E_{xc}[n]}{\delta n(r) \delta n(r') \delta n(r'')} n^{(1)}(r) n^{(1)}(r') n^{(1)}(r'') dr dr' dr''.$$

Gonze and Vigneron [49] further extended the above work to obtain the expression for

33

the third-order derivative of the energy with respect to three arbitrary perturbations, as in the case of three different atomic displacements.

In this work we use density-functional perturbation theory as implemented in the Quantum-ESPRESSO package [32] to obtain the second-order and third-order derivatives of the energy with respect to three atomic displacements.

Chapter 3

Thermal conductivity of isotopically pure Silicon (Si^{28}) and Germanium (Ge^{70})

Thermal conductivity is a fundamental transport property that plays a vital role in many applications. In semiconductors and insulators, heat is conducted by lattice vibrations. Understanding and quantifying the interactions between these vibrations is critical to accurate prediction of thermal conductivity. A theoretical approach to predict lattice thermal conductivity in these materials would facilitate understanding of heat dissipation in microelectronics and nanoelectronics as well as assist in design of high efficiency thermoelectrics for both refrigeration and power generation applications. At temperature above a few tens of degrees Kelvin the lattice thermal conductivity of semiconductors is usually dominated by three-phonon scattering, which arises because of the anharmonicity of the interatomic potential. Anharmonic phonon scattering is an intrinsic resistive process and does not require the presence of defects, impurities or grain boundaries in the material. In 1929 Peierls first formulated a microscopic description of the intrinsic lattice thermal conductivity of semiconductors and insulators through what has become known as the phonon Boltzmann equation (PBE). The equation involves the unknown perturbed population of a phonon mode and balances the perturbation due to the temperature gradient to the change in

phonon population due to scattering. The perturbed phonon populations can be obtained by solving the PBE. While the framework to describe thermal conductivity is well known, the development of a predictive theoretical approach to calculate thermal conductivity has been hindered by the significant complexity inherent in describing (a) interatomic forces between atoms and (b) the inelastic phonon-phonon scattering processes.

The first issue can be addressed by using density-functional perturbation theory to obtain interatomic force constants. Use of DFPT has been shown in the past to yield accurate IFCs, which have led to the prediction of material properties in good agreement with measured values. The challenge involved in the second issue lies in the dependence of inelastic phonon-phonon scattering rates upon the unknown perturbed phonon populations of the phonon modes in the Brillouin zone. A tremendous simplification is however achieved in the calculation of thermal conductivity in bulk semiconductors by using the single-mode relaxation time approximation (SMRT). In this approximation it is assumed that only the phonon mode under consideration is out of equilibrium and relaxes to its equilibrium state, while all other modes remain in their equilibrium states. This allows the three-phonon scattering rate to be expressed in terms of only the unknown population of that mode and a phonon relaxation time which is completely known. This further allows the Boltzmann equation to be solved for the unknown population. The thermal conductivity in this approximation is determined by fundamental properties such as phonon frequencies, group velocities, phonon populations and phonon relaxation times.

Going beyond the use of single-mode relaxation time approximation, the PBE can be solved exactly by using a self-consistent iterative procedure first developed by Omini and Sparavigna [30]. Broido *et al.* [29] used such an exact solution of the phonon Boltzmann equation along with the interatomic force constants derived from density-functional perturbation theory [28] to compute the thermal conductivity of isotopically pure silicon and obtained excellent agreement with measured values.

In this chapter, the theory for first-principles thermal conductivity calculations is presented along with its implementation for isotopically pure Si and Ge. The results

are compared against the experimentally measured values, allowing for a benchmarking of the approach. In subsequent chapters, we compute the thermal conductivity of disordered SiGe alloys as well as superlattices.

3.1 Theory of thermal conductivity

In this section we present the theory of thermal conductivity following Ref. [51]. The potential energy V of a crystal, in which the unit cell is characterized by the vector $\boldsymbol{l}$ and the atomic positions in each unit cell are described by the vector $\boldsymbol{b}$, can be expanded in a Taylor series in powers of the atomic displacements $\boldsymbol{u}(\boldsymbol{lb})$; we show here the expansion up to third-order:

$$
\begin{aligned}
V =V_0 &+ \sum_{lb\alpha} \frac{\partial V}{\partial u_\alpha(\boldsymbol{lb})}\bigg|_0 u_\alpha(\boldsymbol{lb})+ \\
&\frac{1}{2}\sum_{lb,l'b'}\sum_{\alpha\beta} \frac{\partial^2 V}{\partial u_\alpha(\boldsymbol{lb})\partial u_\beta(\boldsymbol{l'b'})}\bigg|_0 u_\alpha(\boldsymbol{lb})u_\beta(\boldsymbol{l'b'})+ \\
&\frac{1}{3!}\sum_{lb,l'b',l''b''}\sum_{\alpha\beta\gamma} \frac{\partial^3 V}{\partial u_\alpha(\boldsymbol{lb})\partial u_\beta(\boldsymbol{l'b'})\partial u_\gamma(\boldsymbol{l''b''})}\bigg|_0 u_\alpha(\boldsymbol{lb})u_\beta(\boldsymbol{l'b'})u_\gamma(\boldsymbol{l''b''}).
\end{aligned}
\tag{3.1}
$$

At equilibrium, the first derivative of the potential energy with respect to atomic displacement is zero, due to the energy being minimum in this configuration:

$$
\frac{\partial V}{\partial u_\alpha(\boldsymbol{lb})}\bigg|_0 = 0.
\tag{3.2}
$$

The second derivative of the energy with respect to atomic displacements yields the second-order force constants

$$
\Phi_{\alpha\beta}(\boldsymbol{lb},\boldsymbol{l'b'}) = \frac{\partial^2 V}{\partial u_\alpha(\boldsymbol{lb})\partial u_\beta(\boldsymbol{l'b'})}\bigg|_0
\tag{3.3}
$$

and the third derivative of energy yields the third-order force constants

$$
\Phi_{\alpha\beta\gamma}(\boldsymbol{lb},\boldsymbol{l'b'},\boldsymbol{l''b''}) = \frac{\partial^3 V}{\partial u_\alpha(\boldsymbol{lb})\partial u_\beta(\boldsymbol{l'b'})\partial u_\gamma(\boldsymbol{l''b''})}\bigg|_0.
\tag{3.4}
$$

The potential energy can now be rewritten in terms of the force constants as

$$
\begin{aligned}
V = V_0 &+ \frac{1}{2} \sum_{lb,l'b'} \sum_{\alpha\beta} \Phi_{\alpha\beta}(lb, l'b') u_\alpha(lb) u_\beta(l'b') + \\
&\frac{1}{3!} \sum_{lb,l'b',l''b''} \sum_{\alpha\beta\gamma} \Phi_{\alpha\beta\gamma}(lb, l'b', l''b'') u_\alpha(lb) u_\beta(l'b') u_\gamma(l''b'').
\end{aligned}
\tag{3.5}
$$

3.1.1 Dynamical matrix and phonon frequencies

If the crystal potential is only expanded up to the second-order with respect to atomic displacements, it can be shown that the displacements can be written in terms of vibration modes which are completely decoupled.

To obtain the equation of motion the first term in the potential energy V_0 is ignored as it does not lead to any forces on atoms. Ignoring it, the equation of motion can be written as:

$$
m_b \ddot{u}_\alpha(lb) = - \sum_{l'b'\beta} \Phi_{\alpha\beta}(lb, l'b') u_\beta(l'b').
\tag{3.6}
$$

Because of translational symmetry, the second-order force constants can be rewritten in terms of the relative position between unit cells $h = l' - l$:

$$
\Phi_{\alpha\beta}(lb, l'b') = \Phi_{\alpha\beta}(0b, (l' - l)b').
\tag{3.7}
$$

The equation of motion can now be written as

$$
m_b \ddot{u}_\alpha(lb) = - \sum_{l'b'\beta} \Phi_{\alpha\beta}(0b, l'b') u_\beta(l'b').
\tag{3.8}
$$

To solve this equation, the displacements can be written as

$$
u_\alpha(lb) = \frac{1}{\sqrt{m_b}} \sum_q U_\alpha(q, b) exp[i(q.l - \omega t)],
\tag{3.9}
$$

where q represents the wave-vector of a vibration mode in the first Brillouin zone with ω as its vibration frequency. By substituting the above expression (Eq. 3.9) into

the equation of motion Eq. 3.8, one obtains

$$\omega^2 U_\alpha(\boldsymbol{q}, \boldsymbol{b}) = \sum_{b'\beta} D_{\alpha\beta}(\boldsymbol{b}\boldsymbol{b}'|\boldsymbol{q})U_\beta(\boldsymbol{q}, \boldsymbol{b}'). \tag{3.10}$$

The above translates into the following determinant equation

$$|D_{\alpha\beta}(\boldsymbol{b}\boldsymbol{b}'|\boldsymbol{q}) - \omega^2 \delta_{\alpha\beta}\delta_{bb'}| = 0, \tag{3.11}$$

where $D_{\alpha\beta}(\boldsymbol{b}\boldsymbol{b}'|\boldsymbol{q})$ is the dynamical matrix and is given by the following expression:

$$D_{\alpha\beta}(\boldsymbol{b}\boldsymbol{b}'|\boldsymbol{q}) = \frac{1}{\sqrt{m_b m_{b'}}} \sum_{l'} \Phi_{\alpha\beta}(\boldsymbol{0}\boldsymbol{b}, \boldsymbol{l}'\boldsymbol{b}') exp(i\boldsymbol{q}.\boldsymbol{l}'). \tag{3.12}$$

Diagonalizing the dynamical matrix yields the phonon frequencies. Thus, expansion of the potential energy up to second-order results in vibration modes which are completely decoupled and do not interact. To see this more explicitly we notice that in the harmonic approximation where the third-order term in the expansion of potential energy is ignored, the crystal Hamiltonian can be written as

$$\begin{aligned} H = \sum_{lb} \frac{\boldsymbol{p}(\boldsymbol{lb}).\boldsymbol{p}(\boldsymbol{lb})}{2m} + \\ \frac{1}{2} \sum_{lb,l'b'} \sum_{\alpha\beta} \Phi_{\alpha\beta}(\boldsymbol{lb}, \boldsymbol{l}'\boldsymbol{b}')u_\alpha(\boldsymbol{lb})u_\beta(\boldsymbol{l}'\boldsymbol{b}'). \end{aligned} \tag{3.13}$$

In the above $\boldsymbol{p}(\boldsymbol{lb})$ represents the momentum operator of an atom located at $\boldsymbol{l} + \boldsymbol{b}$. To rewrite the above in terms of vibration wave-vectors $\boldsymbol{q}$ we make use of a set of transformations that involve replacing the displacement and momentum operators with their Fourier representations $\boldsymbol{X}$ and $\boldsymbol{P}$, respectively:

$$\boldsymbol{u}(\boldsymbol{lb}) = \frac{1}{\sqrt{N_0}} \sum_q \boldsymbol{X}(\boldsymbol{q}, \boldsymbol{b})e^{i\boldsymbol{q}.\boldsymbol{l}} \tag{3.14}$$

$$\boldsymbol{p}(\boldsymbol{lb}) = \frac{1}{\sqrt{N_0}} \sum_q \boldsymbol{P}(\boldsymbol{q}, \boldsymbol{b})e^{-i\boldsymbol{q}.\boldsymbol{l}}. \tag{3.15}$$

39

Here $N_0 = N_1 N_2 N_3$ is the crystal size, N_1, N_2 and N_3 being the number of unit cells along the three lattice directions. Using the above transformations the Hamiltonian can be rewritten as,

$$H = \frac{1}{N_0} \sum_{qq'lb} \frac{\boldsymbol{P}(\boldsymbol{q}, \boldsymbol{b}).\boldsymbol{P}(\boldsymbol{q}', \boldsymbol{b})}{2m_b} exp[-i(\boldsymbol{q} + \boldsymbol{q}').\boldsymbol{l}] +$$
$$\frac{1}{2}\frac{1}{N_0} \sum_{q,q'} \sum_{lb,l'b'} \sum_{\alpha\beta} \Phi_{\alpha\beta}(\boldsymbol{lb}, \boldsymbol{l'b'}) X_\alpha(\boldsymbol{q}, \boldsymbol{b}) X_\beta(\boldsymbol{q}', \boldsymbol{b}') exp[i(\boldsymbol{q}.\boldsymbol{l} + \boldsymbol{q}'.\boldsymbol{l}')].$$

(3.16)

The first term can be simplified by performing the summation over $\boldsymbol{l}$,

$$\text{First Term} = \sum_{q,q'b} \frac{\boldsymbol{P}(\boldsymbol{qb}).\boldsymbol{P}(\boldsymbol{q'b})}{2m_b} \frac{1}{N_0} \sum_l exp[-i(\boldsymbol{q} + \boldsymbol{q}').\boldsymbol{l}]$$
$$= \sum_{qq'b} \frac{\boldsymbol{P}(\boldsymbol{qb}).\boldsymbol{P}(\boldsymbol{q'b})}{2m_b} \delta_{q+q',o}$$

(3.17)

$$= \sum_{qb} \frac{\boldsymbol{P}(\boldsymbol{qb}).\boldsymbol{P}^\dagger(\boldsymbol{qb})}{2m_b}.$$

As indicated earlier, because of the translational symmetry, the second-order force constants can be rewritten in terms of only the relative position between the unit cells $\boldsymbol{h} = \boldsymbol{l}' - \boldsymbol{l}$ as shown by Eq. 3.7. Using this the second term can be rewritten as:

Second Term
$$= \frac{1}{2}\frac{1}{N_0} \sum_{q,q'} \sum_{lb,l'b'} \sum_{\alpha\beta} \Phi_{\alpha\beta}(\boldsymbol{lb}, \boldsymbol{l'b'}) X_\alpha(\boldsymbol{q}, \boldsymbol{b}) X_\beta(\boldsymbol{q}', \boldsymbol{b}') exp[i(\boldsymbol{q}.\boldsymbol{l} + \boldsymbol{q}'.\boldsymbol{l}')]$$
$$= \frac{1}{2}\frac{1}{N_0} \sum_{q,q'} \sum_{b,hb'} \sum_{\alpha\beta} \Phi_{\alpha\beta}(\boldsymbol{0b}, \boldsymbol{hb'}) X_\alpha(\boldsymbol{q}, \boldsymbol{b}) X_\beta(\boldsymbol{q}', \boldsymbol{b}') exp[i\boldsymbol{q}'.\boldsymbol{h}] \sum_l exp[i(\boldsymbol{q} + \boldsymbol{q}').\boldsymbol{l}]$$
$$= \frac{1}{2} \sum_{q,q'} \sum_{b,hb'} \sum_{\alpha\beta} \Phi_{\alpha\beta}(\boldsymbol{0b}, \boldsymbol{hb'}) X_\alpha(\boldsymbol{q}, \boldsymbol{b}) X_\beta(\boldsymbol{q}', \boldsymbol{b}') exp[i\boldsymbol{q}'.\boldsymbol{h}] \delta_{q+q',o}$$
$$= \frac{1}{2} \sum_{q} \sum_{b,hb'} \sum_{\alpha\beta} \Phi_{\alpha\beta}(\boldsymbol{0b}, \boldsymbol{hb'}) X_\alpha(\boldsymbol{q}, \boldsymbol{b}) X_\beta(-\boldsymbol{q}, \boldsymbol{b}') exp[-i\boldsymbol{q}.\boldsymbol{h}].$$

(3.18)

In the above use is made of: $\sum_l exp[i(\boldsymbol{q} + \boldsymbol{q}').\boldsymbol{l}] = N_0 \delta_{q+q',o}$.

Using

$$\Phi_{\alpha\beta}(\boldsymbol{bb'}|\boldsymbol{q}) = \sum_{\boldsymbol{h}} \Phi_{\alpha\beta}(\boldsymbol{ob}, \boldsymbol{hb'}) exp(-i\boldsymbol{q}.\boldsymbol{h})$$

$$= \sqrt{m_b m_{b'}} D_{\alpha\beta}(\boldsymbol{bb'}|-\boldsymbol{q})$$

(3.19)

where D is the dynamical matrix, the second term can now be written as,

$$\text{Second Term} = \frac{1}{2} \sum_{\boldsymbol{q,b,b'}} \sum_{\alpha\beta} \Phi_{\alpha\beta}(\boldsymbol{bb'}|\boldsymbol{q}) X_\alpha(\boldsymbol{q}, \boldsymbol{b}) X_\beta^\dagger(\boldsymbol{qb'}).$$

(3.20)

Using Eqs. 3.17 and 3.20 crystal Hamiltonian in the harmonic approximation can now be written as a sum over the different vibration wave vectors $\boldsymbol{q}$,

$$H = \sum_{\boldsymbol{q}} \left[\sum_{\boldsymbol{b}} \frac{\boldsymbol{P(qb)}.\boldsymbol{P^\dagger(qb)}}{2m_b} + \frac{1}{2} \sum_{\boldsymbol{b,b'}} \sum_{\alpha\beta} \Phi_{\alpha\beta}(\boldsymbol{bb'}|\boldsymbol{q}) X_\alpha(\boldsymbol{q}, \boldsymbol{b}) X_\beta^\dagger(\boldsymbol{qb'}) \right].$$

(3.21)

The above Hamiltonian is completely separable and therefore has independent eigenstates or vibration modes. However it is shown next that the inclusion of the third-order anharmonic term in the potential energy expansion leads to coupling (scattering) between three vibration modes.

3.1.2 Anharmonic potential

Including the third-order term in the expansion of the potential energy the crystal Hamiltonian can be written as:

$$H = \sum_{lb} \frac{\boldsymbol{p(lb)}.\boldsymbol{p(lb)}}{2m} +$$

$$\frac{1}{2} \sum_{lb,l'b'} \sum_{\alpha\beta} \Phi_{\alpha\beta}(\boldsymbol{lb}, \boldsymbol{l'b'}) u_\alpha(\boldsymbol{lb}) u_\beta(\boldsymbol{l'b'}) +$$

$$\frac{1}{3!} \sum_{lb,l'b',l''b''} \sum_{\alpha\beta\gamma} \Phi_{\alpha\beta\gamma}(\boldsymbol{lb}, \boldsymbol{l'b'}, \boldsymbol{l''b''}) u_\alpha(\boldsymbol{lb}) u_\beta(\boldsymbol{l'b'}) u_\gamma(\boldsymbol{l''b''}).$$

(3.22)

41

We focus the discussion on rewriting of the third term V_3 to show how anharmonicity leads to three-phonon coupling. Using the transformations represented by Eqs. 3.14 and 3.15, V_3 can be rewritten as

$$V_3 = \frac{1}{3!} \frac{1}{(N_0)^{3/2}} \sum_{qq'q''} \sum_{lb,l'b',l''b''} \sum_{\alpha\beta\gamma} \Phi_{\alpha\beta\gamma}(lb, l'b', l''b'') X_\alpha(\boldsymbol{q}, \boldsymbol{b}) X_\beta(\boldsymbol{q'}, \boldsymbol{b'}) X_\gamma(\boldsymbol{q''}, \boldsymbol{b''})$$

$$\times exp[i(\boldsymbol{q}.\boldsymbol{l} + \boldsymbol{q'}.\boldsymbol{l'} + \boldsymbol{q''}.\boldsymbol{l''})].$$

(3.23)

Defining $\boldsymbol{h'} = \boldsymbol{l'} - \boldsymbol{l}$ and $\boldsymbol{h''} = \boldsymbol{l''} - \boldsymbol{l}$ the cubic term V_3 can be further rewritten as

$$V_3 = \frac{1}{3!} \frac{1}{(N_0)^{3/2}} \sum_{qb,q'b',q''b''} \sum_{\alpha\beta\gamma} \sum_{l} exp[i(\boldsymbol{q} + \boldsymbol{q'} + \boldsymbol{q''}).\boldsymbol{l}]$$

$$\times \Phi_{\alpha\beta\gamma}(\boldsymbol{qb}, \boldsymbol{q'b'}, \boldsymbol{q''b''}) X_\alpha(\boldsymbol{q}, \boldsymbol{b}) X_\beta(\boldsymbol{q'}, \boldsymbol{b'}) X_\gamma(\boldsymbol{q''}, \boldsymbol{b''})$$

(3.24)

where

$$\Phi_{\alpha\beta\gamma}(\boldsymbol{qb}, \boldsymbol{q'b'}, \boldsymbol{q''b''}) = \sum_{h',h''} \Phi_{\alpha\beta\gamma}(\boldsymbol{ob}, \boldsymbol{h'b'}, \boldsymbol{h''b''}) e^{i\boldsymbol{q'h'}} e^{i\boldsymbol{q''h''}}.$$

(3.25)

Finally summing over $\boldsymbol{l}$ and realizing that $\sum_l exp[i(\boldsymbol{q} + \boldsymbol{q'} + \boldsymbol{q''}).\boldsymbol{l}] = N_0 \delta_{G,q+q'+q''}$, we obtain

$$V_3 = \frac{1}{3!} \frac{1}{\sqrt{N_0}} \sum_{qb,q'b',q''b''} \delta_{G,q+q'+q''} \sum_{\alpha\beta\gamma}$$

$$\times \Phi_{\alpha\beta\gamma}(\boldsymbol{qb}, \boldsymbol{q'b'}, \boldsymbol{q''b''}) X_\alpha(\boldsymbol{q}, \boldsymbol{b}) X_\beta(\boldsymbol{q'}, \boldsymbol{b'}) X_\gamma(\boldsymbol{q''}, \boldsymbol{b''}).$$

(3.26)

$\boldsymbol{G}$ in the above equation is the reciprocal lattice vector.

To explicitly show the three-phonon couplings and to convert the anharmonic term into a form where it can be used to compute the three-phonon scattering rates, two more transformations are performed. The second set of transformations allows the anharmonic term to be expressed in terms of the vibration eigenvectors $\boldsymbol{e}(\boldsymbol{b}|\boldsymbol{qs})$, where s represents a particular vibration mode of the vibration characterized by wave-vector $\boldsymbol{q}$. The transformations are indicated below:

$$X(\boldsymbol{qs}) = \sum_b \sqrt{m_b} e^*(\boldsymbol{b}|\boldsymbol{qs}).X(\boldsymbol{qb})$$

(3.27)

42

$$P(\boldsymbol{q}s) = \sum_b \frac{1}{\sqrt{m_b}} e(\boldsymbol{b}|\boldsymbol{q}s).\boldsymbol{P}(\boldsymbol{q}b). \tag{3.28}$$

The vibration eigenvectors obey the following relationships

$$\sum_b e^*(\boldsymbol{b}|\boldsymbol{q}s).e(\boldsymbol{b}|\boldsymbol{q}s') = \delta_{ss'} \tag{3.29}$$

$$\sum_s e^*_\alpha(\boldsymbol{b}|\boldsymbol{q}s)e_\beta(\boldsymbol{b}'|\boldsymbol{q}s) = \delta_{\alpha\beta}\delta_{bb'}. \tag{3.30}$$

Finally, the last set of transformations involves the use of the creation and annihilation operators a_{qs} and $a^\dagger_{qs}$:

$$a_{qs} = \frac{1}{\sqrt{2\hbar\omega(\boldsymbol{q}s)}} P(\boldsymbol{q}s) - i\sqrt{\frac{\omega(\boldsymbol{q}s)}{2\hbar}} X^\dagger(\boldsymbol{q}s) \tag{3.31}$$

$$a^\dagger_{qs} = \frac{1}{\sqrt{2\hbar\omega(\boldsymbol{q}s)}} P^\dagger(\boldsymbol{q}s) + i\sqrt{\frac{\omega(\boldsymbol{q}s)}{2\hbar}} X(\boldsymbol{q}s). \tag{3.32}$$

We discuss next some of the properties of creation and annihilation operators. Let a state with n phonons of wavevector $\boldsymbol{q}$ and polarisation s be denoted by $|n_{qs}\rangle$; the effect of the creation and annihilation operators on such a state is summarized below:

$$a^\dagger_{qs}|n_{qs}\rangle = \sqrt{n_{qs} + 1}|n_{qs} + 1\rangle \tag{3.33}$$

$$a_{qs}|n_{qs}\rangle = \sqrt{n_{qs}}|n_{qs} - 1\rangle. \tag{3.34}$$

Inverting Eqs. 3.31 and 3.32 allows the operators $X(\boldsymbol{q}s)$ and $P(\boldsymbol{q}s)$ to be written in terms of creation and annihilation operators:

$$X(\boldsymbol{q}s) = -i\sqrt{\frac{\hbar}{2\omega(\boldsymbol{q}s)}}(a^\dagger_{qs} - a_{-qs}) \tag{3.35}$$

$$P(\boldsymbol{q}s) = \sqrt{\frac{\hbar\omega(\boldsymbol{q}s)}{2}}(a_{qs} + a^\dagger_{-qs}). \tag{3.36}$$

43

Finally, using Eqs. 3.27 and 3.28, the operators $\boldsymbol{X}(\boldsymbol{qb})$ and $\boldsymbol{P}(\boldsymbol{qb})$ can now be written in terms of the vibration eigenvectors and the creation and annihilation operators:

$$
\begin{aligned}
\boldsymbol{X}(\boldsymbol{qb}) &= \frac{1}{\sqrt{m_b}} \sum_s \boldsymbol{e}(b|\boldsymbol{qs}) X(\boldsymbol{qs}) \\
&= -i \sum_s \sqrt{\frac{\hbar}{2m_b\omega(\boldsymbol{qs})}} \boldsymbol{e}(b|\boldsymbol{qs})(a_{qs}^\dagger - a_{-qs})
\end{aligned}
\tag{3.37}
$$

$$
\begin{aligned}
\boldsymbol{P}(\boldsymbol{qb}) &= \sqrt{m_b} \sum_s \boldsymbol{e}^*(b|\boldsymbol{qs}) P(\boldsymbol{qs}) \\
&= \sum_s \sqrt{\frac{m_b\hbar\omega(\boldsymbol{qs})}{2}} \boldsymbol{e}^*(b|\boldsymbol{qs})(a_{qs} + a_{-qs}^\dagger).
\end{aligned}
\tag{3.38}
$$

Substituting the above in the expression for the cubic term in the crystal Hamiltonian yields

$$
\begin{aligned}
V_3 &= \frac{1}{3!} \frac{i}{\sqrt{N_0}} \sum_{\substack{qs,q's',q''s'' \\ bb'b''}} \sum_{\alpha\beta\gamma} \left(\frac{\hbar^3}{8m_b m_{b'} m_{b''} \omega(\boldsymbol{qs})\omega(\boldsymbol{q's'})\omega(\boldsymbol{q''s''})} \right)^{1/2} \\
&\quad \times \delta_{G,q+q'+q''} e_\alpha(b|\boldsymbol{qs}) e_\beta(b'|\boldsymbol{q's'}) e_\gamma(b''|\boldsymbol{q''s''}) \Phi_{\alpha\beta\gamma}(\boldsymbol{qb}, \boldsymbol{q'b'}, \boldsymbol{q''b''}) \\
&\quad \times (a_{qs}^\dagger - a_{-qs})(a_{q's'}^\dagger - a_{-q's'})(a_{q''s''}^\dagger - a_{-q''s''}) \\
&= \frac{i\hbar}{3!} \sum_{qs,q's',q''s''} \delta_{G,q+q'+q''} \tilde{V}_3(\boldsymbol{qs}, \boldsymbol{q's'}, \boldsymbol{q''s''}) \\
&\quad \times (a_{qs}^\dagger - a_{-qs})(a_{q's'}^\dagger - a_{-q's'})(a_{q''s''}^\dagger - a_{-q''s''})
\end{aligned}
\tag{3.39}
$$

where

$$
\tilde{V}_3(\boldsymbol{qs}, \boldsymbol{q's'}, \boldsymbol{q''s''}) = \left(\frac{\hbar}{8N_0\omega(\boldsymbol{qs})\omega(\boldsymbol{q's'})\omega(\boldsymbol{q''s''})} \right)^{1/2} \sum_{b,b',b''} \sum_{\alpha\beta\gamma} \Phi_{\alpha\beta\gamma}(\boldsymbol{qb}, \boldsymbol{q'b'}, \boldsymbol{q''b''})
$$
$$
\times \frac{e_\alpha(b|\boldsymbol{qs})}{\sqrt{m_b}} \frac{e_\beta(b'|\boldsymbol{q's'})}{\sqrt{m_{b'}}} \frac{e_\gamma(b''|\boldsymbol{q''s''})}{\sqrt{m_{b''}}}.
\tag{3.40}
$$

Eq. 3.39 shows that an anharmonic term in the expansion of potential energy leads to scattering between three phonons such that $\boldsymbol{G} = \boldsymbol{q} + \boldsymbol{q'} + \boldsymbol{q''}$. We next compute the rates of phonon scattering due to anharmonicity and use them along with Boltzmann

transport equation to compute thermal conductivity.

3.1.3 Boltzmann transport equation

In the absence of a temperature gradient, the heat flux in a material is zero and the phonon modes are in their equilibrium state with the phonon populations being determined by the Bose-Einstein distribution

$$\bar{n}_{qs} = \frac{1}{e^{\hbar\omega(qs)/(k_B T)} - 1} \tag{3.41}$$

where $\bar{n}(qs)$ and $\omega(qs)$ are the equilibrium population and the frequency, respectively, of the phonon mode qs, $\hbar$ is the Planck's constant and k_B is the Boltzmann constant.

However, the presence of a temperature gradient in a material causes the phonon population of any mode qs to be perturbed out of equilibrium and establishes a heat flux Q than can be written in terms of phonon energies $\hbar\omega(qs)$, perturbed phonon populations n_{qs}, and phonon group velocities $c(qs)$ as

$$Q_\alpha = \frac{1}{N_0 \Omega} \sum_{qs} \hbar\omega(qs) c_\alpha(qs) n_{qs} = -k_{\alpha\beta} |\nabla T|_\beta, \tag{3.42}$$

where Ω is the volume of the unit-cell. As shown above the heat flux can be further written as the product of the thermal conductivity k and the temperature gradient ∇T. Thermal conductivity is a tensor whose components $k_{\alpha\beta}$ give the direction of heat flux along a direction α for a temperature gradient along direction β.

Knowledge of the perturbed phonon populations allows heat flux and in turn thermal conductivity to be determined. As phonon populations are a function of temperature, a temperature gradient creates an imbalance in the flux of a phonon mode qs through an elemental volume in the material as shown in Fig. 3-1. If the phonon mode qs does not interact (scatter) with other phonon modes (i.e. $\partial n_{qs}/\partial t|_{scatt} = 0$) as is the case in a perfect harmonic crystal, such an imbalance creates a divergence in the perturbed phonon population leading to a divergence in the thermal conductivity. A perfect harmonic crystal therefore has infinite thermal conductivity. Through,

$$-\frac{\partial n_{qs}}{\partial t}\bigg|_{scatt}$$

$$c_x(\boldsymbol{q}s)n_{qs}(T+dT) \qquad c_x(\boldsymbol{q}s)n_{qs}(T)$$

$$T+dT \qquad\qquad T \qquad\qquad x$$
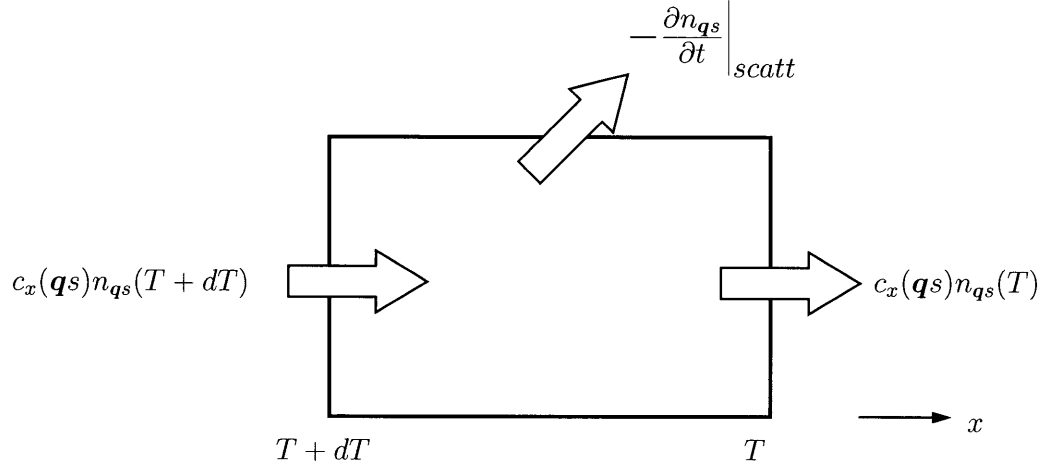
Figure 3-1: Perturbation in phonon population due to temperature gradient balanced by the change due to scattering induced by the anharmonicity of the interatomic potential.

three-phonon scattering processes anharmonicity allows for the perturbation due to the temperature gradient to be balanced by the change in phonon population by scattering, leading to a finite thermal conductivity. The resulting balance equation for the perturbed phonon population is called the phonon Boltzmann equation (PBE) [16, 51, 30]:

$$-\boldsymbol{c}(\boldsymbol{q}s).\boldsymbol{\nabla}T\left(\frac{\partial n_{qs}}{\partial T}\right) + \frac{\partial n_{qs}}{\partial t}\bigg|_{scatt} = 0, \qquad (3.43)$$

where n_{qs} and $\boldsymbol{c}(\boldsymbol{q}s)$ are the perturbed phonon population and group velocity respectively of mode $\boldsymbol{q}s$. The first term on the left-hand side represents phonon diffusion induced by a temperature gradient and the second term represents the phonon scattering rate due to all scattering processes. Assuming that the perturbation from equilibrium is small, the temperature gradient of the perturbed phonon population can be replaced with the temperature gradient of the equilibrium phonon population, $\partial n_{qs}/\partial T \approx \partial \bar{n}_{qs}/\partial T$, leading to

$$-\boldsymbol{c}(\boldsymbol{q}s).\boldsymbol{\nabla}T\left(\frac{\partial \bar{n}_{qs}}{\partial T}\right) + \frac{\partial n_{qs}}{\partial t}\bigg|_{scatt} = 0, \qquad (3.44)$$

where $\bar{n}_{qs}$ is the equilibrium population of mode $\boldsymbol{q}s$ and is determined by the Bose-
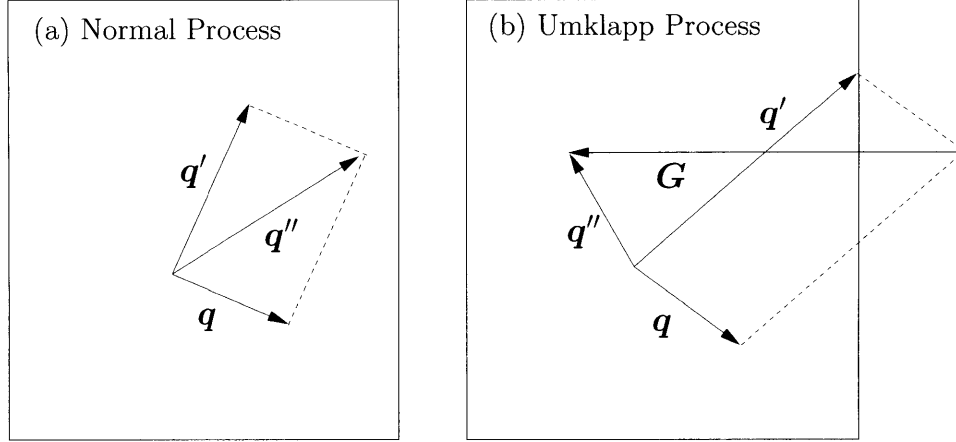
Figure 3-2: (a) Normal and (b) Umklapp processes – for class 1 events or the "coalescence processes".

Einstein distribution Eq. 3.41.

As indicated in the previous section, in a pure material a phonon mode qs can scatter through anharmonic three-phonon scattering processes such that $G = q + q' + q''$. The three-phonon scattering can thus be classified into two types:

1. Normal processes: For these type of processes, $G = 0$. For example, when a phonon q scatters by absorbing another phonon q' to yield phonon q'' the momentum conservation for this process can be written as $-q - q' + q'' = 0$. This is shown in Fig. 3-2(a). As can be seen, these processes preserve the direction of energy flow, since the resulting phonon is in the same direction as the combining phonon modes. Hence these processes do not contribute towards thermal resistance in a material.

2. The second type of processes are characterized by $G \neq 0$. Here the momentum conservation for the process indicated above would be $q + q' = q'' + G$. This is shown in Fig. 3-2(b). As can be seen, in this process the direction of energy flow is reversed. These type of scattering processes were given the name "Umklapp" by Peierls [52], and they give rise to thermal resistance in a material.

The scattering rate for a three-phonon scattering process can be computed using Fermi's golden rule [53, 54]:

47
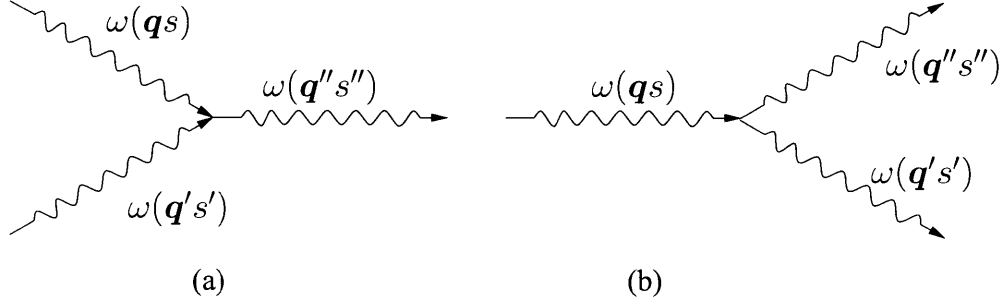
Figure 3-3: (a) Class 1 and (b) Class 2 events associated with three-phonon scattering.

$$P_i^f(3ph) = \frac{2\pi}{\hbar}|\langle f|V_3|i\rangle|^2\delta(E_f - E_i).$$ (3.45)

In the above equation i and f denote the initial and final state, V_3 is the three phonon coupling potential as expressed in Eq. 3.39, and $\delta(E_f - E_i)$ denotes energy conservation between the initial and final states.

There are two types of events associated with three-phonon scattering. In the first type of events, called class 1 events or "coalescence processes", a phonon mode $(\boldsymbol{q}s)$ scatters by absorbing another mode $(\boldsymbol{q}'s')$ to yield a third phonon mode $(\boldsymbol{q}''s'')$. In the second type of events, called class 2 events or "decay processes" a phonon mode $(\boldsymbol{q}s)$ scatters by decaying into two phonon modes $(\boldsymbol{q}'s')$ and $(\boldsymbol{q}''s'')$. These two classes of events are shown in Figs. 3-3 (a) and (b) respectively.

Both processes satisfy momentum and energy conservation: For class 1 events, these are:

$$\boldsymbol{q} + \boldsymbol{q}' = \boldsymbol{q}'', \quad \hbar\omega(\boldsymbol{q}s) + \hbar\omega(\boldsymbol{q}'s') = \hbar\omega(\boldsymbol{q}''s''),$$ (3.46)

while for class 2 events we have

$$\boldsymbol{q} = \boldsymbol{q}' + \boldsymbol{q}'', \quad \hbar\omega(\boldsymbol{q}s) = \hbar\omega(\boldsymbol{q}'s') + \hbar\omega(\boldsymbol{q}''s'').$$ (3.47)

The reciprocal lattice vector $\boldsymbol{G}$ is not explicitly written in the above equations.

For class 1 events the scattering rate is given by :

$$P_{qs,q's'}^{q''s''} = \frac{2\pi}{\hbar^2} |\langle n_{qs} - 1, n_{q's'} - 1, n_{q''s''} + 1|V_3|n_{qs}, n_{q's'}, n_{q''s''}\rangle|^2 \\ \times \delta(\omega(qs) + \omega(q's') - \omega(q''s''))$$

(3.48)

where n in the above equation represent the perturbed phonon populations. Substituting V_3 from Eq. 3.39, we obtain

$$P_{qs,q's'}^{q''s''} = 2\pi|\tilde{V}_3(-qs, -q's', q''s'')|^2 n_{qs} n_{q's'} (n_{q''s''} + 1) \\ \times \delta(\omega(qs) + \omega(q's') - \omega(q''s''))$$

(3.49)

The factor of 1/3! in the expression for V_3 is cancelled by the presence of 3! equivalent terms involved in the summation over q, q', q''. This is due to the fact that the expression for V_3 is cyclically symmetric in q, q', q''. Secondly in the expansion of $(a_{qs}^\dagger - a_{-qs})(a_{q's'}^\dagger - a_{-q's'})(a_{q''s''}^\dagger - a_{-q''s''})$ only one term, $a_{-qs} a_{-q's'} a_{q''s''}^\dagger$, survives, as this is the only term that couples the initial state $|n_{qs}, n_{q's'}, n_{q''s''}\rangle$ with the final state $|n_{qs} - 1, n_{q's'} - 1, n_{q''s''} + 1\rangle$.

The net scattering rate involving a class 1 event can be written as the difference of the forward and back scattering processes. The expression is given below:

$$P_{qs,q's'}^{q''s''} - P_{q''s''}^{qs,q's'} = 2\pi\delta(\omega(qs) + \omega(q's') - \omega(q''s''))|\tilde{V}_3(-qs, -q's', q''s'')|^2 \\ [n_{qs} n_{q's'} (n_{q''s''} + 1) - (n_{qs} + 1)(n_{q's'} + 1)n_{q''s''}] .$$

(3.50)

At equilibrium and in the absence of a temperature gradient, the net scattering rate is zero. This yields the principle of detailed balance for the class 1 events:

$$\bar{n}_{qs} \bar{n}_{q's'} (\bar{n}_{q''s''} + 1) = (\bar{n}_{qs} + 1)(\bar{n}_{q's'} + 1)\bar{n}_{q''s''},$$

(3.51)

that can be rewritten as

$$\bar{n}_{q's'} - \bar{n}_{q''s''} = \frac{\bar{n}_{q's'}(\bar{n}_{q''s''} + 1)}{(\bar{n}_{qs} + 1)}.$$

(3.52)

To linearize the scattering rates in Eq. 3.50, we expand the perturbed phonon population n_{qs} about the equilibrium in terms of a first order perturbation Ψ_{qs} defined as

$$n_{qs} = \bar{n}_{qs} - \frac{k_B T}{\hbar} \frac{\partial \bar{n}_{qs}}{\partial \omega(\boldsymbol{q}s)} \Psi_{qs}, \tag{3.53}$$

leading to

$$n_{qs} = \bar{n}_{qs} + \bar{n}_{qs}(\bar{n}_{qs} + 1)\Psi_{qs}. \tag{3.54}$$

Substituting Eq. 3.54 into Eq. 3.50, the net scattering rate due to class 1 events can be written as :

$$P^{q''s''}_{qs,q's'} - P^{qs,q's'}_{q''s''} = \widetilde{P}^{q''s''}_{qs,q's'}(\Psi^s_q + \Psi^{s'}_{q'} - \Psi^{s''}_{q''}) \tag{3.55}$$

where

$$\begin{aligned}
\widetilde{P}^{q''s''}_{qs,q's'} =& 2\pi \bar{n}_{qs}\bar{n}_{q's'}(\bar{n}_{q''s''} + 1)|\tilde{V}_3(-\boldsymbol{q}s, -\boldsymbol{q}'s', \boldsymbol{q}''s'')|^2 \\
& \times \delta(\omega(\boldsymbol{q}s) + \omega(\boldsymbol{q}'s') - \omega(\boldsymbol{q}''s'')).
\end{aligned} \tag{3.56}$$

Similarly the scattering rate due to class 2 events is expressed as

$$\begin{aligned}
P^{q's',q''s''}_{qs} =& \frac{2\pi}{\hbar^2}|\langle n_{qs} - 1, n_{q's'} + 1, n_{q''s''} + 1|V_3|n_{qs}, n_{q's'}, n_{q''s''}\rangle|^2 \\
& \times \delta(\omega(\boldsymbol{q}s) - \omega(\boldsymbol{q}'s') - \omega(\boldsymbol{q}''s'')).
\end{aligned} \tag{3.57}$$

Substituting V_3 from Eq. 3.39 we obtain:

$$\begin{aligned}
P^{q's',q''s''}_{qs} =& 2\pi|\tilde{V}_3(-\boldsymbol{q}s, \boldsymbol{q}'s', \boldsymbol{q}''s'')|^2 n_{qs}(n_{q's'} + 1)(n_{q''s''} + 1) \\
& \times \delta(\omega(\boldsymbol{q}s) - \omega(\boldsymbol{q}'s') - \omega(\boldsymbol{q}''s'')).
\end{aligned} \tag{3.58}$$

The net scattering rate involving a class 2 event is

$$\begin{aligned}
P^{q's',q''s''}_{qs} - P^{qs}_{q's',q''s''} =& 2\pi\delta(\omega(\boldsymbol{q}s) - \omega(\boldsymbol{q}'s') - \omega(\boldsymbol{q}''s''))|\tilde{V}_3(-\boldsymbol{q}s, \boldsymbol{q}'s', \boldsymbol{q}''s'')|^2 \\
& [n_{qs}(n_{q's'} + 1)(n_{q''s''} + 1) - (n_{qs} + 1)n_{q's'}n_{q''s''}] \,.
\end{aligned} \tag{3.59}$$

Again, at equilibrium, the net scattering rate for class 2 events is zero, yielding the

following identity for class 2 events:

$$\bar{n}_{qs}(\bar{n}_{q's'} + 1)(\bar{n}_{q''s''} + 1) = (\bar{n}_{qs} + 1)\bar{n}_{q's'}\bar{n}_{q''s''}, \tag{3.60}$$

that can be rewritten as

$$1 + \bar{n}_{q's'} + \bar{n}_{q''s''} = \frac{\bar{n}_{q's'}\bar{n}_{q''s''}}{\bar{n}_{qs}}. \tag{3.61}$$

Making use of Eq. 3.54, the scattering rate due to class 2 events becomes

$$P_{qs}^{q's',q''s''} - P_{q's',q''s''}^{qs} = \widetilde{P}_{qs}^{q's',q''s''}(\Psi_q^s - \Psi_{q'}^{s'} - \Psi_{q''}^{s''}) \tag{3.62}$$

where

$$\widetilde{P}_{qs}^{q's',q''s''} = 2\pi\bar{n}_{qs}(\bar{n}_{q's'} + 1)(\bar{n}_{q''s''} + 1)|\Phi(-qs, q's', q''s'')|^2 \\ \times \delta(\omega(qs) - \omega(q's') - \omega(q''s'')). \tag{3.63}$$

The net scattering rate of a phonon mode is the sum of scattering rates due to the class 1 and class 2 events and is given by

$$-\frac{\partial n_{qs}}{\partial t}\bigg|_{scatt} = \sum_{q's',s''} \left[\left(P_{qs,q's'}^{q''s''} - P_{q''s''}^{qs,q's'} \right) + \frac{1}{2}\left(P_{qs}^{q's',q''s''} - P_{q's',q''s''}^{qs} \right) \right] \\ = \sum_{q's',s''} \left[\widetilde{P}_{qs,q's'}^{q''s''}(\Psi_q^s + \Psi_{q'}^{s'} - \Psi_{q''}^{s''}) + \frac{1}{2}\widetilde{P}_{qs}^{q's',q''s''}(\Psi_q^s - \Psi_{q'}^{s'} - \Psi_{q''}^{s''}) \right]. \tag{3.64}$$

Substituting the above expression for net scattering rate into Eq. 3.44, the PBE can now be rewritten as

$$-c(qs).\nabla T\left(\frac{\partial\bar{n}_{qs}}{\partial T}\right) = \sum_{q's',s''} \left[\widetilde{P}_{qs,q's'}^{q''s''}(\Psi_q^s + \Psi_{q'}^{s'} - \Psi_{q''}^{s''}) + \frac{1}{2}\widetilde{P}_{qs}^{q's',q''s''}(\Psi_q^s - \Psi_{q'}^{s'} - \Psi_{q''}^{s''}) \right]. \tag{3.65}$$

3.1.4 Single-mode relaxation time approximation

Eq. 3.65 shows that the PBE for the unknown Ψ_q^s is coupled together with the unknown phonon populations of all other modes ($\Psi_{q'}^{s'}$, $\Psi_{q''}^{s''}$) all over the Brillouin zone. The complexity involved in solving the phonon Boltzmann equation (PBE) based on the three phonon processes lies in the dependence of the distribution function n_{qs} on the occupation of all other states, allowed by energy and momentum conservation. The scattering rate of a mode when the entire system relaxes to equilibrium would in general not be the same as when all other modes are in equilibrium. In the first situation the PBE's of all the different modes qs are coupled together and have to be solved simultaneously in a self consistent way [30, 17]. The second situation corresponds to the single mode relaxation time approximation [55, 56, 16, 57, 58]. In this approximation, the PBE is solved for n_{qs} by assuming that $\Psi_{q'}^{s'}, \Psi_{q''}^{s''}$ are zero where $q's'$ and $q''s''$ are modes involved in the scattering of mode qs. We first calculate the thermal conductivity in the single mode relaxation time approximation and later compare it with the result obtained from the full self consistent solution of the Boltzmann transport equation.

In the single-mode relaxation time approximation, by setting $\Psi_{q'}^{s'}, \Psi_{q''}^{s''} = 0$ and using identities represented by Eqs. 3.52 and 3.61, Eq. 3.64 can be rewritten as,

$$
\begin{aligned}
-\left.\frac{\partial n_{qs}}{\partial t}\right|_{scatt} = \bar{n}_{qs}(\bar{n}_{qs}+1)\Psi_q^s \pi \sum_{q's',s''} |\tilde{V}_3(-qs, q's', q''s'')|^2 \\
\times \left[2(\bar{n}_{q's'} - \bar{n}_{q''s''})\delta(\omega(qs) + \omega(q's') - \omega(q''s'')) + \right. \\
\left. (1 + \bar{n}_{q's'} + \bar{n}_{q''s''})\delta(\omega(qs) - \omega(q's') - \omega(q''s'')) \right].
\end{aligned}
$$

(3.66)

Using Eq. 3.54, the above can be rewritten as

$$
-\left.\frac{\partial n_{qs}}{\partial t}\right|_{scatt} = \frac{n_{qs} - \bar{n}_{qs}}{\tau_{qs}}
$$

(3.67)

where τ_{qs} is the phonon relaxation time and is given by the following expression:

$$\frac{1}{\tau_{qs}} = 2\Gamma_{qs} = \pi \sum_{q's',s''} |\tilde{V}_3(-qs, q's', q''s'')|^2$$
$$\times \left[2(\bar{n}_{q's'} - \bar{n}_{q''s''})\delta(\omega(qs) + \omega(q's') - \omega(q''s'')) + \right. \qquad (3.68)$$
$$\left. (1 + \bar{n}_{q's'} + \bar{n}_{q''s''})\delta(\omega(qs) - \omega(q's') - \omega(q''s'')) \right].$$

In the above expression $2\Gamma_{qs}$ is the full linewidth at half maximum (FWHM).

Now solving the PBE assuming a temperature gradient along direction β, we get

$$-c_\beta(qs)|\boldsymbol{\nabla}T|_\beta \left(\frac{\partial \bar{n}_{qs}}{\partial T} \right) = -\frac{\partial n_{qs}}{\partial t}\bigg|_{scatt}$$
$$= \frac{n_{qs} - \bar{n}_{qs}}{\tau_{qs}}. \qquad (3.69)$$

Therefore

$$n_{qs} - \bar{n}_{qs} = -c_\beta(qs)|\boldsymbol{\nabla}T|_\beta \left(\frac{\partial \bar{n}_{qs}}{\partial T} \right) \tau_{qs}$$
$$= -c_\beta(qs)|\boldsymbol{\nabla}T|_\beta \bar{n}_{qs}(\bar{n}_{qs} + 1)\frac{\hbar\omega(qs)}{k_B T^2}\tau_{qs}. \qquad (3.70)$$

Substituting the perturbed phonon population obtained above into the expression for heat flux (Eq. 3.42) yields the following expression for thermal conductivity

$$k_{\alpha\beta} = \frac{\hbar^2}{N_0 \Omega k_B T^2} \sum_{qs} c_\alpha(qs) c_\beta(qs) \omega^2(qs) n_{qs}(n_{qs} + 1)\tau_{qs}. \qquad (3.71)$$

3.2 Implementation

Thus, in order to compute thermal conductivity in the single mode relaxation time approximation, the only inputs required are the second-order and the third-order interatomic force constants (IFCs).

Steps involved in the thermal conductivity calculation are outlined below:

1.) The second-order interatomic force constants (IFCs) $\Phi_{\alpha\beta}(ob, hb')$ are obtained. The second-order IFC's allow computation of the dynamical matrix $D_{\alpha\beta}(bb'|q)$,

whose eigenvalues yield the phonon frequencies and the dispersion, from which the phonon group velocities and Bose-Einstein populations can be computed. The second-order force constants yield the second derivative of energy with respect to two atomic displacements; as the distance between the atoms increases, these force constants diminish in magnitude. In order to ensure an accurate estimate of dynamical matrix, these force constants have to obtained in real space on a large enough supercell such that the force constants have decayed to negligibly small values. We find that a supercell size of 10x10x10 is enough to ensure this. However, direct calculation of force constants in real space is computationally expensive as it requires using a supercell with thousands of atoms. Instead, first the Brillouin zone is discretized into 10x10x10 grid of q points; then the force constants in q space $\Phi_{\alpha\beta}(bb'|q)$ are computed for q belonging to this grid, using density-functional perturbation theory in reciprocal space. This calculation is computationally much cheaper as it involves using the primitive fcc unit cell with only two atoms. The force constants in q space, $\Phi_{\alpha\beta}(bb'|q)$, are then inverse Fourier transformed to obtain the force constants in real space:

$$\Phi_{\alpha\beta}(ob, hb') = \sum_{q} \Phi_{\alpha\beta}(bb'|q)exp(iq.h), \tag{3.72}$$

where q in the above equation now belongs to the 10x10x10 grid in the first Brillouin zone, and h is the lattice vector of a unit cell on a 10x10x10 supercell in real space. The dynamical matrix at any arbitrary q' can now be obtained by a simple Fourier transform of these real space force constants

$$D_{\alpha\beta}(bb'|-q') = \frac{1}{\sqrt{m_b m_{b'}}} \sum_{h} \Phi_{\alpha\beta}(ob, hb')exp(-iq'.h). \tag{3.73}$$

2.) Next, the third-order interatomic force constants $\Phi_{\alpha\beta\gamma}(lb, l'b', l''b'')$ are computed. The third-order IFC's are used to compute the three-phonon scattering matrix elements, which along with the phonon frequencies and populations yield the phonon relaxation times. As in the case of second-order force constants, the third order force constants decay with the distance between atoms and have to be computed

on a large enough supercell such that for the farthest atoms in the supercell, these force constants have diminished to negligible values. In the case of second-order force constants this calculation was performed indirectly, the force constants were first obtained in $\boldsymbol{q}$ space and then inverse Fourier transformed to get them in real space. To repeat the same process for the third-order force constants, force constants in $\boldsymbol{q}$ space $\Phi_{\alpha\beta\gamma}(\boldsymbol{qb}, \boldsymbol{q'b'}, \boldsymbol{q''b''})$ need to determined for $\boldsymbol{q}$, $\boldsymbol{q'}$ and $\boldsymbol{q''}$ belonging to a chosen grid in the first Brillouin zone. As in the case of second-order force constants, this approach would reduce computational cost as it would allow using the primitive fcc unit cell with only two atoms. However DFPT as implemented in the Quantum-ESPRESSO package [32] currently only allows the above calculation for $\boldsymbol{q} = \boldsymbol{0}$, $\boldsymbol{q''} = -\boldsymbol{q'}$. Knowledge of the force constants $\Phi_{\alpha\beta\gamma}(\boldsymbol{0b}, \boldsymbol{q'b'}, -\boldsymbol{q'b''})$ on the two atom unit cell is only sufficient to compute the linewidth of the phonon mode at Γ (since momentum conservation $\boldsymbol{q} + \boldsymbol{q'} + \boldsymbol{q''} = \boldsymbol{0}$ leads to $\boldsymbol{q''} = -\boldsymbol{q'}$ for $\boldsymbol{q} = \boldsymbol{0}$).

Due to the above limitation the third-order force constants $\Phi_{\alpha\beta\gamma}(\boldsymbol{lb}, \boldsymbol{l'b'}, \boldsymbol{l''b''})$ are computed at Γ using density-functional perturbation theory on larger supercells sized 2x2x2 and 3x3x3 containing 16 and 54 atoms respectively. This makes the calculation computationally expensive. While calculation of third-order force constants on 2x2x2 supercell required a few hours on twelve 2.4 GHz processors, calculation on a 3x3x3 supercell required about 30 days for the same computational resources. Computing third-order force constants on a mesh larger than 3x3x3 is prohibitively expensive. By comparing the phonon linewidths obtained from force constants on a 2x2x2 versus 3x3x3 supercell, an estimate of the convergence of the phonon linewidth is obtained. We find that the force constants obtained on a 3x3x3 supercell are adequate for the present calculation and lead to a only a small error in the estimate of the phonon linewidth (inverse of phonon relaxation time). The three-phonon matrix elements are then computed using these force constants through Eq. 3.39, which are then used to compute phonon relaxation times using Eq. 3.68.

3.) To compute the thermal conductivity, the first Brillouin zone is discretized into a grid of $\boldsymbol{q}$ points, and the thermal conductivity is computed using Eq. 3.71. At any $\boldsymbol{q}$ in the grid, the phonon frequencies are computed using the second-order force

constants obtained in step 1, and the phonon group velocities are computed from the derivative of the phonon dispersion $\partial \omega / \partial q$, using the central difference technique

$$c(qs) = \frac{\partial \omega(qs)}{\partial q} = \frac{\omega(q + \Delta q, s) - \omega(q - \Delta q, s)}{2\Delta q}. \tag{3.74}$$

Finally, the phonon population is computed using the Bose-Einstein distribution (Eq. 3.41).

4.) To compute the relaxation time of any phonon mode q, the Brillouin zone is again discretized into a grid of q'. The relaxation time is then computed by evaluating the sum in Eq. 3.68. The convergence of the computed relaxation time with respect to the size of the q' grid is studied. It is found that for a grid of size 30x30x30, relaxation times are sufficiently converged. Also to compute the relaxation time, the delta function for the energy conservation in Eq. 3.68 is replaced by a Gaussian

$$\delta(\omega) = \frac{1}{\sqrt{\pi}\epsilon} exp(-(\omega/\epsilon)^2); \tag{3.75}$$

a width of $\epsilon = 2.5$ cm^{-1} along with a q' grid of size 30x30x30 is found to lead to reasonably converged relaxation times.

5.) Finally, the convergence of the computed thermal conductivity with respect to the size of the q grid in the first Brillouin zone is studied. The converged result is taken to be the thermal conductivity in the single mode relaxation time approximation.

For all density-functional perturbation theory calculations a 8x8x8 Monkhorst-Pack [59] mesh is used to sample electronic states in the Brillouin zone and an energy cutoff of 20 Ry is used for the plane-wave expansion. Convergence of all quantities with respect to these parameters is carefully tested. First-principles calculations within density-functional theory are carried out using the PWscf and PHonon codes of the Quantum-ESPRESSO distribution [32] with norm-conserving pseudopotentials based on the approach of von Barth and Car [60].

3.3 Phonon linewidth of the zone center optical mode in Si and Ge

Calculation of the linewidth of zone center optical phonon modes can be performed more accurately than that of any arbitrary q. This is due to the fact that for computing the linewidth of the zone center optical phonons, the elements $\Phi_{\alpha\beta\gamma}(qb, q'b', q''b'')$ need to be known only for $q = 0, q'' = -q'$, i.e. only $\Phi_{\alpha\beta\gamma}(0b, q'b', -q'b'')$ need to be known. These can be obtained directly from density-functional perturbation theory for q' belonging to grids even larger than 3x3x3, and relatively cheaply.

Thus, to study the convergence of linewidth of the zone center optical mode, we obtain directly $\Phi_{\alpha\beta\gamma}(0b, q'b', -q'b'')$ using DFPT on grids of size 2x2x2, 3x3x3, and 4x4x4 respectively.

Linewidth at Γ is computed by discretizing the Brillouin zone into a dense grid of q' wavevectors and computing the sum in Eq. 3.68. For this, $\Phi_{\alpha\beta\gamma}(0b, q'b', -q'b'')$ need to be known for thousands of q' wavevectors over the entire Brillouin zone. These are therefore interpolated from the $\Phi_{\alpha\beta\gamma}(0b, q'b', -q'b'')$ computed using DFPT on either a 2x2x2, 3x3x3, or 4x4x4 q' grid in the first Brillouin zone. The linewidths computed using $\Phi_{\alpha\beta\gamma}(0b, q'b', -q'b'')$ interpolated from three different starting grids are compared. This gives insight into the rate of decay of the anharmonic force constants with distance between atoms. If the anharmonic force constants in real space diminish rapidly with the distance between atoms, then this would lead to their variation in q space to be relatively smaller. This in turn would allow accurate linewidth to be obtained using $\Phi_{\alpha\beta\gamma}(0b, q'b', -q'b'')$ interpolated from even a small initial q' grid in the Brillouin zone.

Linewidths computed using $\Phi_{\alpha\beta\gamma}(0b, q'b', -q'b'')$ interpolated from three different starting grids (2x2x2, 3x3x3 and 4x4x4) are compared against the experimentally measured values in Fig. 3-4.

It can be seen that the linewidths computed using $\Phi_{\alpha\beta\gamma}(0b, q'b', -q'b'')$ obtained on a 4x4x4 initial grid agree very well with both the first-principles calculation performed by Lang *et al.* [27], and also the experimental values. Interestingly however,
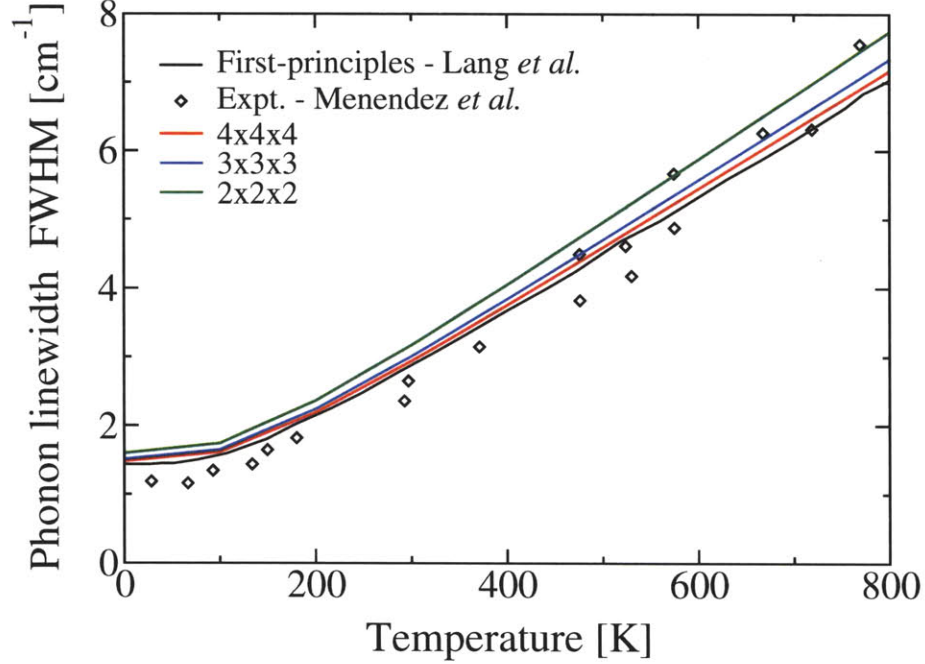
Figure 3-4: Comparison of the phonon linewidth of the zone center optical mode in Si^{28} computed using the anharmonic force constants interpolated from three different initial q' grids in the Brillouin zone, 2x2x2, 3x3x3 and 4x4x4. The computed values are compared against the computed values obtained by Lang *et al.* [27] and the experimentally measured values obtained by Menéndez and Cardona [61].

the linewidths computed even with the $\Phi_{\alpha\beta\gamma}(0b, q'b', -q'b'')$ obtained on a 3x3x3 initial grid agree well with experimentally measured values, with only a small error. This confirms that the anharmonic force constants decay rapidly in real space and thus vary smoothly in q space, allowing accurate interpolations based on even a 3x3x3 grid.

3.4   Phonon lifetimes in Si and Ge

To compute phonon linewidth (inverse of lifetime) of any mode (qs), where s is the vibration branch, the Brillouin zone is discretized into a grid of wavevectors q', and the linewidth is computed using Eq. 3.68. The linewidth is found to converge for a q' grid size of 30x30x30. As indicated earlier, the third-order force constants
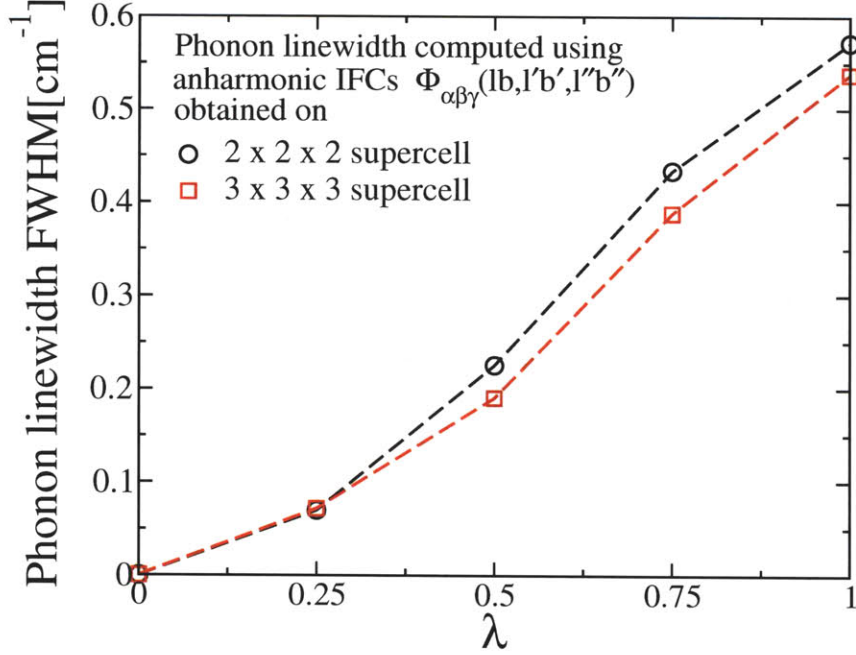
Figure 3-5: Comparison of the phonon linewidth of the transverse acoustic modes along Γ-X $(0,0,\lambda)$ in Si^{28} at 300 K computed using anharmonic force constants obtained on two different supercells, 2x2x2 and 3x3x3.

$\Phi_{\alpha\beta\gamma}(\boldsymbol{ob}, \boldsymbol{h'b'}, \boldsymbol{h''b''})$ needed to compute phonon linewidths were obtained on two different supercells, 2x2x2 and 3x3x3. The phonon linewidth of phonon modes along the direction Γ-X was computed using these two different sets of interatomic force constants. The results for the TA modes at 300 K are presented in Fig. 3-5.

The difference between the two linewidths is only about 6.3% for the TA mode at $(0, 0, 1.0)$; however, it is much larger, at about 18% at $(0, 0, 0.5)$. Although the change in linewidth can be expected to be smaller in going from a 3x3x3 to a 4x4x4 supercell, there is certainly a small error introduced in the thermal conductivity calculation due to the inability to compute the third-order IFC's on a supercell larger than 3x3x3.

Phonon relaxation times to compute the thermal conductivity were thus computed using the third-order IFCs obtained on a 3x3x3 supercell. In Fig. 3-6 the anharmonic relaxation times in silicon are presented along directions of high symmetry at 50 K, 100 K, 300 K, and 500 K respectively.
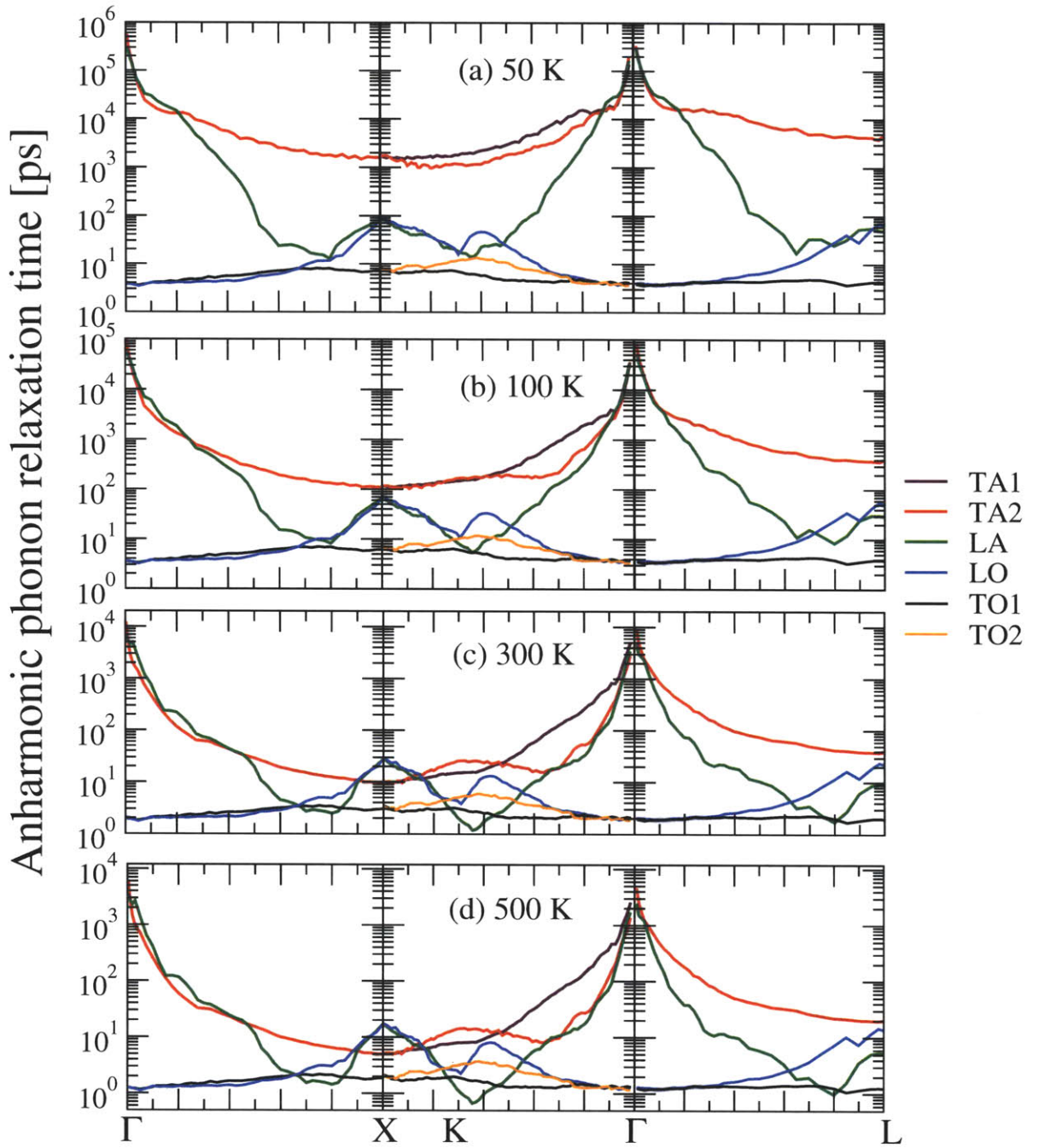
Figure 3-6: Anharmonic phonon relaxation times in Si^{28} at 50 K, 100 K , 300 K and 500 K along directions of high symmetry.

3.5   Thermal conductivity of Si and Ge

In this section, the heat carrying ability of the different modes is compared. The total thermal conductivity is computed and compared against experimentally measured values.

As indicated before, to compute the thermal conductivity the Brillouin zone is discretized in a grid of q wave-vectors. For each vibration mode qs in the grid the phonon frequencies, group velocities, populations and relaxation times are computed. The thermal conductivity is then computed by using Eq. 3.71. We first study the convergence of the computed thermal conductivity with respect to the size of the q grid. Fig. 3-7a shows the thermal conductivity of Si^{28} computed using three different grid sizes of 10x10x10, 30x30x30 and 50x50x50 respectively. The computed value converges for a grid size of 30x30x30.

In Fig. 3-7(b) we compare the converged computed thermal conductivity of Si^{28} and Ge^{70} in the single mode relaxation time approximation with experimentally measured values. The computed values in the single mode relaxation time approximation agree well with the experimentally measured values [62, 63] both qualitatively and quantitatively, the disagreement being about 16% for Si^{28} and 14% for Ge^{70} at 300 K.

3.5.1   Contribution of TA and LA modes to thermal conductivity

The good agreement between computed and measured values allows these results to be used for a more detailed understanding of the parameters controlling thermal transport in bulk semiconductor materials. One of the issues that has been strongly debated is the relative contribution of longitudinal and transverse acoustic modes in conducting heat in Silicon and Germanium. Hamilton and Parott [64] solved the Boltzmann transport equation by using a variational approach using a trial function; using a linear phonon dispersion, they showed that in Germanium transverse acoustic modes conduct about 80-90% of the heat, while the contribution of longitudinal
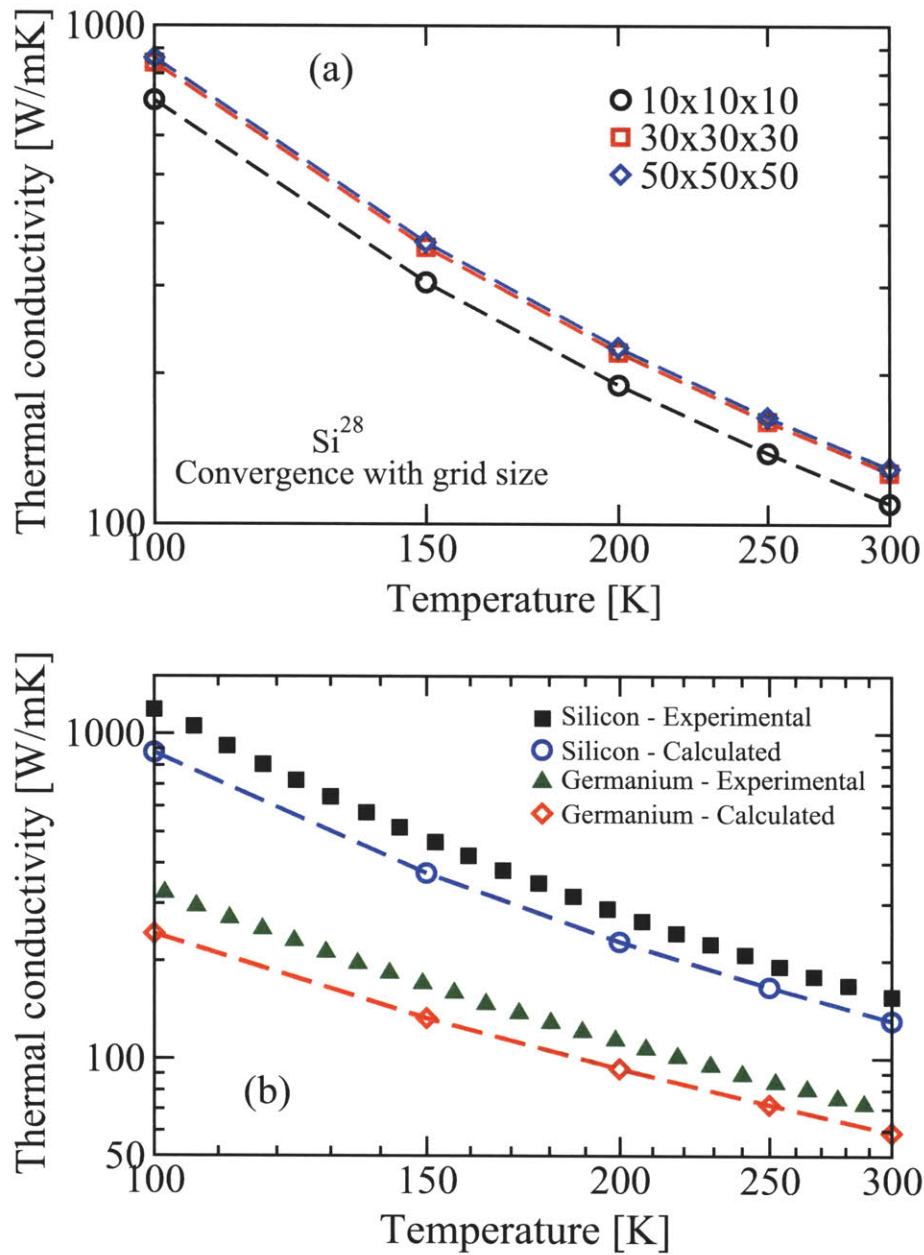
Figure 3-7: (a) Convergence of the computed thermal conductivity of Si^{28} with the size of q grid in first Brillouin zone (b) Comparison between the computed thermal conductivity in the single-mode relaxation time approximation and the experimentally measured values for Si^{28} and Ge^{70}. The discrepancy is about 15% at 300K. Experimentally measured values are from Ref. [62] (Si^{28}, solid squares) and Ref. [63] (Ge^{70}, solid triangles).

phonons to thermal conductivity is less that 20%. Their work led to the idea that transverse acoustic modes play the dominant role in thermal conduction. Savvides and Goldsmid [65] used the results of Hamilton and Parott to explain their experimental results. However, Ju and Goodson [66] measured thermal conductivity of silicon thin films and through modelling explained the results by assuming that LA modes were the dominant heat carriers. More recently Henry and Chen [21] performed molecular dynamics simulations using an environment dependent interatomic potential (EDIP) to study thermal transport in silicon. They found that LA phonons contributed roughly 45% to thermal conductivity while TA modes conducted about 50% of the heat. Clearly there a is large scatter in the values reported for the relative importance of TA and LA modes in conducting heat. The main reason for this disagreement is that, while empirical potentials have been partially successful in capturing the second-order vibration properties such as the phonon dispersion correctly, their use to predict the anharmonic behaviour is largely unsuccessful. Empirical potentials are almost never fitted to any properties related to third-order derivatives (such as Gruneisen parameter) and therefore cannot be expected to yield the correct third-order behaviour.

In Fig. 3-8 we compare the different modes along Γ-L line in terms of their phonon frequencies, group velocities, populations and relaxation times i.e all the ingredients necessary to compute thermal conductivities. The populations and relaxation times are presented at 300K: it can be seen right away that optical modes have much smaller group velocities, phonon populations and relaxation times, compared to the acoustic phonons. Optical phonons can thus be expected to have only a small contribution to the thermal conductivity. Among the acoustic modes, while transverse acoustic modes have lower frequencies and group velocities compared to LA modes, they have higher populations and relaxation times; Actually the relaxation times of TA modes are higher than those of the LA modes, almost by an order of magnitude in certain parts of the Brillouin zone.

In Fig. 3-9(a) we compare the heat carrying ability of the different modes along the direction Γ-L$(\lambda,\lambda,\lambda)$. It can be seen that lower frequencies and group velocities of
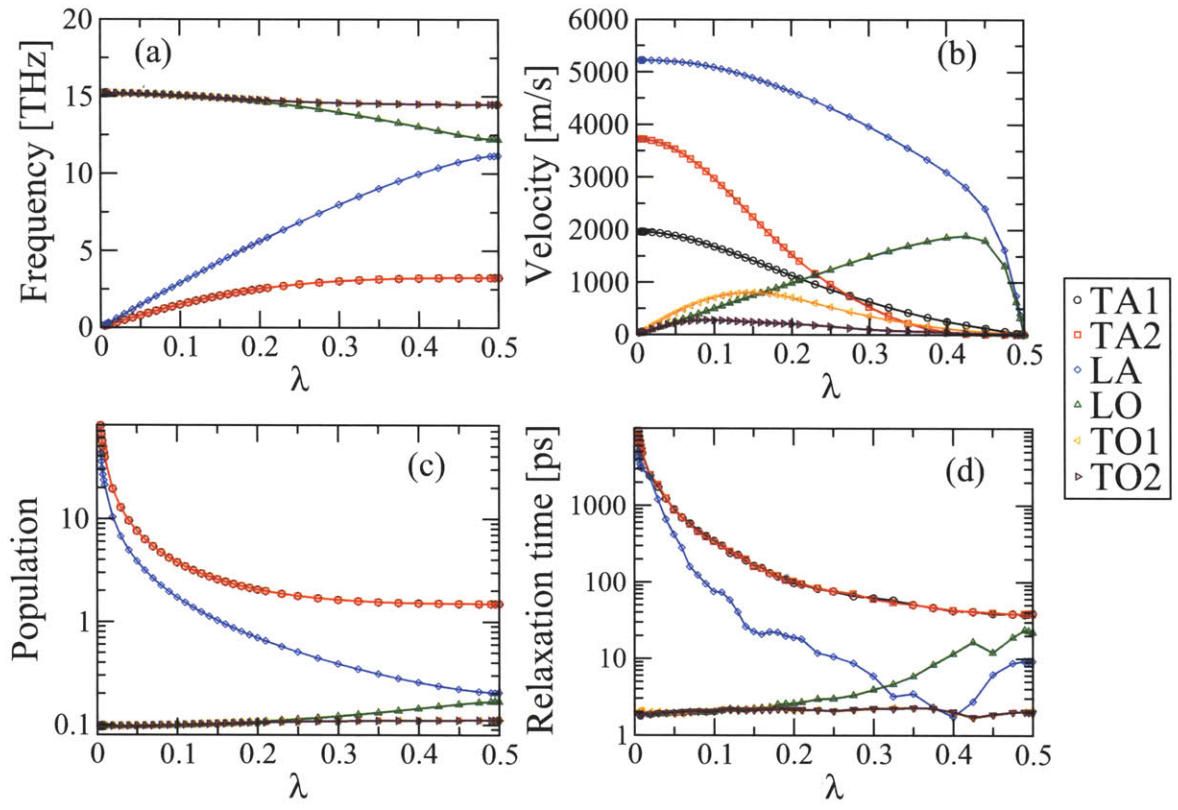
Figure 3-8: (a) Phonon frequencies, (b) group velocities, (c) Bose-Einstein populations and (d)relaxation times – in Si^{28} at 300K for different modes along the Γ-L direction $(\lambda,\lambda,\lambda)$.
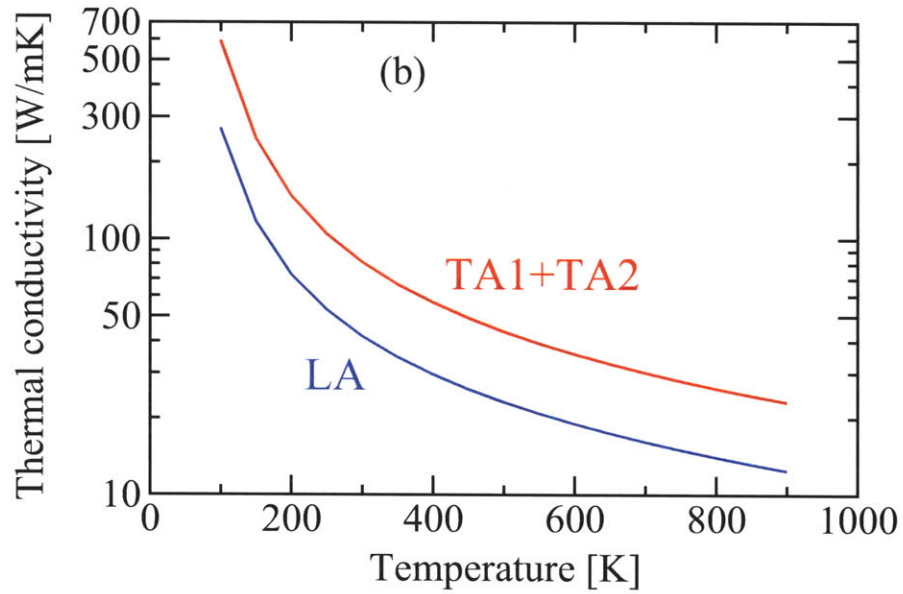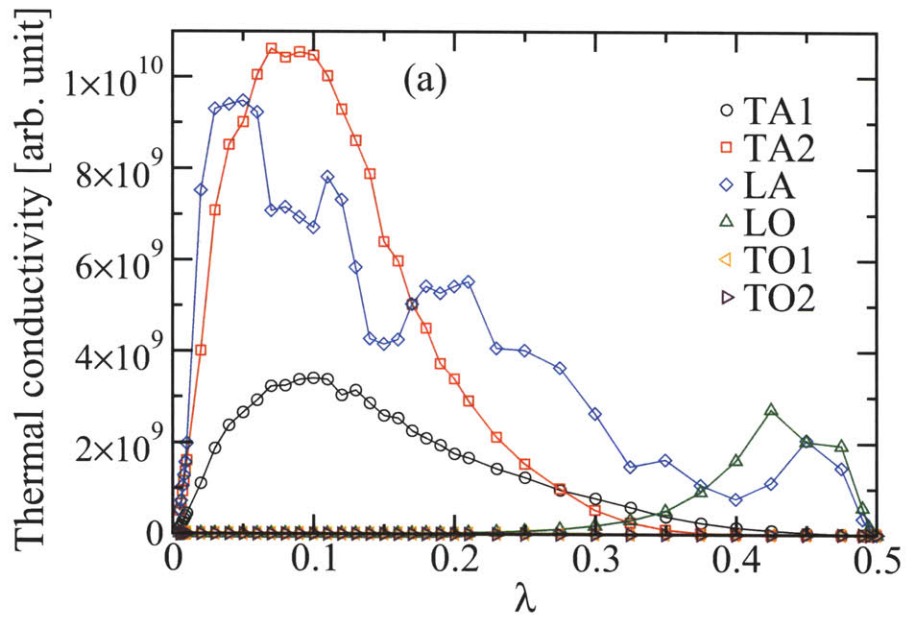
Figure 3-9: (a) Heat conduction ability of different modes along Γ-L $(\lambda,\lambda,\lambda)$ at 300 K in Si^{28} (b) Comparison of the contribution of the transverse and longitudinal acoustic modes to total thermal conductivity in Si^{28}. At 300 K, TA modes contribute almost 63% and LA modes contribute 32% of the thermal conductivity.

the TA modes are compensated by their higher relaxation times, leading to the heat conduction of each TA mode being comparable to that of the LA modes.

In Fig. 3-9(b) the total contribution to the thermal conductivity of the TA and LA modes is compared. In silicon, at room temperature, it is found that the TA modes conduct about 63% of the heat and LA modes conduct about 32%, the remaining 5% being conducted by optical phonons. These values are significantly different from results reported above [64, 65, 66, 21]. First-principles calculations can thus provide more accurate understanding of parameters controlling thermal transport.

Figs. 3-10(a) and (b) show the frequency dependence of the thermal conductivity in Si^{28} and Ge^{70} respectively: in Si^{28}, even though acoustic modes extend in frequencies to more than 10 THz, only modes up to about 6 THz contribute to the thermal conductivity. A decrease in relaxation times and phonon group velocities with increase in frequency diminishes the heat conduction ability of higher frequency phonons. The small jump in thermal conductivity at 12 THz occurs due to the contribution of longitudinal optical modes. Similar trends can be seen for Ge^{70}.

3.5.2 Phonon mean free path dependence

The dependence of thermal conductivity on phonon mean free path is presented in Fig. 3-11. The phonon mean free path of a mode qs is taken to be the product of its relaxation time τ_{qs} and the magnitude of its group velocity $|c(qs)|$. Peak contribution to thermal conductivity at room temperature comes primarily from phonons of relatively small mean free path, about 50 nm in Si^{28} and about 40 nm in Ge^{70}. As the temperature is lowered, an increase in relaxation times shifts the peak contribution to higher mean free paths. Even though the contribution to thermal conductivity drops significantly with the increase in mean free path, the long tail ensures that these large mean free path phonons still contribute significantly to the total thermal conductivity.

Fig. 3-12 shows the accumulation of thermal conductivity as a function of phonon mean free path. In Si^{28}, more than 50% of the heat is carried by phonons of mean free path larger than 200 nm. This provides avenues to lower thermal conductivity through
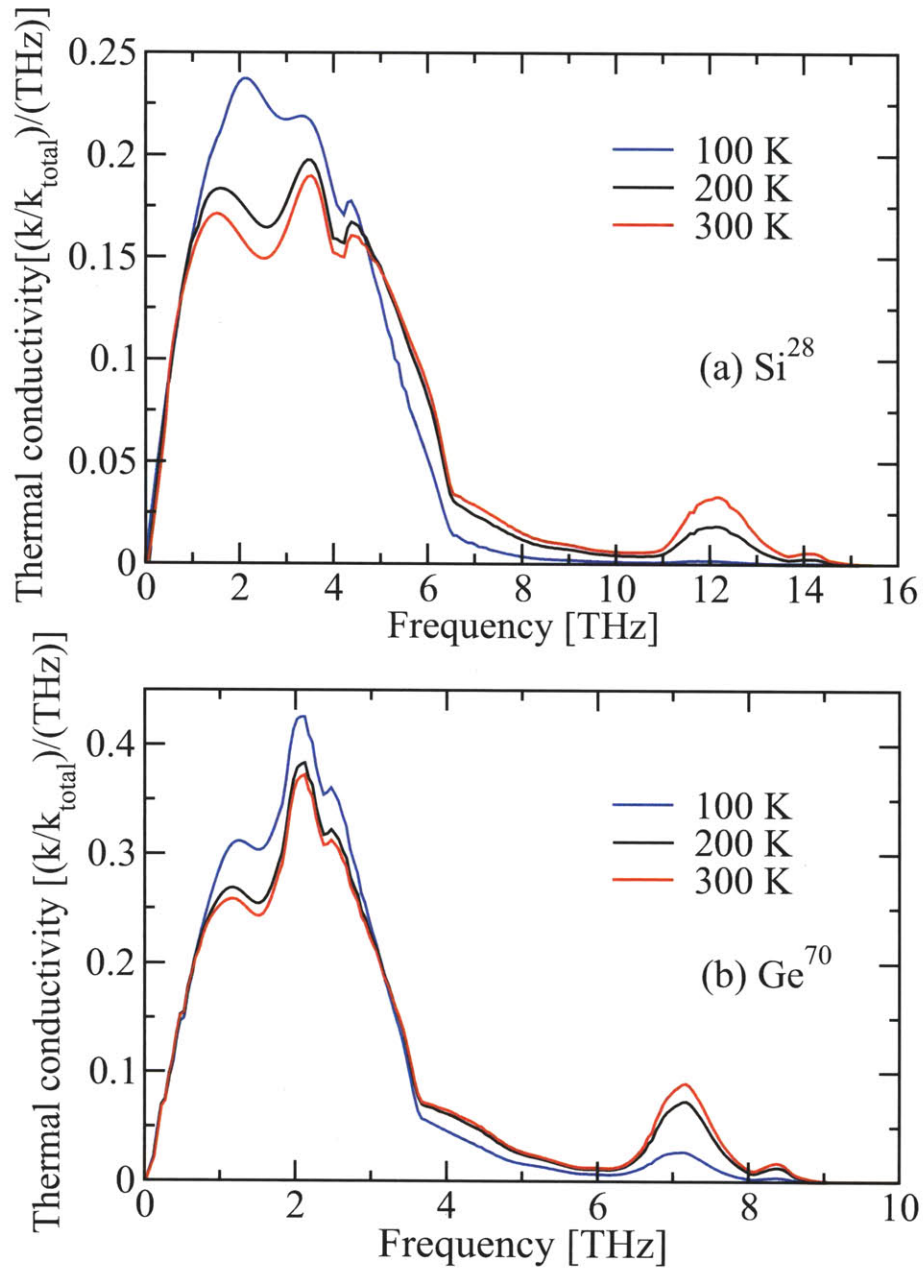
Figure 3-10: Frequency dependence of the thermal conductivity in (a) Si[28] and (b) Ge[70].
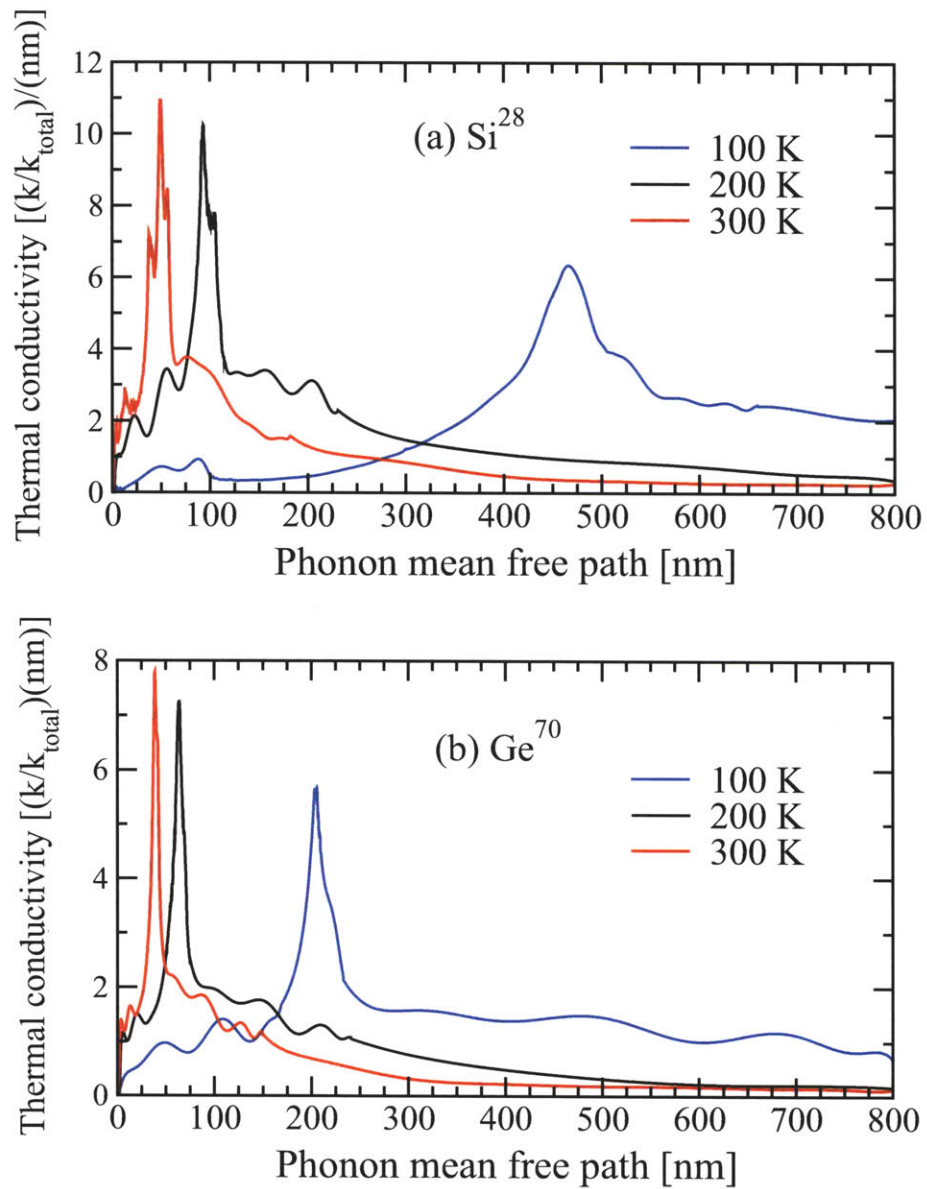
Figure 3-11: Dependence of the thermal conductivity on phonon mean free paths in (a) Si^{28}. Peak contribution to thermal conductivity at 300 K comes from phonons of mean free path around 50 nm. However, as shown by the long tail present even higher mean free path phonons make significant contributions to thermal conductivity. (b) Same for Ge^{70}.

nanostructuring. Indeed room temperature thermal conductivity of polycrystalline silicon was measured to be almost an order of magnitude lower than that of single-crystal silicon [67].

3.6 Full iterative solution

In the previous sections the thermal conductivity was computed by solving the Boltzmann transport equation in the single-mode relaxation time approximation. However, the Boltzmann transport equation can be solved exactly using a self-consistent iterative solution [30, 17]. In this section, following Ref. [17], the full iterative solution is implemented, and the methodology presented.

Rewriting the phonon Boltzmann equation (PBE) as

$$-c(qs).\nabla T \left(\frac{\partial \bar{n}_{qs}}{\partial T} \right) = \sum_{q's',s''} \left[\widetilde{P}_{qs,q's'}^{q''s''} (\Psi_q^s + \Psi_{q'}^{s'} - \Psi_{q''}^{s''}) + \frac{1}{2} \widetilde{P}_{qs}^{q's',q''s''} (\Psi_q^s - \Psi_{q'}^{s'} - \Psi_{q''}^{s''}) \right],$$

(3.76)

using the shorthand λ for the vibration mode (qs) and defining $\Psi_q^s = \sum_\alpha F_{\lambda\alpha}(\partial T/\partial x_\alpha)$ and realizing that

$$\frac{\partial \bar{n}_\lambda}{\partial T} = \frac{\hbar\omega(\lambda)\bar{n}_\lambda(\bar{n}_\lambda + 1)}{k_B T^2}$$

(3.77)

the PBE can be rewritten as

$$-c_\alpha(\lambda) \frac{\hbar\omega(\lambda)\bar{n}_\lambda(\bar{n}_\lambda + 1)}{k_B T^2} = \sum_{\lambda',\lambda''} \left[\widetilde{P}_{\lambda,\lambda'}^{\lambda''} (F_{\lambda\alpha} + F_{\lambda'\alpha} - F_{\lambda''\alpha}) + \frac{1}{2} \widetilde{P}_{\lambda}^{\lambda',\lambda''} (F_{\lambda\alpha} - F_{\lambda'\alpha} - F_{\lambda''\alpha}) \right]$$

(3.78)

where it is understood that the sum over λ'' only involves the sum over the mode s''.

Defining

69
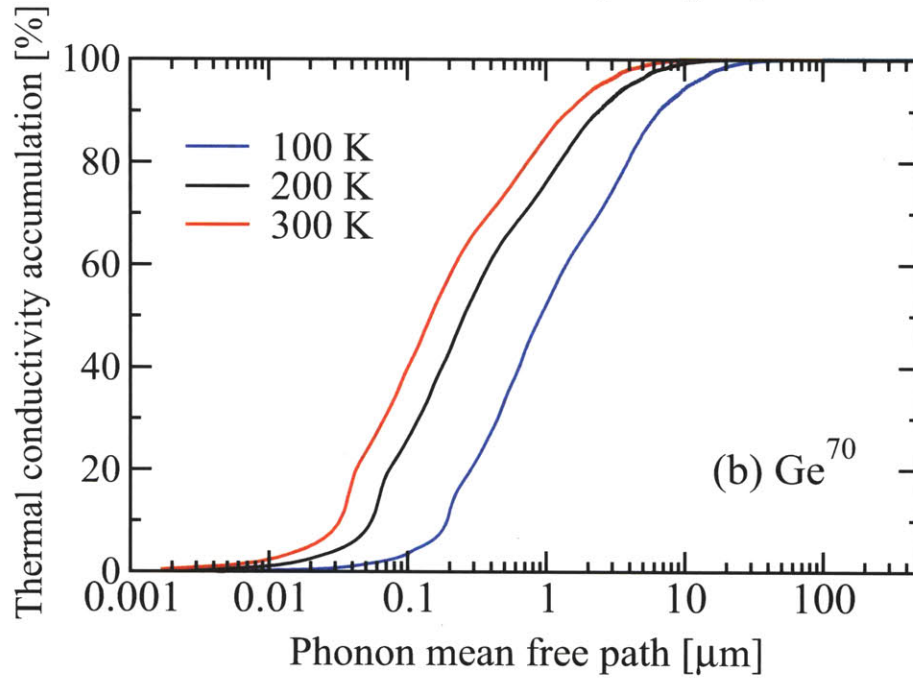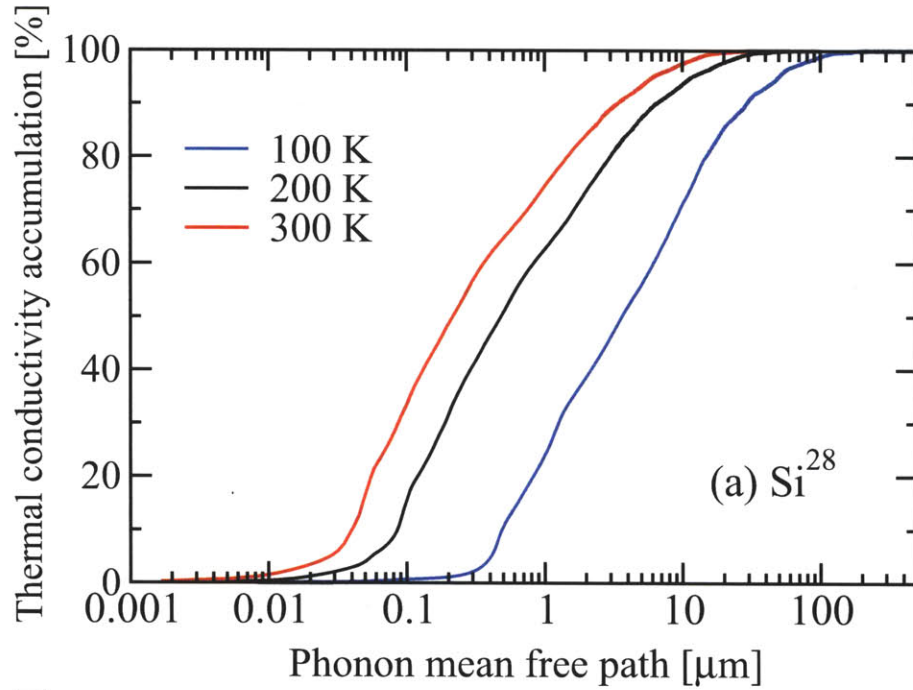
Figure 3-12: Thermal conductivity accumulation with phonon mean free path in (a) Si^{28}. Almost 50% of the heat is conducted by phonons of mean free path longer than 200 nm. This provides avenues to lower thermal conductivity through nanostructuring. (b) Same for Ge^{70}.

$$Q_\lambda = \sum_{\lambda',\lambda''} \left[\widetilde{P}_{\lambda,\lambda'}^{\lambda''} + \frac{1}{2} \widetilde{P}_{\lambda}^{\lambda',\lambda''} \right] \tag{3.79}$$

and

$$-c_\alpha(\lambda) \frac{\hbar\omega(\lambda)\bar{n}_\lambda(\bar{n}_\lambda + 1)}{k_B T^2} = F_{\lambda\alpha}^0 Q_\lambda \tag{3.80}$$

the PBE can be rewritten as

$$F_{\lambda\alpha}^0 Q_\lambda = F_{\lambda\alpha} Q_\lambda - \sum_{\lambda',\lambda''} \left[\widetilde{P}_{\lambda,\lambda'}^{\lambda''}(F_{\lambda''\alpha} - F_{\lambda'\alpha}) + \frac{1}{2} \widetilde{P}_{\lambda}^{\lambda',\lambda''}(F_{\lambda'\alpha} + F_{\lambda''\alpha}) \right], \tag{3.81}$$

and further rewritten as:

$$F_{\lambda\alpha} = F_{\lambda\alpha}^0 + \frac{1}{Q_\lambda} \sum_{\lambda',\lambda''} \left[\widetilde{P}_{\lambda,\lambda'}^{\lambda''}(F_{\lambda''\alpha} - F_{\lambda'\alpha}) + \frac{1}{2} \widetilde{P}_{\lambda}^{\lambda',\lambda''}(F_{\lambda'\alpha} + F_{\lambda''\alpha}) \right]. \tag{3.82}$$

The above equation has to be solved for $F_{\lambda\alpha}$ for all the modes λ on a chosen grid in the first Brillouin zone. The iterative solution starts by assuming that the second term on the right hand side is zero. This gives the zeroth order solution $F_{\lambda\alpha} = F_{\lambda\alpha}^0$. For the next iteration, the required values of $F_{\lambda'\alpha}$ and $F_{\lambda''\alpha}$ are taken from the zeroth order solution. Substituting these into the second term on the right hand side, yields the first-order solution $F_{\lambda\alpha}^1$. Continuing this process yields the converged values of $F_{\lambda\alpha}$.

The thermal conductivity after solving exactly the PBE is obtained as

$$k_{\alpha\beta} = \frac{1}{N_0 \Omega} \sum_\lambda \hbar\omega(\lambda) c_\alpha(\lambda) \bar{n}_\lambda(\bar{n}_\lambda + 1) F_{\lambda\beta}. \tag{3.83}$$

The computed thermal conductivity after self consistently solving the PBE is compared against experimental values in Fig. 3-13. It can be seen that solving the PBE exactly leads to a better agreement with experimentally measured values as compared to the use of the SMRT approximation. However for pure Si[28] and Ge[70]

71
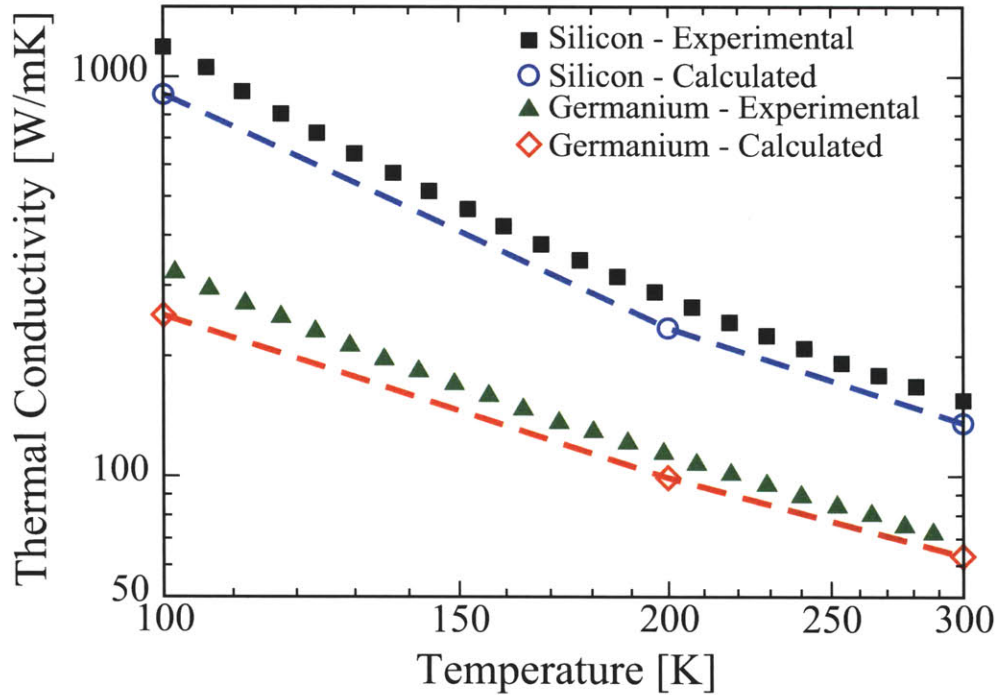
Figure 3-13: Thermal conductivity of Si^{28} and Ge^{70} computed using the full self consistent solution of the phonon Boltzmann transport equation. Experimental values are from Ref. [62] (Si^{28}) and Ref. [63] (Ge^{70}).

the difference between the two results is small. Furthermore, it can be seen that there is still a small disagreement between the computed and the experimentally measured values. This is primarily due to the fact that the anharmonic force constants $\Phi_{\alpha\beta\gamma}(\boldsymbol{ob}, \boldsymbol{h'b'}, \boldsymbol{h''b''})$ were obtained on a 3x3x3 supercell. As shown in Fig. 3-5, there is a small difference in the linewidths computed using $\Phi_{\alpha\beta\gamma}(\boldsymbol{ob}, \boldsymbol{h'b'}, \boldsymbol{h''b''})$ obtained on a 2x2x2 versus a 3x3x3 supercell. Thus the computation of linewidths is not fully converged with respect to the size of the supercell on which the third-order anharmonic force constants were obtained. Computation of the force constants on a supercell larger than 3x3x3 was found computationally too expensive, thus somewhat limiting the accuracy of the final computed thermal conductivity.

Chapter 4

Thermal conductivity of Silicon-Germanium alloys

In thermoelectric materials, the energy conversion efficiency is often characterized by the dimensionless figure of merit $ZT = S^2\sigma T/k$ where S, σ, k and T are the Seebeck coefficient, electrical conductivity, thermal conductivity, and temperature. For decades, it was found difficult to increase the figure of merit beyond ~ 1, rendering these devices too inefficient to be of practical use except in niche applications, such as power generation in space. However, recent advances in nanotechnology have led to renewed interest in thermoelectric devices. A key approach to improve ZT in thermoelectric materials has been to reduce thermal conductivity by increasing phonon scattering either by introducing disorder as in alloys, or nanostructuring [8, 9, 10].

As an example, while ZT in heavily doped n-type single crystal silicon was reported to be about 0.01 at room temperature [6], ZT in nanostructured silicon was measured to be about 0.02 [6], almost 100% higher compared to single crystal silicon. This increase in ZT was due to the significant reduction in thermal conductivity in nanostructured silicon, due to increased scattering of phonons. More recently, Hochbaum *et al.* [9] measured ZT in surface-rough silicon nanowires to be about 0.6 at room temperature, almost 60 times higher than bulk silicon. This increase in ZT was attributed to an almost 100-fold decrease in thermal conductivity with respect

to bulk silicon. Similarly, Boukai *et al.* [10] measured ZT in silicon nanowires to be about 1 at 200 K. This increase was again ascribed to phonon effects.

Due to disorder, thermal conductivity of silicon-germanium alloys is significantly lower than both silicon and germanium. This leads to a higher ZT in SiGe alloys. Vining *et al.* [7] reported a ZT of about 1 in n-type $Si_{0.8}Ge_{0.2}$ alloys and a maximum ZT of about 0.62 in p-type samples. Both measurements were made on samples with grain sizes of the order of microns. Thus low thermal conductivity in SiGe alloys leads to a ZT almost 100 times larger than bulk silicon. However, while ZT in p-type samples with micron-sized grains was measured to be 0.62, nanostructuring to reduce thermal conductivity was found to lead to a ZT of about 0.95 [68], an increase of almost 50%.

Being able to predict thermal conductivity in disordered materials accurately would greatly reduce the cost associated with designing more efficient thermoelectric materials. One of the key parameters deciding whether nanostructuring would result in lower thermal conductivity is the phonon mean free path. If significant heat is conducted by phonons of mean free path larger than a micron, then this provides avenues to lower thermal conductivity by introducing additional scattering mechanisms at nanometer length scales. Accurate prediction of phonon mean free paths can thus help guide the design of nanostructured materials with improved ZT. In Chapter 3, it was demonstrated that first-principles approaches can very accurately predict the thermal conductivity in pure materials, such as Si^{28} and Ge^{70}.

However, prediction of thermal conductivity in disordered systems is more challenging. While mass-disorder plays a key role in lowering thermal conductivity in important thermoelectric materials such as half-Heusler alloys [69] and silicon-germanium alloys, an attempt to predict the magnitude of this effect in SiGe alloys through non-equilibrium molecular dynamics (MD) [33] simulations using the Stillinger-Weber potential [18] was found to result in large discrepancies with measured values. Moreover, the predicted temperature dependence did not agree with experimentally observed behaviour.

Chaudhuri *et al.* [70] studied heat-current in two-and three-dimensional disordered

harmonic crystals in a slab geometry. Expressing the current in terms of a frequency dependent transmission function, they numerically evaluated thermal transport in these systems, and tried to ascertain the finiteness as well as system size dependence of thermal conductivity. However the effect of anharmonicity was not included in the work. Finally Allen and Feldman [71] investigated heat conduction in highly disordered materials where the typical phonon mean free paths are so short that phonon wavelength and mean free path are no longer well defined concepts. Again, the discussion pertained to harmonic solids.

In this Chapter, we will use a first-principles approach to predict the thermal conductivity of silicon-germanium alloys. It would be tempting to compute the thermal conductivity of alloys using the same approach as was implemented for pure silicon and germanium, using larger supercells to take disorder into account. The thermal conductivity is then computed using the phonon modes of these large supercells, with random distributions of silicon and germanium masses. However, this approach does not converge to the alloy thermal conductivity in the limit of an infinitely large supercell. The cause of the failure of this approach is discussed and presented.

The second approach involves replacing the disordered crystal with an ordered one and using the phonon modes of this ordered crystal to compute the thermal conductivity. Both anharmonicity and disorder are treated as perturbations and phonon relaxation times are computed using anharmonic and mass-disorder scattering terms. Disorder therefore leads to scattering in addition to the anharmonic scattering present in pure materials, thereby lowering relaxation times and lowering thermal conductivity. This approach is found to lead to excellent agreement with experimentally measured values and provides guidelines for the design of nanostructured materials.

The two approaches are presented in detail in the following sections.

4.1 Approach based on use of supercells

In this section, the first approach to compute the thermal conductivity of silicon-germanium alloys is presented. This approach involves using large supercells to com-

pute phonon frequencies, group velocities, populations and relaxation times, that together yield the thermal conductivity via Eq. 3.71. Since, the structure of SiGe alloys has been shown to be truly random both experimentally and theoretically [34, 35] with no significant long or short range chemical ordering, disorder can be modelled by randomly allocating masses to be that of Si or Ge, in the ratio corresponding to a desired composition. Naturally occurring Germanium Ge^{nat} is a mixture of five isotopes having an average mass of 72.64 a.m.u [72]; while computing the thermal conductivity of alloys the mass of naturally occurring Ge^{nat} was used.

To compute phonon frequencies, group velocities, populations and relaxation times, second-order $\Phi_{\alpha\beta}(\boldsymbol{ob}, \boldsymbol{hb'})$ and third-order $\Phi_{\alpha\beta\gamma}(\boldsymbol{ob}, \boldsymbol{h'b'}, \boldsymbol{h''b''})$ IFCs need to be known for any composition. For $Si_{0.5}Ge_{0.5}$, these are obtained by using the virtual crystal approximation [44], where the atomic potential at each site is represented by the 50/50 average of the Si and Ge potentials. The use of this virtual crystal potential, along with the second- and third-order density-functional perturbation theory yields the second- and third-order IFC's respectively. For compositions Si_xGe_{1-x} different from $Si_{0.5}Ge_{0.5}$ the second-order and third-order IFCs are obtained by quadratically interpolating between those of Si, the virtual crystal at x=0.5, and Ge. Obtaining IFCs using the virtual crystal approximation ignores the effect of difference in atomic sizes of Si and Ge in lowering thermal conductivity in alloys. However, it is well known that in SiGe alloys mass disorder plays a significantly more dominant role compared to strain disorder [39, 33]; the use of the virtual crystal approximation should therefore lead to only a small error in the estimate of the thermal conductivity.

For any supercell size, the thermal conductivity is taken to be an ensemble average over many different configurations of mass disorder for a particular composition. As supercell size is increased, more long-range disorder can be incorporated. The thermal conductivity at any composition is then finally taken to be the value in the limit of the supercell size approaching infinity. The validity of the virtual crystal approximation for computing the thermal conductivity of SiGe alloys is tested and the results are presented next.
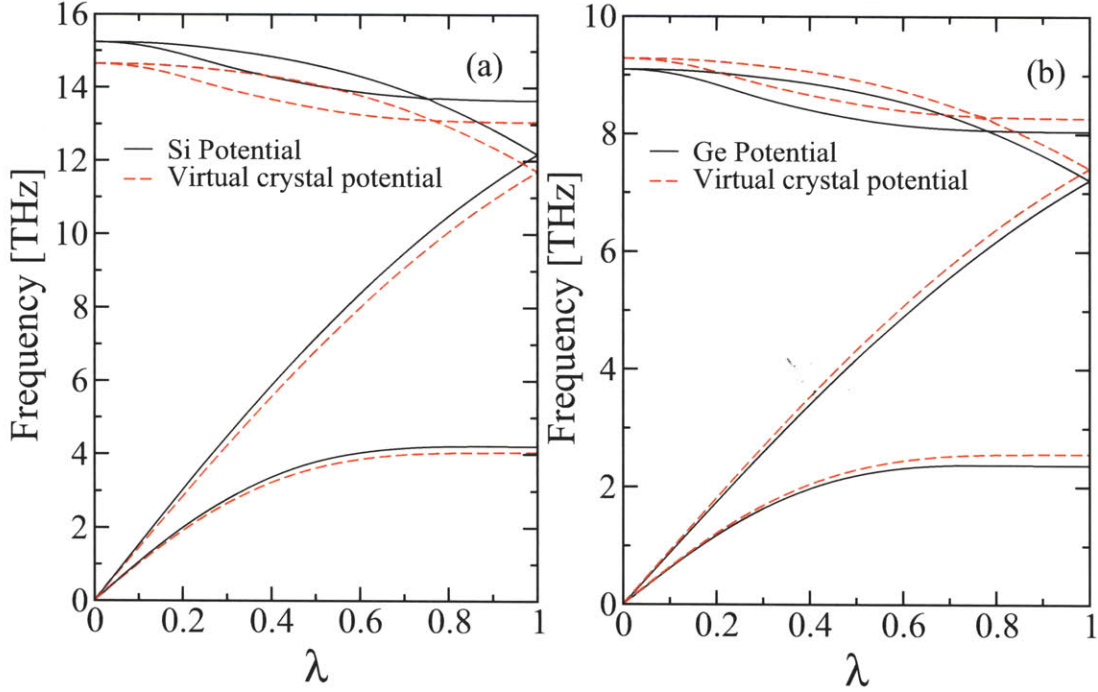
Figure 4-1: Comparison of phonon dispersion along Γ-X $(0,0,\lambda)$ of (a) Si^{28} and (b) Ge^{70} computed using the pseudopotentials of Si and Ge, respectively, with that computed using the virtual crystal potential.

4.1.1 Validity of the virtual crystal approximation

The applicability of the virtual crystal approximation to compute second-order properties such as phonon dispersion is tested first. The phonon dispersions of silicon and germanium computed using the pseudopotentials of Si^{28} and Ge^{70} are compared against those computed using the virtual crystal potential. The dispersions are compared along Γ-X in Figs. 4-1 (a) and (b).

For both Si and Ge, the phonon frequencies computed using the Si and Ge pseudopotentials are close to those computed with the virtual crystal potential. The difference in computed frequencies of longitudinal acoustic modes at $(0,0,1.0)$ is only about 4% for Si and 3% for Ge. Thus virtual crystal approximation can be used very well to predict second-order properties such as phonon dispersions in silicon-germanium systems [73, 74].

Next the phonon linewidth at Γ in Si^{28} is computed using the second-order and

third-order IFCs of Si^{28}, and compared against the value obtained with the second- and third-order IFC's of the virtual crystal. The comparison is presented in Table 4.1 below.

Table 4.1: Comparison of the phonon linewidth $FWHM(cm^{-1})$ of zone center optical mode in Si^{28} computed using the force constants derived from (a) Si^{28} pseudopotential and (b) Virtual crystal.

Temperature	Force constants	
	Silicon	Virtual
0 K	1.40	1.46
300 K	2.77	2.99

The disagreement is about 4% at 0 K and about 8% at 300 K. Thus the use of virtual crystal leads to only a small discrepancy even in the estimate of a property such as a phonon linewidth, that depends upon the third-order interatomic force constants.

Finally, the applicability of the virtual crystal approximation to compute total thermal conductivity is tested. To make the comparison easier, we choose a configuration that has a small unit cell and still allows both Si and Ge atoms to be incorporated. This is the case for $SiGe[001]_{1+1}$ superlattice. The structure has the two atom fcc primitive unit cell, one atom being Si and the other Ge. In the first case, the thermal conductivity is computed using the second-order and third-order interatomic force constants derived using the Si pseudopotential at the Si site and the Ge pseudopotential at the Ge site. In the second case these are derived using the virtual crystal potential at both the sites. The comparison is presented in Table 4.2.

Thus the discrepancy in computing the thermal conductivity through the use of virtual crystal potential is less than 10%.

4.1.2 Application to thermal conductivity of $Si_{0.5}Ge_{0.5}$

After the harmonic and anharmonic IFC's are obtained using the virtual crystal pseudopotential, the disorder is simulated by randomly allocating masses, either of Si

78

Table 4.2: Comparison of the thermal conductivity (in W/mK) of SiGe$[001]_{1+1}$ superlattice computed using force constants of (a) Si and Ge pseudopotentials and (b) Virtual crystal

	Force constants	
Temperature	Si,Ge	Virtual
100 K	648	606
150 K	363	336
200 K	252	233

or Ge, to the atomic sites in the supercell but without relaxing the ions from the ideal configuration. The thermal conductivity is calculated in the single mode relaxation time approximation using Eq. 3.71. While the thermal conductivity of isotopically pure Si and Ge was calculated using the primitive two-atom unit cell, the thermal conductivity of the $Si_{0.5}Ge_{0.5}$ alloy is calculated for larger supercells and the result is then extrapolated to infinity. This value is taken to be the thermal conductivity of the $Si_{0.5}Ge_{0.5}$ alloy.

First, the variation of phonon relaxation times with increase in supercell size is discussed. The anharmonic three-phonon relaxation times are computed using Eq. 3.68. However, larger supercell corresponds to a smaller Brillouin zone and typically a smaller q' grid is required for the convergence of the phonon linewidth. Second, the number of vibration modes s', s'' at each q', q'' in the Brillouin zone is equal to three times the number of atoms in the supercell. This number increases as the third power of the supercell linear dimensions, and becomes 48 for a 2x2x2 supercell, and 384 for a 4x4x4 supercell. This makes the computation of phonon relaxation times expensive, and a 4x4x4 supercell is the largest supercell for which they can be computed. For supercells 5x5x5 and larger, the computational cost is prohibitively large.

The phonon scattering rate as determined by Eq. 3.68 depends upon both the strength of the three-phonon coupling matrix elements $|\widetilde{V}_3(-qs, q's', q''s'')|$ as well as the phase space available for scattering, as determined by

79

$$\chi = \frac{1}{N(3N_{atom})^2} \sum_{q's',s''} \Big[2\delta(\omega(\boldsymbol{q}s) - \omega(\boldsymbol{q}'s') - \omega(\boldsymbol{q}''s'')) +$$
$$\delta(\omega(\boldsymbol{q}s) - \omega(\boldsymbol{q}'s') - \omega(\boldsymbol{q}''s'')) \Big].$$

(4.1)

In the above equation $1/[N(3N_{atom})^2]$ is a normalization factor, where N is the size of the $\boldsymbol{q}'$ grid in the Brillouin zone and N_{atom} is the number of atoms in the supercell. Mass disorder modifies the three-phonon scattering rate in the following ways;

- Disorder leads to lower symmetry, and in turn to a loss of degeneracy. Phonon modes become smeared out over the entire frequency range, changing the number of scattering channels (i.e. phase space, χ) available for the scattering of any particular phonon mode.

- Phonon scattering also depends on the strength of the three-phonon coupling matrix elements. These matrix elements (Eq. 3.40) are related to the third-order anharmonic force constants and the vibration eigenvectors of the three-phonon modes involved in scattering. Mass disorder can change the vibration eigenmodes and therefore alter the strength of these three-phonon scattering matrix elements, thereby changing scattering amplitudes.

The three-phonon relaxation times computed for the composition $Si_{0.5}Ge_{0.5}$ using 2x2x2, 3x3x3 and 4x4x4 supercells are presented in Fig. 4-3 and we find that there is little variation in the anharmonic relaxation times as the supercell size is increased from 2x2x2 to 3x3x3 and to 4x4x4. As indicated above, computing phonon relaxation times for supercells sized 5x5x5 and larger is currently computationally too expensive. However, to accurately extrapolate the thermal conductivity to an infinitely large supercell, phonon relaxation times on supercells sized 5x5x5 and larger are required. Since there is little variation in relaxation times as supercell size is varied from 2x2x2 to 4x4x4, any further variation can be expected to be small and is ignored. The three-phonon relaxation times for supercells sized 5x5x5 or higher are assumed to be properly described by an extrapolation on the 4x4x4 supercell. To implement this,

80
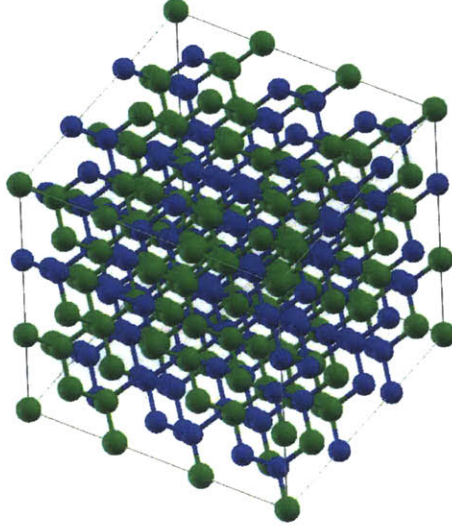
Figure 4-2: A supercell with random distribution of Si and Ge atoms in the composition $Si_{0.5}Ge_{0.5}$.

a fit between relaxation times and phonon frequencies is obtained. For any supercell the three-phonon relaxation time of a phonon mode can be computed through the knowledge of its frequency and this fit.

Next, we discuss the phonon group velocities. Allen and Feldman [71] suggested that as the size of a supercell containing N_{atom} atoms is increased, the system becomes more disordered, causing the N_{atom} phonon bands to repel each other, and reducing bandwidths and group velocities by on average, $1/N_{atom}$. Thus, in the limit of an infinitely large supercell, all phonon modes can be expected to become localized and with zero group velocities. To study group velocities we define here a mean squared group velocity weighted with the density of states.

$$\langle v_\alpha^2 \rangle(\omega) = \frac{\sum\limits_{\substack{qj \\ \omega < \omega(qj) < \omega + d\omega}} v_\alpha^2(qj)}{(d\omega) \times N \times (3N_{atom})}. \tag{4.2}$$

In the above equation N is the size of grid used to discretize the Brillouin zone and N_{atom} is the number of atoms in the supercell. This mean squared velocity is presented as a function of frequency for different supercell sizes in Fig. 4-4. It can be seen that

81
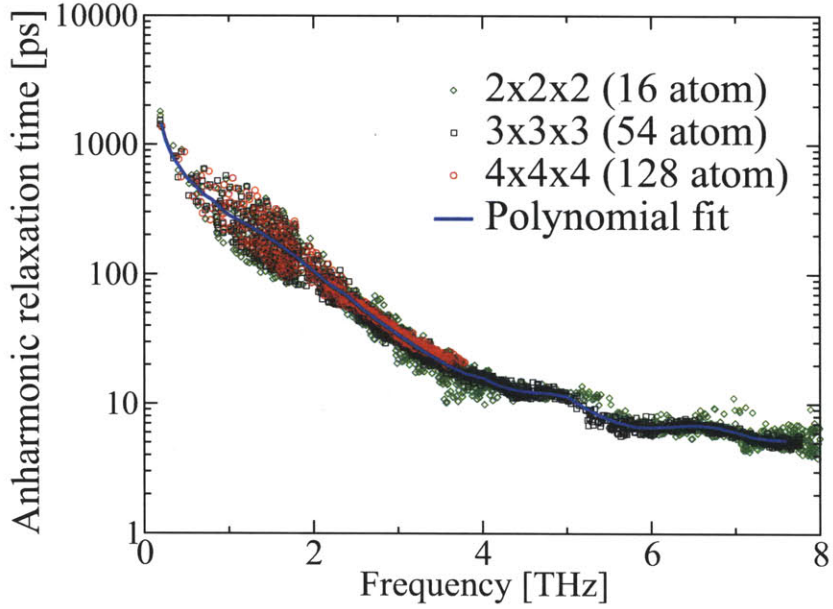
Figure 4-3: Anharmonic phonon relaxation times $Si_{0.5}Ge_{0.5}$ alloy at 300 K as a function of supercell size.

the group velocities decrease with increase in supercell size as suggested by Allen and Feldman [71].

Using the fit we obtained for the phonon relaxation times, and the actual group velocities, it is now possible to compute the thermal conductivity with increasing supercell size. The results are presented in Fig. 4-5(a). Due to the decrease in group velocities, the thermal conductivity drops with increase in supercell size, and plotting the results on log-log scale (Fig. 4-5(b)) reveals that the conductivity drops with the number of atoms in the supercell roughly as $1/N_{atom}^{0.24}$. Thus, in the limit of an infinitely large supercell this approach would yield zero thermal conductivity, and cannot be used to compute alloy thermal conductivities. This result agrees well with the observation made by Lee [75] who stated that disordered systems cannot be understood by forcing them into the mould of ordered systems, but instead that disorder should be treated separately from the beginning.

Below we present another approach which does treat disorder from the beginning by including its effect as an additional two-phonon elastic scattering term.
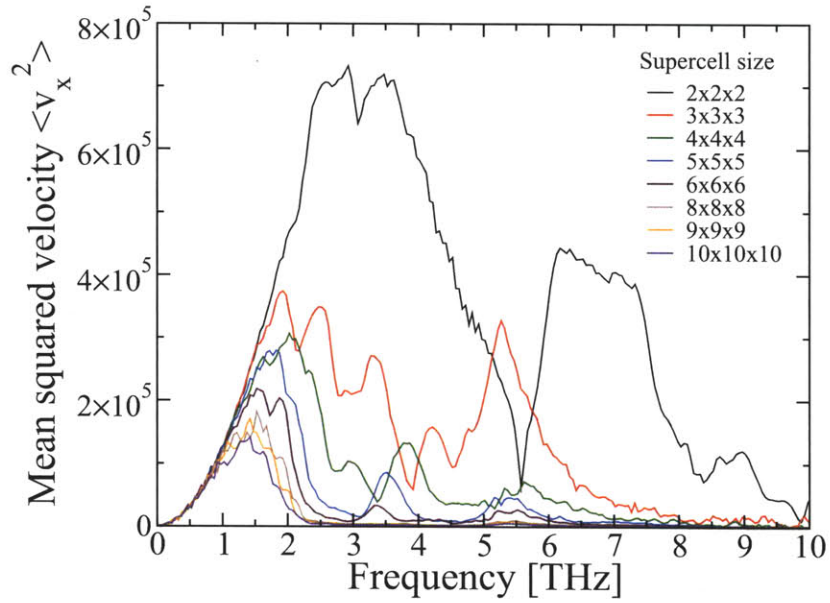
Figure 4-4: Mean squared group velocities as a function of frequency for different supercell sizes.
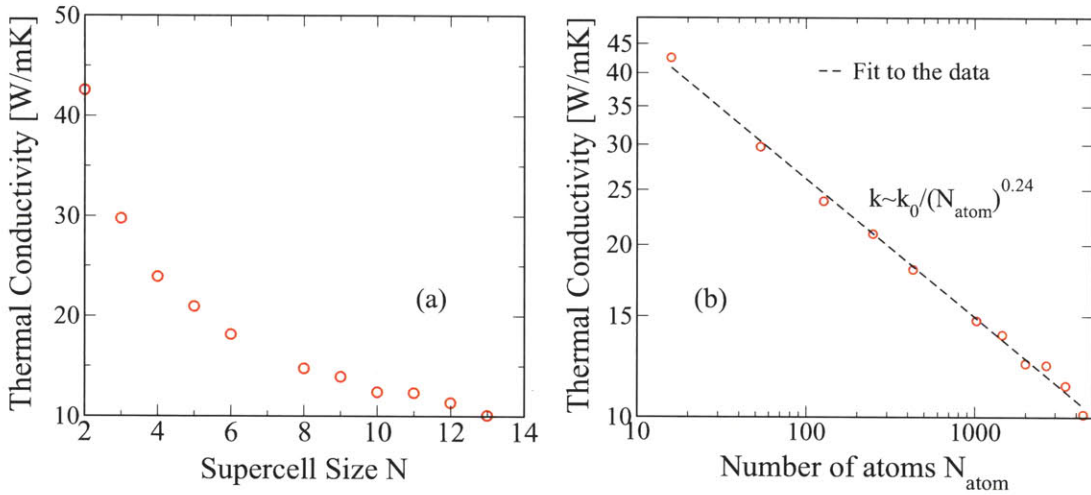
Figure 4-5: (a)Thermal conductivity of $Si_{0.5}Ge_{0.5}$ as a function of the supercell size at 300 K (b) Same on a log-log scale.

4.2 Approach based on perturbation theory for the virtual crystal

Abeles [39] first introduced the idea of computing the thermal conductivity of SiGe alloys by replacing the disordered crystal with an ordered one and treating both disorder and anharmonicity as perturbations. In this phenomenological model the net scattering rate of a phonon mode is computed as the sum of the scattering due to mass disorder and anharmonicity. The mass disorder contribution is taken to be $\tau^{-1} = \omega^4 V_0 g/(4\pi v^3)$, in analogy with the result of Klemens [76] for point-defect scattering, where V_0 is the volume per unit atom, v is the branch-averaged sound velocity, $g = \sum_i f_i (1 - m_i/\bar{m})^2$ is a measure of the mass disorder, f_i and m_i are the concentration and the atomic mass of species i and $\bar{m}$ is the average mass for the given composition. For the anharmonic contribution, the low-frequency limit of normal $(B_1\omega^2)$ and umklapp $(B_2\omega^2)$ processes is used to estimate anharmonic scattering, leaving B_1 and B_2 as free parameters. The use of these fitting parameters allows to obtain good agreement with experiments, but also limits the predictive ability of these models.

Here we follow Ref. [39], but we compute from first-principles all parameters necessary to estimate the thermal conductivity. For any composition, the disordered crystal is replaced with an ordered (average) crystal which has a 2-atom fcc unit cell and lattice parameter, mass and force constants appropriate to that composition. The mass of an atom in this ordered (average) crystal is taken to be a linear interpolation between the masses of Si and Ge for any composition, $Si_x Ge_{1-x}$,

$$m = x m_{Si} + (1-x) m_{Ge}. \tag{4.3}$$

For $Si_{0.5}Ge_{0.5}$, the force constants are obtained by using the virtual crystal approximation [73, 44], where the atomic potential at each site is represented by the average of the Si and Ge potentials. Second-order and third-order density-functional perturbation theory along with this virtual crystal potential yield the second-order $\Phi_{\alpha\beta}(lb, l'b')$

and third-order $\Phi_{\alpha\beta\gamma}(\boldsymbol{lb}, \boldsymbol{l'b'}, \boldsymbol{l''b''})$ interatomic force constants respectively. The lattice parameter for $Si_{0.5}Ge_{0.5}$ is obtained by minimising the energy with respect to the volume of the unit cell using the virtual crystal potential. For compositions Si_xGe_{1-x} different from $Si_{0.5}Ge_{0.5}$ the interatomic force constants and the lattice parameter are obtained by quadratically interpolating between those of Si, the virtual crystal potential at x=0.5, and Ge.

For any composition, we compute the phonon modes of this ordered (average) crystal from the interpolated force constants and mass and derive from these the frequencies, group velocities and populations that enter into the calculation of thermal conductivity. The scattering rate of a phonon mode $\boldsymbol{q}s$ where $\boldsymbol{q}$ is the wave-vector and s is the phonon branch, is taken to be the sum of a term describing harmonic scattering due to mass disorder and a term describing anharmonic scattering, as in Matthiessen's rule.

$$\frac{1}{\tau_{qs}} = \frac{1}{\tau_{qs}^{harmonic}} + \frac{1}{\tau_{qs}^{anharmonic}} \tag{4.4}$$

The harmonic scattering rates due to mass disorder are derived using perturbation theory by Tamura [77]. The derivation is presented in the following section. Anharmonic scattering rates are computed based on the perturbation theory for the lowest order three-phonon scattering processes [28] using Eq. 3.68.

Finally, we adopt the single-mode relaxation time (SMRT) approximation [16] as an approximate solution of the Boltzmann transport equation [22, 52]; the thermal conductivity is computed using Eq. 3.71.

4.2.1   Harmonic scattering rate due to mass disorder

We present below the scattering rates due to mass disorder as derived in Ref. [77]. For a crystal with a unit cell containing r atoms, the Hamiltonian can be written as:

$$H = \frac{1}{2} \sum_{lb\alpha} m(\boldsymbol{lb}) \dot{u}_\alpha^2(\boldsymbol{lb}) + V_2 \tag{4.5}$$

85

where u represents the magnitude of the displacement of an atom, l represents the position of the unit cell, b denotes the position of different atoms in each unit cell, α is the direction of the displacement, and V_2 is the harmonic interatomic potential. If the only disorder present is assumed to be purely mass disorder, then the Hamiltonian can be rewritten in the following form:

$$H = H_0 + H_I \tag{4.6}$$

where

$$H_0 = \frac{1}{2}\sum_{lb\alpha} \bar{m}(b)\dot{u}_\alpha^2(lb) + V_2. \tag{4.7}$$

H_0 is the unperturbed Hamiltonian, that represents the average crystal, and its eigenvalues and eigenfunctions are the phonon energies and phonon eigenvectors corresponding to the vibration modes of the average crystal. H_I is the interaction Hamiltonian, that leads to coupling and hence scattering between the eigenstates of the average crystal. The expression for H_I is given below:

$$\begin{aligned}
H_I &= \frac{1}{2}\sum_{lb\alpha}[m(lb) - \bar{m}(b)]\dot{u}_\alpha^2(lb) \\
&= \frac{1}{2}\sum_{lb\alpha} \Delta m(lb)\dot{u}_\alpha^2(lb).
\end{aligned} \tag{4.8}$$

In the above $\bar{m}(b)$ is the average mass of the atom at location b in the unit cell,

$$\bar{m}(b) = \frac{1}{N}\sum_{l} m(lb) = \sum_{i} f_i(b)m_i(b), \tag{4.9}$$

where $N = N_1 N_2 N_3$ is the crystal size, N_1, N_2 and N_3 being the number of unit cells along the three lattice directions, i represents the different atomic species and f is the concentration. Using Eq. 3.14 and Eq. 3.37, the displacement of any atom can be expressed in terms of vibration eigenvectors $e(b|qs)$ and creation and annihilation operators $a_{qs}^\dagger$ and a_{qs}, where q and s are the wave-vector and branch of phonon qs:

$$u(lb) = -i\sum_{qs} \sqrt{\frac{\hbar}{2m_b N\omega(qs)}} e(b|qs)(a_{qs}^\dagger - a_{-qs})e^{iq.l}. \tag{4.10}$$

In the above, the time dependence $exp(i\omega t)$ is omitted as it only contributes a phase factor which yields unity when the scattering rate amplitudes are computed. The time derivative (omitting the term $exp(i\omega t)$), can be written as

$$\dot{u}(lb) = -i \sum_{qs} \sqrt{\frac{\hbar \omega(qs)}{2m_b N}} e(b|qs)(a_{qs}^\dagger - a_{-qs})e^{iq.l}. \tag{4.11}$$

Substituting the above expression into the interaction Hamiltonian, we obtain,

$$H_I = \frac{\hbar}{4} \sum_b \sum_{qq'} \sum_{ss'} \sum_l [\omega(qs)\omega(q's')]^{1/2} \frac{\Delta m(lb)}{Nm_b}$$
$$\times e(b|qs).e(b|q's')[a_{-qs}a_{q's'}^\dagger + a_{qs}^\dagger a_{-q's'}]e^{iq.l}e^{iq'.l}. \tag{4.12}$$

In the above only those combinations of annihilation and creation operator have been retained that lead to a physically possible scattering process. To further simplify the above, following transformation is introduced:

$$\frac{\Delta m(lb)}{m_b} = \sum_Q \Delta \widetilde{M}_b(Q)e^{iQ.l} \tag{4.13}$$

$$\Delta \widetilde{M}_b(Q) = \frac{1}{N} \sum_l \Delta M(lb)e^{-iQ.l}, \tag{4.14}$$

where $\Delta M(lb) = \Delta m(lb)/m_b$. Using the above transformations, the interaction Hamiltonian can be rewritten as:

$$H_I = \frac{\hbar}{4} \sum_b \sum_{qq'Q} \sum_{ss'} [\omega(qs)\omega(q's')]^{1/2} \Delta \widetilde{M}_b(Q)$$
$$\times e(b|qs).e(b|q's')[a_{-qs}a_{q's'}^\dagger + a_{qs}^\dagger a_{-q's'}] \sum_l e^{i(q+q'+Q).l}; \tag{4.15}$$

the summation over l yields the delta function $\delta(q + q' + Q)$ and we obtain

$$H_I = \frac{\hbar}{4} \sum_b \sum_{qq'Q} \sum_{ss'} [\omega(qs)\omega(q's')]^{1/2} \delta(q + q' + Q) \Delta \widetilde{M}_b(Q)$$
$$\times e(b|qs).e(b|q's')[a_{-qs}a_{q's'}^\dagger + a_{qs}^\dagger a_{-q's'}]. \tag{4.16}$$

87

As for the case of three-phonon scattering, the phonon scattering rate due to mass-disorder can be now computed using the Fermi's golden rule,

$$P_i^f = \frac{2\pi}{\hbar} |\langle f|H_I|i\rangle|^2 \delta(E_f - E_i). \tag{4.17}$$

The net scattering rate of a phonon mode is given by

$$-\frac{\partial n_{qs}}{\partial t}\bigg|_{scatt} = \sum_{q's'} (P_{qs}^{q's'} - P_{q's'}^{qs}), \tag{4.18}$$

where

$$P_{qs}^{q's'} = \frac{\pi}{2} n_{qs}(n_{q's'} + 1)\omega(qs)\omega(q's') \left| \sum_{bQ} \Delta\widetilde{M}_b(Q)e(b|qs).e^*(b|q's')\delta(q + q' + Q) \right|^2$$

$$\times \delta[\omega(qs) - \omega(q's')]. \tag{4.19}$$

Writing $\omega(qs)$ as simply ω, i.e. $\omega \equiv \omega(qs)$, and realizing that energy conservation leads to $\omega(qs) = \omega(q's')$, the above expression can be rewritten as

$$P_{qs}^{q's'} = \frac{\pi}{2} n_{qs}(n_{q's'} + 1)\omega^2 \left| \sum_{bQ} \Delta\widetilde{M}_b(Q)e(b|qs).e^*(b|q's')\delta(q + q' + Q) \right|^2$$

$$\times \delta[\omega - \omega(q's')]. \tag{4.20}$$

Similarly

$$P_{q's'}^{qs} = \frac{\pi}{2}(n_{qs} + 1)n_{q's'}\omega^2 \left| \sum_{bQ} \Delta\widetilde{M}_b(Q)e(b|qs).e^*(b|q's')\delta(q + q' + Q) \right|^2$$

$$\times \delta[\omega - \omega(q's')]. \tag{4.21}$$

Substituting Eqs. 4.20 and 4.21 into Eq. 4.18, the scattering rate of phonon mode qs

can be written as

$$-\frac{\partial n_{qs}}{\partial t}\bigg|_{scatt} = \frac{\pi}{2}\omega^2 \sum_{q's'} \left| \sum_{bQ} \Delta\widetilde{M}_b(\boldsymbol{Q})e(\boldsymbol{b}|\boldsymbol{q}s).e^*(\boldsymbol{b}|\boldsymbol{q}'s')\delta(\boldsymbol{q}+\boldsymbol{q}'+\boldsymbol{Q}) \right|^2 \delta[\omega - \omega(\boldsymbol{q}'s')]$$

$$\times [n_{qs}(n_{q's'}+1) - (n_{qs}+1)n_{q's'}].$$

$$(4.22)$$

The term $[n_{qs}(n_{q's'}+1) - (n_{qs}+1)n_{q's'}]$ can be simplified by linearising the perturbed phonon population n_{qs} in terms of equilibrium population $\bar{n}_{qs}$ and a first order perturbation δn_{qs} to yield,

$$n_{qs}(n_{q's'}+1) - (n_{qs}+1)n_{q's'} = (\bar{n}_{qs} - \bar{n}_{q's'}) + (\delta n_{qs} - \delta n_{q's'})$$

$$= \delta n_{qs} - \delta n_{q's'}.$$

$$(4.23)$$

In the above use is made of the energy conservation for the scattering process, i.e. $\omega(\boldsymbol{q}s) = \omega(\boldsymbol{q}'s')$ leading to $\bar{n}_{qs} = \bar{n}_{q's'}$. Using the single-mode relaxation time approximation, where it is assumed that only the mode $\boldsymbol{q}s$ relaxes to its equilibrium state while other modes remain in equilibrium, i.e. $\delta n_{q's'} = 0$, Eq. 4.23 reduces to,

$$n_{qs}(n_{q's'}+1) - (n_{qs}+1)n_{q's'} = \delta n_{qs}$$

$$(4.24)$$

Using the above, the net scattering rate can now be written in terms of the perturbation in phonon population of the mode $\boldsymbol{q}s$ and a relaxation time $\tau_{qs}(\omega)$ as,

$$-\frac{\partial n_{qs}}{\partial t}\bigg|_{scatt} = \frac{\delta n_{qs}}{\tau_{qs}(\omega)} = \frac{n_{qs} - \bar{n}_{qs}}{\tau_{qs}(\omega)}$$

$$(4.25)$$

where the relaxation time $\tau_{qs}(\omega)$ is given by

$$\frac{1}{\tau_{qs}(\omega)} = \frac{\pi}{2}\omega^2(\boldsymbol{q}s) \sum_{q's'} \delta[\omega - \omega(\boldsymbol{q}'s')] \left| \sum_{bQ} \Delta\widetilde{M}_b(\boldsymbol{Q})e(\boldsymbol{b}|\boldsymbol{q}s).e^*(\boldsymbol{b}|\boldsymbol{q}'s')\delta(\boldsymbol{q}+\boldsymbol{q}'+\boldsymbol{Q}) \right|^2.$$

$$(4.26)$$

89

To simplify the above expression, we note that

$$\Delta \widetilde{M}_b(\boldsymbol{Q})\Delta \widetilde{M}_{b'}^*(\boldsymbol{Q'}) = \frac{1}{N^2}\sum_{ll'}\Delta M(\boldsymbol{bl})\Delta M(\boldsymbol{b'l'})e^{-i[\boldsymbol{Q.l}-\boldsymbol{Q'.l'}]}. \qquad (4.27)$$

Taking an ensemble average over a random distribution of masses yields

$$\left\langle \Delta M(\boldsymbol{bl})\Delta M(\boldsymbol{b'l'})\right\rangle_{ave} = \left\langle [\Delta M(\boldsymbol{bl})]^2\right\rangle_{ave}\delta_{ll'}\delta_{bb'} = g_2(\boldsymbol{b})\delta_{ll'}\delta_{bb'}, \qquad (4.28)$$

where

$$g_2(\boldsymbol{b}) = \sum_i f_i(\boldsymbol{b})[1 - m_i(b)/\bar{m}(\boldsymbol{b})]^2; \qquad (4.29)$$

here, $f_i(\boldsymbol{b})$ is the concentration of species i at location $\boldsymbol{b}$ in the unit cell. Note that the above allows sub-lattice disorder to be taken into account. Making use of the Eq. 4.28, Eq. 4.27 can be written as

$$\Delta \widetilde{M}_b(\boldsymbol{Q})\Delta \widetilde{M}_{b'}^*(\boldsymbol{Q'}) = \frac{1}{N}g_2(\boldsymbol{b})\delta_{bb'}\Delta(\boldsymbol{Q}-\boldsymbol{Q'}). \qquad (4.30)$$

Substituting Eq. 4.30 into Eq. 4.26, the scattering rate can now be written as

$$\frac{1}{\tau_{qs}(\omega)} = \frac{\pi}{2N}\omega^2(\boldsymbol{q}s)\sum_{q's'}\delta[\omega - \omega(\boldsymbol{q's'})]\sum_b g_2(\boldsymbol{b})|e(\boldsymbol{b}|\boldsymbol{q}s).e^*(\boldsymbol{b}|\boldsymbol{q's'})|^2. \qquad (4.31)$$

To make further progress, we use the following property of the eigenvectors related to the cubic symmetry of fcc unit cell [77],

$$\sum_{qs} f(\boldsymbol{q}s)e_\alpha^*(\boldsymbol{b}|\boldsymbol{q}s).e_\beta(\boldsymbol{b}|\boldsymbol{q}s) = \frac{\delta_{\alpha\beta}}{6}\sum_{qs} f(\boldsymbol{q}s). \qquad (4.32)$$

In the above $f(\boldsymbol{q}s)$ is any function that depends upon $\boldsymbol{q}$ and s through $\omega(\boldsymbol{q}s)$. Using Eq. 4.32, the scattering rate can be rewritten as

$$\frac{1}{\tau_{qs}(\omega)} = \frac{\pi}{12N}\omega^2(\boldsymbol{q}s)\sum_{q's'}\delta[\omega - \omega(\boldsymbol{q's'})]. \qquad (4.33)$$

Realizing that $\delta[\omega - \omega(\boldsymbol{q's'})]/N = D(\omega)$ where $D(\omega)$ is the density of states corre-

sponding to the two-atom unit cell ($\int D(\omega)d\omega = 6$), the above can be written as:

$$\frac{1}{\tau_{qs}(\omega)} = \frac{\pi}{12} g_2 \omega^2(\boldsymbol{q}s) D(\omega) \tag{4.34}$$

where

$$g_2 = \sum_b g_2(\boldsymbol{b}) \tag{4.35}$$

Using the density of states normalized to unity $\tilde{D}(\omega) = D(\omega)/6$ such that $\int \tilde{D}(\omega)d\omega = 1$, the scattering rate can be written as

$$\frac{1}{\tau_{qs}(\omega)} = \frac{\pi}{2} g_2 \omega^2(\boldsymbol{q}s) \tilde{D}(\omega). \tag{4.36}$$

Typically the low frequency limit of this expression is used to estimate elastic phonon scattering rates. We now derive the limit of the above expression as $\omega \to 0$. Rewriting

$$\frac{1}{\tau_{qs}(\omega)} = \frac{\pi}{6} g_2 \omega^2(\boldsymbol{q}s) V_0 D'(\omega) \tag{4.37}$$

where $D'(\omega)$ is the density of states per unit volume, $D'(\omega) = D(\omega)/V$, V is the volume of the unit cell, and V_0 is the volume per unit atom. The density of states per unit volume is given by

$$D'(\omega) = \frac{1}{(2\pi)^3} \sum_j \int \frac{dS_\omega(\boldsymbol{q}s)}{v_s(\boldsymbol{q})} \tag{4.38}$$

where dS_ω is an element of area on the constant frequency surface, and v_s is the group velocity of the phonons. We finally obtain

$$\frac{1}{\tau_{qs}(\omega)} = \frac{V_0}{4\pi} g_2 \frac{\omega^4}{\langle c^3(\omega) \rangle} \tag{4.39}$$

where we define

$$\frac{1}{\langle c^3(\omega) \rangle} \equiv \frac{1}{3} \sum_s \int_\omega \frac{d\Omega(\boldsymbol{q})}{4\pi} \frac{1}{c_s^2(\boldsymbol{q}) v_s(\boldsymbol{q}) cos[\xi_s(\boldsymbol{q})]} \tag{4.40}$$

91

In the above c_s is the phase velocity, and ξ_s is the angle between $\boldsymbol{q}$ and the group-velocity vector. The integral is performed over the solid angle $\Omega(\boldsymbol{q})$ in the wave vector space on a constant frequency surface. In the long wavelength limit, where both c_s and $v_s = c_s/cos\xi_s$ become independent of the magnitude of $\boldsymbol{q}$ or the frequency, the relaxation time exhibits the characteristic ω^{-4} behaviour. For $Si_{0.5}Ge_{0.5}$ composition, the above expression is numerically evaluated to be

$$
\begin{aligned}
\tau_{qs}^{-1}(\omega \to 0) &= \frac{V_0}{4\pi} g_2 \frac{\omega^4}{\langle c^3(0) \rangle} \\
&= 4.43 \times 10^{-42} sec^3 \times \omega^4
\end{aligned}
\tag{4.41}
$$

where ω is in rad/sec.

Though the expression for harmonic scattering (Eq. 4.36) is valid for small mass disorder, its use has been found to lead to good agreement with experimentally measured phonon linewidths, e.g even in the case of a $Ni_{0.55}Pd_{0.45}$ alloy, where atomic species are chemically similar but mass disorder is large $(m_{Pd}/m_{Ni} = 1.812)$ [78].

The computed harmonic scattering rates for the composition $Si_{0.5}Ge_{0.5}$ are shown by the solid line and the long wavelength limit (represented by Eq. 4.41) is shown by the dashed line in Fig. 4-7(b).

4.2.2 Anharmonic scattering rates

The anharmonic scattering rates are computed based on the lowest-order three-phonon scattering processes in the single-mode relaxation time approximation by using Eq. 3.68 [13, 28]. These anharmonic scattering rates for any composition are computed first using the phonon modes of the average crystal corresponding to that composition; later we will also incorporate the effect of disorder by performing explicit calculations on supercells with random distributions of Si and Ge masses for the relevant composition. The anharmonic scattering rates for the composition $Si_{0.5}Ge_{0.5}$ computed using the phonon modes of the average crystal at 100 K, 300 K and 500 K are shown in Fig. 4-7(b) by open circles, diamonds and squares respectively.
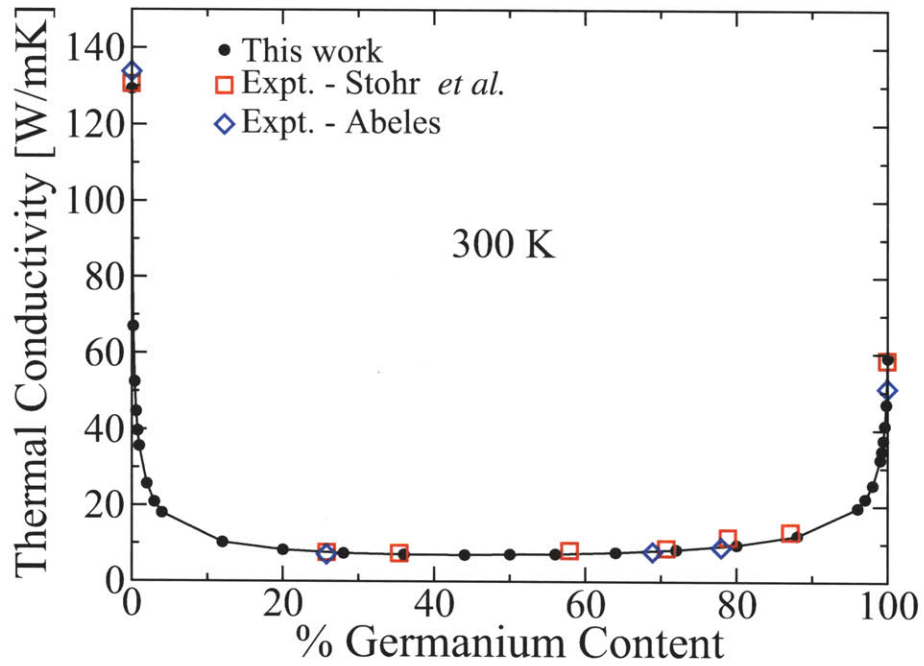
Figure 4-6: Composition dependence of the thermal conductivity in Si_xGe_{1-x} at 300 K. Solid black circles show our predicted thermal conductivities, to be compared with the experimental values of Stohr *et al.*(Ref. [36]) and Abeles (Ref. [39]) (red open squares and blue open diamonds, respectively).
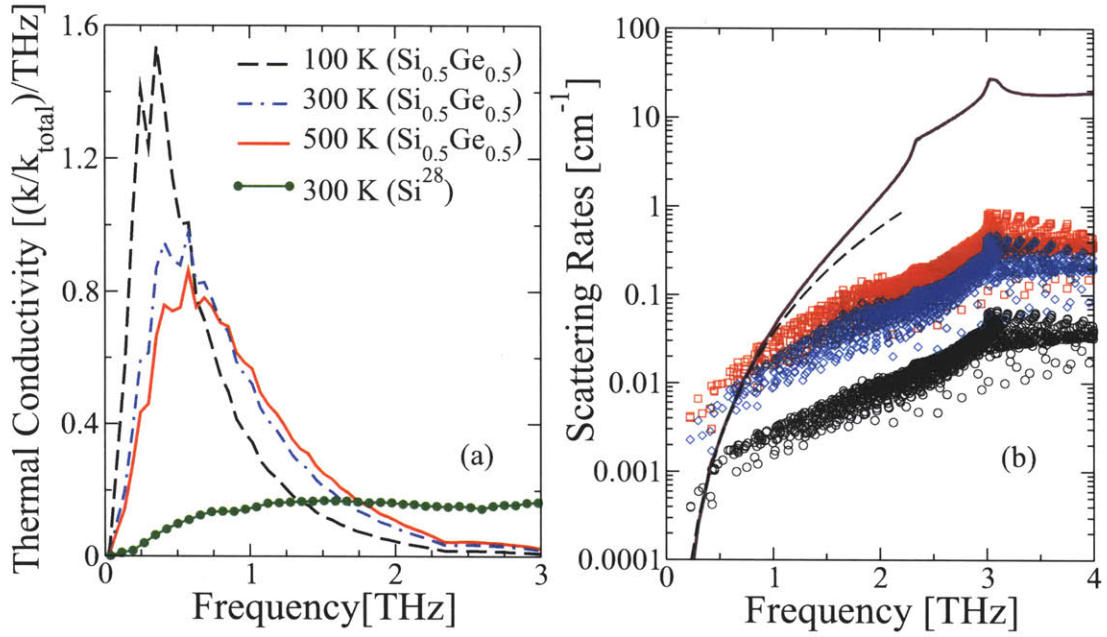
Figure 4-7: (a) Frequency dependence of the thermal conductivity (normalized with respect to total thermal conductivity) for $Si_{0.5}Ge_{0.5}$ and pure silicon.(b) Scattering rates (full width at half maximum) due to harmonic scattering (solid line) and anharmonic scattering (open symbols) in $Si_{0.5}Ge_{0.5}$. Open circles, diamonds, and squares are the anharmonic scattering rates at 100K, 300K and 500K respectively. Below 0.7 THz the mass disorder scattering rate agrees well with Klemens' result (dashed line) for point defect scattering, $\tau_{\lambda a}^{-1} = 4.43 \times 10^{-42} sec^3 \times \omega_\lambda^4$ where ω is in rad/sec.

4.2.3 Alloy thermal conductivity

The approach outlined above yields an excellent agreement between the computed and measured values at 300 K [36, 39] for the alloy thermal conductivity at all compositions (Fig. 4-6). Notably, the thermal conductivity is found to drop sharply after only a small amount of alloying. This is due to the strong harmonic scattering of phonons even in the dilute alloy limit. Our approach predicts that in the composition range $0.2 < x < 0.8$ the alloy thermal conductivity becomes nearly independent of composition, in excellent qualitative and quantitative agreement with experiments.

This low thermal conductivity in Si_xGe_{1-x} with respect to pure Si or pure Ge is better understood from the analysis of the relative contribution of the different scattering mechanisms. As shown in Fig. 4-7(a) for $Si_{0.5}Ge_{0.5}$, thermal conductivity even at temperatures as high as 500 K is dominated by phonon modes below 1 THz (at 100 K, 300 K, and 500 K, respectively, 82%, 65% and 58% of the heat is conducted by phonons of frequency less than 1 THz, while 13%, 23% and 27% is conducted by phonons between 1 and 2 THz; optical frequencies for Si and Ge are 15.67 and 9.27 THz, respectively, at the zone center). In pure silicon, on the other hand, phonon modes up to 6 THz contribute in similar measures to thermal conductivity (see Figs. 3-10 and 4-7(a)); harmonic scattering completely annihilates the heat carrying ability of these higher frequency modes (see Fig. 4-7(b)) leading to the observed sudden drop in conductivity.

In order to consider the temperature dependence of heat transport, we looked at the experimental data for $Si_{0.3}Ge_{0.7}$. While disagreement with measured resistivity [38] is less than 10% at 300K, it becomes larger at higher temperatures (open squares in Fig. 4-8). The effect of 4-phonon processes has been estimated to be small [79]; we should note that up to now scattering rates were computed using the phonon modes of the average crystal, without taking into account the effect of a random distribution of masses. To incorporate this effect, we compute the scattering rates using large supercells with explicit random distribution of Si and Ge masses in the relevant compositions. Fig. 4-9(a) shows that for $Si_{0.3}Ge_{0.7}$ the anharmonic
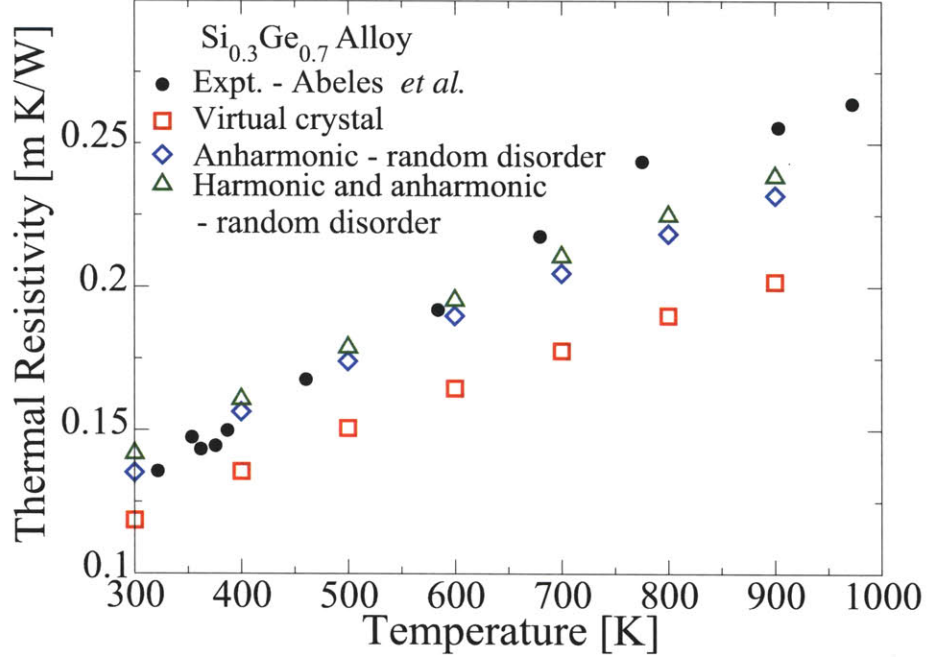
Figure 4-8: Temperature dependence of the thermal resistivity; measured values are from Ref. [38]. The open squares and the open diamonds are the computed values obtained using anharmonic relaxation times of the virtual crystal and the supercell (where disorder is simulated through explicit random distribution of Si and Ge masses appropriate to $Si_{0.3}Ge_{0.7}$) respectively. Open triangles are the computed values obtained by including the effect of random disorder on both harmonic and anharmonic relaxation times.

phonon relaxation times computed using a 4x4x4 supercell (dashed red line) are lower by a factor of ~ 2.0 at the smallest frequencies studied — compared to those obtained using the virtual crystal (solid black line) — with the difference diminishing as the frequency is increased. Using these lower anharmonic lifetimes, and continuing to use the other parameters obtained with the virtual crystal, we find that a good agreement with measured resistivity values is obtained even at higher temperatures (see Fig. 4-8, open diamond). On the other hand, the effect of using real masses is negligible for harmonic scattering in the low-frequency region, due to the negligible changes in phonon density of states at low frequencies (Figs. 4-9(b)), resulting in minimal changes for the thermal resistivity (open triangles in Fig. 4-8).

Mass-disorder thus lowers thermal conductivity through harmonic scattering in the

high-frequency region, and by increasing anharmonic scattering at low frequencies. To understand this latter effect, we perform anharmonic scattering calculations on a 2x2x2 supercell, using 2nd and 3rd order force constants for the composition $Si_{0.3}Ge_{0.7}$. We compute the values of the three-phonon anharmonic coupling matrix elements $|\tilde{V}_3(-\boldsymbol{q}s, \boldsymbol{q}'s', \boldsymbol{q}''s'')|^2$ involved in the scattering of a low-frequency phonon mode $(\boldsymbol{q}s)$, when the mode $(\boldsymbol{q}'s')$ is varied over the entire Brillouin zone. The $|\tilde{V}_3|^2$ values are computed first for the case where all the atoms have an average mass corresponding to $Si_{0.3}Ge_{0.7}$, and second with real Si and Ge masses randomly distributed according to the above composition. We find that in the first case a large fraction of channels have negligibly small $|\tilde{V}_3|^2$ (Fig. 4-10(a)), while in the second case the number of channels with large $|\tilde{V}_3|^2$ increases significantly (Fig. 4-10(b)), causing the overall anharmonic scattering rate to increase by almost a factor 2. To explain this increase, we notice that

$$\tilde{V}_3(\boldsymbol{q}s, \boldsymbol{q}'s', \boldsymbol{q}''s'') \sim \sum_{b,b',b''} \sum_{\alpha\beta\gamma} \Phi_{\alpha\beta\gamma}(\boldsymbol{q}b, \boldsymbol{q}'b', \boldsymbol{q}''b'') \frac{e_\alpha(\boldsymbol{b}|\boldsymbol{q}s)}{\sqrt{m_b}} \frac{e_\beta(\boldsymbol{b}|\boldsymbol{q}'s')}{\sqrt{m_{b'}}} \frac{e_\gamma(\boldsymbol{b}|\boldsymbol{q}''s'')}{\sqrt{m_{b''}}}$$

(4.42)

where κ denotes the atoms in the supercell, α is the Cartesian direction, Φ is the Fourier transformed anharmonic force constants, M is the atomic mass, and e's are the vibration eigenvectors. Typically, it is found that the largest values of Φ involve the same atom and vibration along different Cartesian directions, while other terms are orders of magnitude smaller. Therefore $V_3 \sim \chi S$ where

$$S = \sum_b \sum_{\alpha \neq \beta \neq \gamma} \frac{e_\alpha(\boldsymbol{b}|\boldsymbol{q}s)}{\sqrt{m_b}} \frac{e_\beta(\boldsymbol{b}|\boldsymbol{q}'s')}{\sqrt{m_{b'}}} \frac{e_\gamma(\boldsymbol{b}|\boldsymbol{q}''s'')}{\sqrt{m_{b''}}}$$

(4.43)

This is confirmed by the strong correlation between $|S|^2$ (Figs. 4-10(c) and (d)) and $|\tilde{V}_3|^2$ ($|S|^2$ can be thought of as an "eigenvector overlap"). Since the same anharmonic force constants are used for both cases of average or random masses, the difference in $\tilde{V}_3$ originates from the vibration eigenmodes. The small values of $|S|^2$ (Fig. 4-10(c)) in the average case indicate a cancellation of terms involved in the summation

97
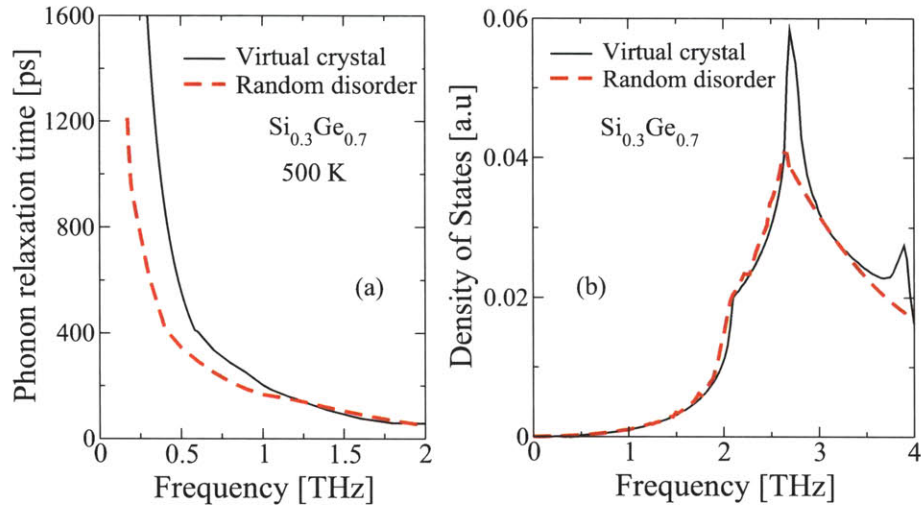
Figure 4-9: a) Anharmonic relaxation times and (b) Phonon density of states – computed using the virtual crystal (solid black line) and a 4x4x4 supercell (dashed red line) with explicit random distribution of Si and Ge masses.
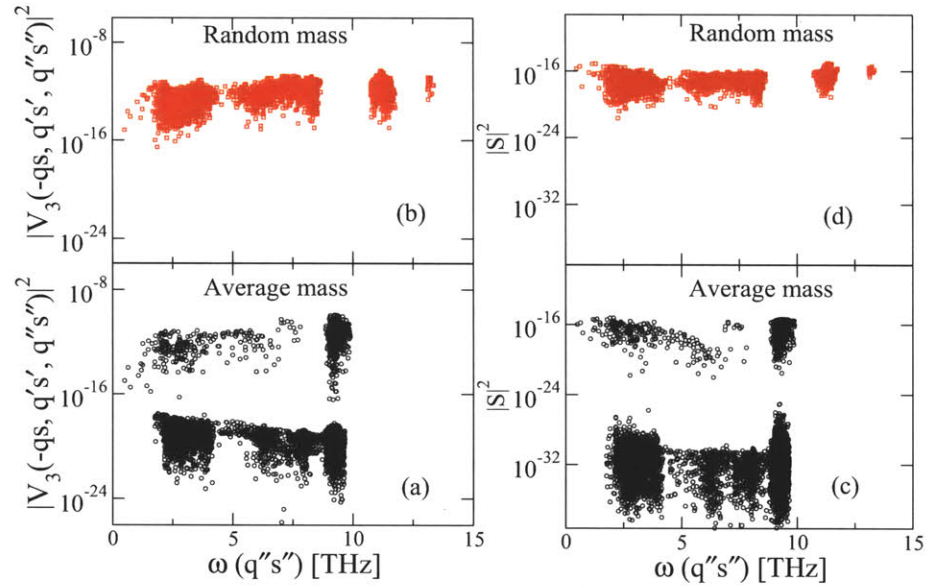
Figure 4-10: Three-phonon coupling matrix elements ($|\widetilde{V}_3|^2$) and "eigenvector overlap" ($|S|^2$) computed for $Si_{0.3}Ge_{0.7}$ on a 2x2x2 supercell using – average mass (a and c respectively) – a random distribution of masses (b and d respectively)
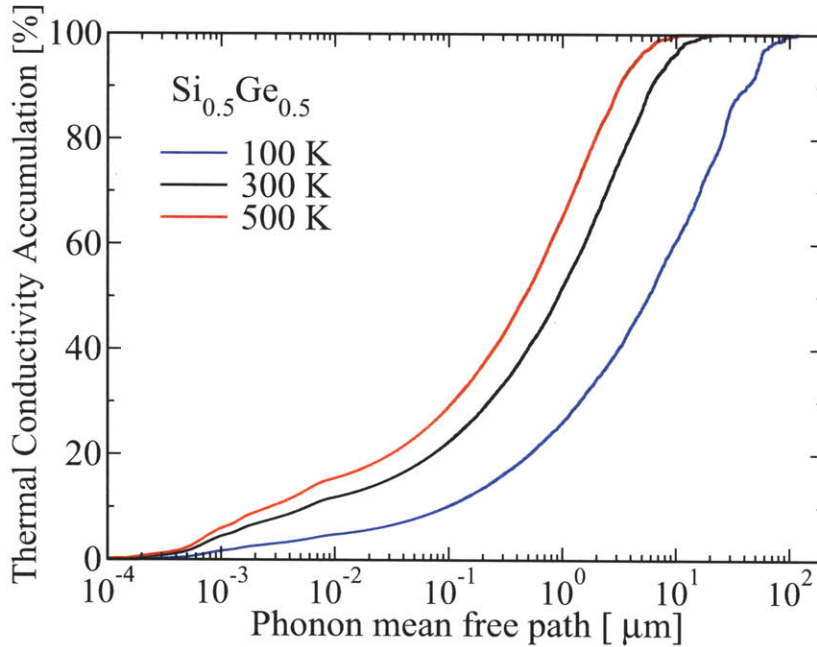
Figure 4-11: Accumulation of the thermal conductivity for $Si_{0.5}Ge_{0.5}$ as a function of the phonon mean free path

for S — due to an even distribution of vibration amplitudes over all atoms in the system — while a random distribution perturbs this even distribution, preventing such cancellation.

4.2.4 Phonon mean free path dependence

The predictive power of first-principles calculations allows to lay out design rules for low thermal conductivity materials, of central importance for applications in thermoelectrics. Through a microscopic characterization of the relative contribution of the different vibrational modes in terms of their mean free paths, practical guidelines for nanostructuring to reduce the thermal conductivity below bulk alloy limit can be obtained. For example, we show that at 300 K (Fig. 4-11) more than 50% of heat is conducted by phonons with mean free paths larger than 1 μm. Additional scattering mechanisms introduced by the presence of grain boundaries or nanoparticles distributed around this length scale can thus reduce the phonon mean free paths

thereby reducing the thermal conductivity below the bulk alloy value. The above results are in agreement with the experimental work of Rowe *et al.* [40] who showed that introduction of grain boundaries can reduce the thermal conductivity of SiGe alloys by as much as $\sim 28\%$. Similarly, from Fig. 4-6, it can be seen that addition of only about 12% Ge to Si is sufficient to lower the thermal conductivity to the minimum value achievable in this binary system, of central importance to develop low-cost thermoelectric devices.

Chapter 5

Thermal conductivity of Silicon-Germanium superlattices

Superlattices could provide another avenue to lower thermal conductivity and achieve higher figure of merit in thermoelectric devices. Venkatasubramanian *et al.* [11] measured the ZT of 10 Å/50 Å p-type Bi_2Te_3/Sb_2Te_3 superlattice to be about 2.4, a value significantly higher than the ZT of bulk materials. Devices built using this superlattice demonstrated a potential to pump heat fluxes up to 700 W cm^{-2}. Localized cooling (for refrigeration) and heating rates (heat pump) were measured to be almost 23,000 times faster than in bulk devices. This fast response was due to the heat transfer being through thin films with thickness of the order of microns rather than through millimeters associated with bulk devices.

Superlattices thus have the potential to achieve significantly higher ZT values compared to bulk materials. Extensive work has been done to understand thermal transport in superlattices; e.g. Venkatasubramanian *et al.* [41] measured the thermal conductivity of Si/Ge superlattices with periods between 30 Å and 300 Å using the 3-omega method [80]. They measured the thermal conductivity of the Si/Ge superlattice with period $L = 150$ Å to be about 2 W/mK at room temperature. This value is almost two orders of magnitude lower than the corresponding value for Si^{28}. To understand this dramatic decrease in thermal conductivity, significant theoretical work has been done to model thermal transport in superlattices.

Ren and Dow [81] explained low thermal conductivity in terms of a new type of umklapp processes, which they termed mini-umklapp. Normal processes do not by themselves offer resistance to the flow of heat, but superlattices have a larger lattice parameter and hence a smaller Brillouin zone in the direction of layering. The reciprocal lattice vector associated with this folded Brillouin zone was described to give rise to mini-umklapp processes which contribute to thermal resistance. Majumdar [82] cast the problem of heat transport by lattice vibrations in dielectric thin films as a radiative transport problem and found that in the acoustically thick limit, where the film thickness is much larger than the phonon-scattering mean free path, the phonon radiative transfer model reduces to the Fourier law. Chen [45] developed models of the effective thermal conductivity of periodic thin-film structures in the parallel direction based on the Boltzmann transport equation. Different interface conditions including specular, diffuse and partially specular and partially diffuse interfaces were considered; the study found that atomic-scale interface roughness was the major cause for the measured reduction in superlattice thermal conductivity. It was also argued that by controlling interface roughness the effective thermal conductivity of superlattices made of bulk materials of high thermal conductivities could be reduced to those of amorphous materials, while maintaining high electrical conductivities, providing avenues for high ZT materials. Subsequently Chen [83] also investigated the thermal conductivity in the cross-plane direction by solving the Boltzmann transport equation. Different scattering mechanisms, including elastic versus inelastic and diffuse versus specular were considered. The thermal conductivity in the cross plane direction was found to be related to the thermal conductivity of the individual layers and a thermal boundary resistance. The thermal boundary resistance was found to be not an intrinsic property of the boundary but depended on the layer thickness and the phonon mean free path.

All of the above attempts to explain the low thermal conductivity of superlattices focussed on increased scattering of phonons. However Hyldgaard and Mahan [46] attributed the decrease in superlattice thermal conductivity to a lower phonon group velocity due to the confinement of phonon modes. They found that the decrease in

group velocity can lead to almost an order of magnitude decrease in thermal conductivity. Subsequently Tamura *et al.* [84] also found that the component of the phonon group velocity in the growth direction of superlattice was reduced due to the flattening of the dispersion curves associated with Brillouin zone folding. In Si/Ge superlattices they found that this leads to an order of magnitude decrease in thermal conductivity, in agreement with the results of Hyldgaard and Mahan.

Simkin and Mahan [85] also discussed the conflict between the thermal conductivity behaviour of superlattices with small and large period lengths. At small period lengths, the thermal conductivity increases with a decrease in period length. However at large period lengths, the behaviour is the opposite, the thermal conductivity decreases with a decrease in period length. They resolved this by using the wave picture at small period lengths and the particle picture at large period lengths. In the wave picture, the decrease in thermal conductivity with increasing period length is due to the interference effects which cause a decrease in group velocity. In the particle picture however, it was proposed that the these interference effects disappear due to the phonon mean free path being smaller than the period length.

In this Chapter, we investigate the thermal conductivity in superlattices from first-principles. The phonon modes of the superlattice are used to derive the phonon frequencies, group velocities and populations that enter into the computation of thermal conductivity, and phonon relaxation times are computed based on the three-phonon scattering processes. We still solve the phonon Boltzmann transport equation in the single-mode relaxation time approximation. We compute the thermal conductivity of [001] superlattices with period lengths ranging from 2 atomic layers to 28 atomic layers. We find that for superlattices with period length between 4 atomic layers and 28 atomic layers, the computed thermal conductivity drops with increase in period length and is lower than that of Ge^{70}. This is due to the decrease in group velocity as a result of zone folding. However we find that for the superlattice with period length of only 2 atomic layers the computed thermal can exceed that of Si^{28}. This large increase in thermal conductivity as the period length is decreased from 4 atomic layers to 2 atomic layers cannot be explained based solely on the increase in group velocity.

We find that the large gap in phonon frequencies of optical and acoustic modes at the zone edge in the 2 atomic layer superlattice strongly affects the three-phonon scattering processes. The gap dramatically reduces the scattering of acoustic modes by optical modes and leads to a large increase in the relaxation times of acoustic modes. This in turn leads to large increase in the thermal conductivity at this small period length.

To describe the superlattices with a particular growth direction and period, we use the notation $SiGe[001]_{i+f}$, where Si and Ge represent the materials that constitute the alternate layers, [001] represents the growth direction, and in the subscript $i + f$, i represents the number of atomic layers of Si and f represents the number of atomic layers of Ge in one period of the superlattice. The period of the superlattice is thus $i + f$ atomic layers.

5.1 Harmonic and anharmonic force constants in superlattices

Our approach to compute the thermal conductivity of superlattices is similar to the one used to compute the thermal conductivity of isotopically pure Si^{28} and Ge^{70}. There are two main differences, however, which are outlined below:

1. To compute the thermal conductivity of Si^{28} and Ge^{70}, the second-order and third-order force constants corresponding to Si^{28} and Ge^{70} were used. The force constants for the superlattice are however derived using the virtual crystal approximation [44] where the atomic potential at each site is an average of the Si and Ge potentials. The second-order and the third-order force constants are again computed on a 10x10x10 and a 3x3x3 supercell (of the 2-atom fcc unit cell), respectively.

2. The unit cell of the superlattice varies with the period length and is different from the 2-atom fcc unit cell. Therefore the second-order and third-order force constants obtained above cannot be used directly but must be folded appropriately.

Once the second-order and third-order force constants are obtained for a super-
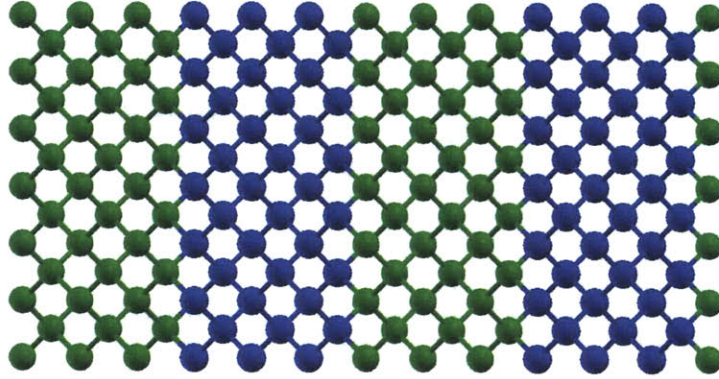
Figure 5-1: A SiGe[001]$_{6+6}$ superlattice with a period of 12 atomic layers.

lattice with a particular period length, the thermal conductivity is computed using Eq. 3.71. The second-order force constants are used to compute the phonon frequencies, group velocities and populations. The third-order force constants are used to calculate the phonon relaxation times based on anharmonic three-phonon scattering processes.

The computed thermal conductivity of superlattices with periods larger than 2 atomic layers is presented in Fig. 5-2 for T=300 K.

5.2   Thermal conductivity variation with superlattice period

Fig. 5-2 shows that with increase in the superlattice period the thermal conductivity drops sharply, and then for larger period lengths the behaviour plateaus out. The minimum computed cross-plane thermal conductivity is about 13 W/mK. This value is higher than the reported values. Lee *et al.* [41] measured the thermal conductivity of Si/Ge superlattices with periods ranging between 30 Å to 275 Å to lie between 1 and 5 W/mK. Thus calculated values are higher than experimentally measured values
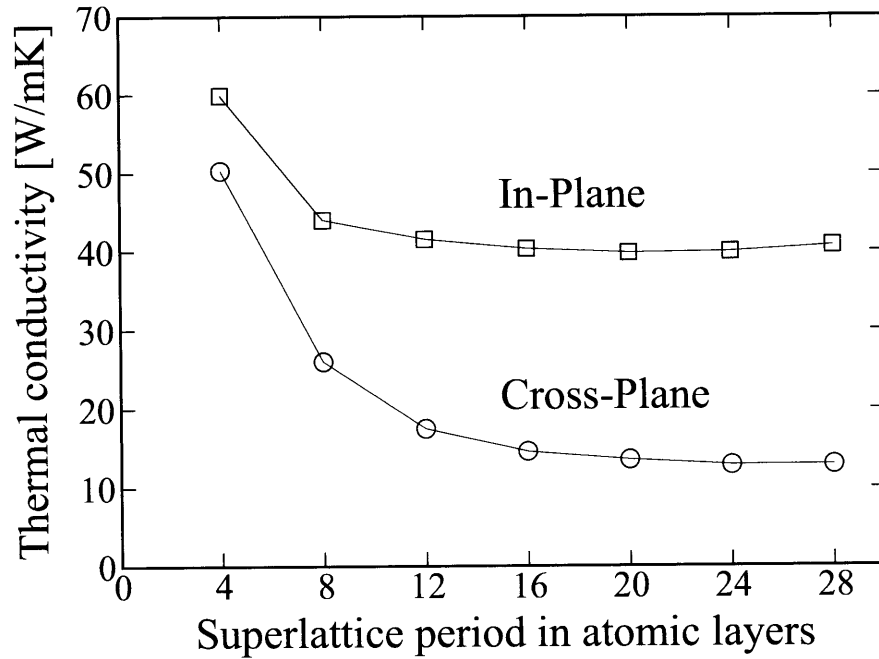
Figure 5-2: Variation of the in-plane and cross-plane thermal conductivity of Si/Ge superlattices (computed in the single mode-relaxation time approximation) with the superlattice period at 300 K.
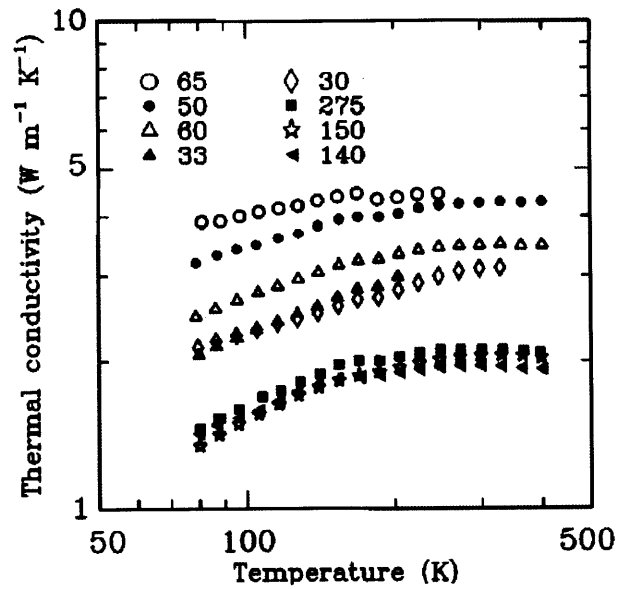
Figure 5-3: Experimentally measured values of the Si/Ge superlattice thermal conductivity from Ref. [41]. Each symbol is labelled by the superlattice period L measured in Å.
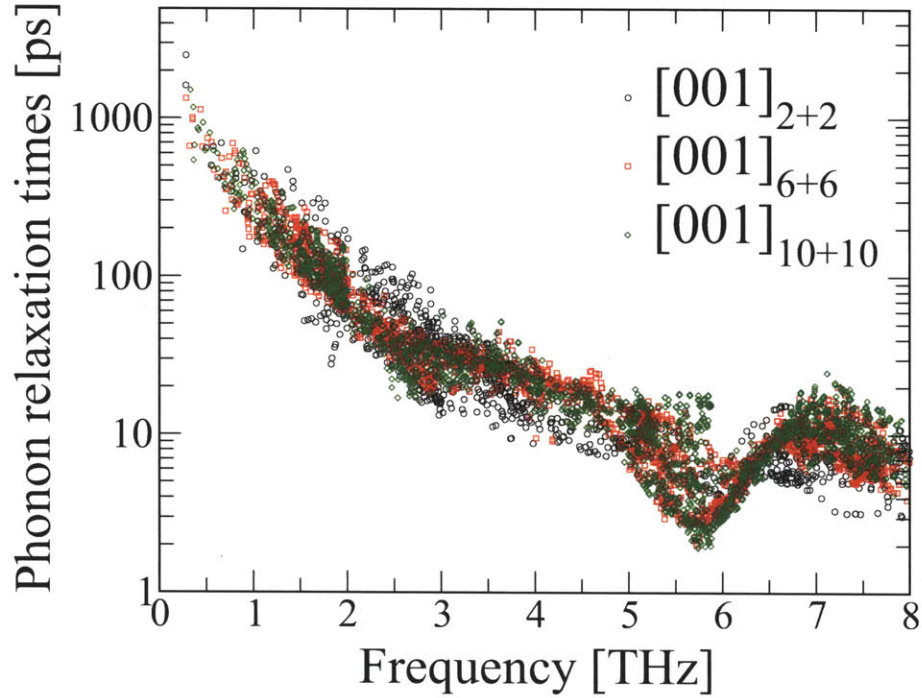
Figure 5-4: Anharmonic phonon relaxation times in Si/Ge superlattices of different periods at 300 K.

by almost an order of magnitude. The cause of this discrepancy will be discussed later and we first discuss the cause of the decrease in computed thermal conductivity. To do this, the phonon group velocities and phonon relaxation times are compared as the period is increased; it can be seen in Fig. 5-4 that the phonon relaxation times do not change. However, it is found that with increase in period length, the phonon group velocities decrease rapidly and we discuss this next.

5.2.1 Group velocity reduction in superlattices

In Figs. 5-5(a) and (b) the mean squared phonon group velocities weighted with the density of states (defined by Eq. 4.2) are compared for different period lengths, both for the cross-plane and in-plane directions. It can be seen that both the cross-plane and in-plane group velocities decrease as the superlattice period is increased. At long period lengths however the group velocities do not decrease any further leading to

the thermal conductivity also becoming constant. Interestingly, it can be seen that at large period lengths the cross-plane group velocities above the highest frequency in Ge^{70} drop to zero. This is simply because higher frequency modes localize within the silicon layer and therefore have zero group velocities. At small period lengths however phonon modes are able to tunnel through, leading to finite group velocities even at high frequencies.

Such a drop in group velocity was also observed by Tamura [84] and Mahan [46], and the cause discussed by Tamura [86], that showed that the presence of alternate layers of materials with different atomic masses leads to Bragg reflection at the Brillouin zone edge and center. This Bragg reflection leads to the creation of a gap in the phonon energies, in turn leading to a flattening of the phonon dispersion. As the period of the superlattice is increased, the Brillouin zone gets folded and the Bragg reflection leads to the creation of additional frequency gaps, in turn leading to further flattening of the phonon dispersion. For this reason, the phonon group velocities decrease as the period length is increased.

Chen [87] also investigated the effect of formation of the frequency gaps on the phonon group velocity and a reduction in the thermal conductivity. At small superlattice periods, the high-frequency phonon modes are able to tunnel through the germanium layers, leading to finite group velocities. However, as the superlattice period width is increased, these modes become progressively localized within the silicon layer, and the group velocity decreases further, leading to the observed drop in computed thermal conductivity. Above a certain width of the germanium layers, all the high frequency phonon modes become localized within the silicon layer, and only the lower frequency phonon modes are able to propagate through. Beyond this period width, there is no further change in group velocity and the thermal conductivity value reaches a constant.

In the very long period length limit, both the in-plane and cross-plane thermal conductivity can be computed from bulk values. Realizing that in the in-plane direction, the thermal resistance of the two layers is in parallel, the thermal conductivity in the long period length limit is given by

108
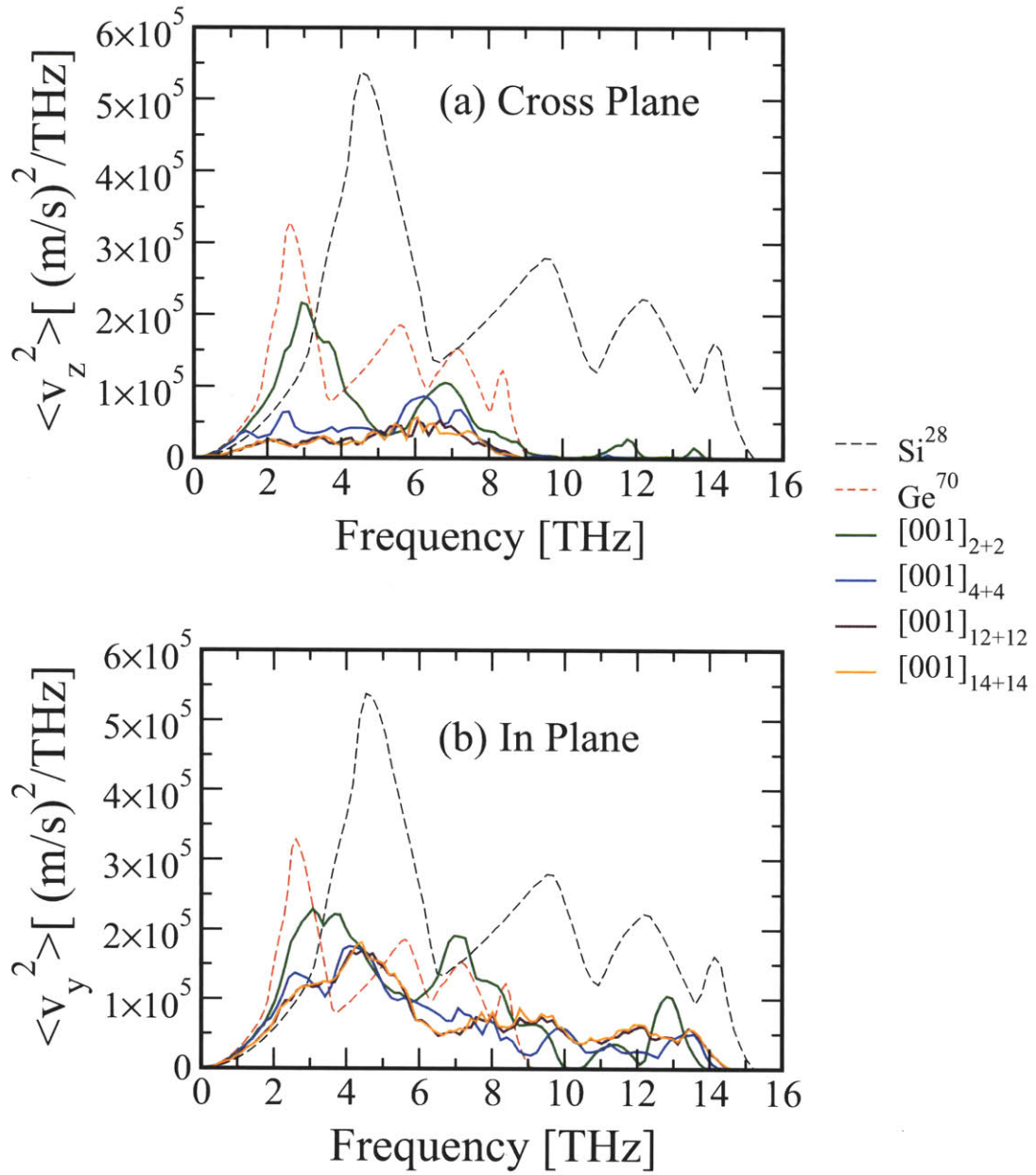
Figure 5-5: Mean squared phonon group velocities (defined by Eq. 4.2) as a function of frequency in Si^{28}, Ge^{70} and Si/Ge superlattices along (a) Cross-plane direction and (b) In-plane direction.

$$k_{in-plane} = \frac{k_{Si} + k_{Ge}}{2}.$$ (5.1)

Using the computed values of the thermal conductivity of silicon (130 W/mK) and germanium (59 W/mK) at 300 K from Chapter 3, the long period limit of the in-plane thermal conductivity of Si/Ge superlattice is obtained to be 94.5 W/mK. For the cross-plane direction, the thermal resistances are in series and therefore the long period length limit is given by

$$k_{cross-plane} = \frac{k_{Si} \times k_{Ge}}{k_{Si} + k_{Ge}}.$$ (5.2)

The above value is computed to be 40.6 W/mK. Thus the long period limits of both the in-plane (94.5 W/mK) and the cross-plane (40.6 W/mK) thermal conductivity are higher than the constant values achieved in our calculations, about 40 W/mK and 13 W/mK for in the in-plane and cross-plane directions respectively. Thus in the very long period limit, our computed thermal conductivity should increase and asymptotically reach the limits presented above. However, it has been argued [88] that our approach based on the use of phonon modes of the superlattice would not show such a behaviour.

To resolve this Simkin and Mahan [85] proposed that in the small period range, for layers thinner than the mean free path, the wave theory applies. Wave interference leads to band folding which in turn leads to a reduction of group velocities and the observed reduction in computed thermal conductivity (Fig. 5-2). However, they argued that when the layer thickness (L) exceeds the mean free path (l), the particle model should become applicable and the interference effects should diminish, leading to an increase in thermal conductivity. They achieved this in a phenomenological way by adding a complex part (i/l) to the wave vector q and then recomputing the properties of the superlattice. Later Yang and Chen [88] further modified this model by also including the diffuse interface scattering and found that this resulted in good agreement with experimentally observed thermal conductivity reduction along both in-plane and cross-plane directions of superlattice.

5.2.2   Constant relaxation time approximation

An approximation that is typically used in the analysis of thermal conductivity of superlattices is the constant relaxation time approximation. In this approximation, it is assumed that the phonon relaxation times of all phonon modes are constant and the thermal conductivity is computed using lattice dynamics, allowing phonon frequencies, populations and group velocities to vary with the phonon modes as well as the superlattice period. Ren *et al.* [89] used the constant relaxation time approximation along with lattice dynamical calculations and found the thermal conductivity to decrease with increasing period length and then reach a constant value beyond a period length of 20 atomic layers. This result is in excellent agreement with our thermal conductivity values computed from first principles. However our explicit calculations of phonon relaxation times show that they are not constant and vary strongly with the frequency of the phonon mode (Fig. 5-4). Thus constant relaxation time approximation is not strictly valid and leads to an error in the estimate of absolute thermal conductivity. However Fig. 5-4 also shows that the relaxation times do not vary much with the superlattice period.

5.2.3   Cause of discrepancy between predicted and measured thermal conductivity

We now discuss the difference between predicted and measured values of thermal conductivity at 300 K. As indicated before, in order to estimate the harmonic and anharmonic force constants in superlattice of any period, we used the virtual crystal approximation. However in our work, we ignored the disorder at the interfaces and treated them as perfectly planar.

The disorder at the interfaces has been reported to have a profound effect on the phonon scattering. Disorder at the interface leads to strong diffuse scattering of phonons [45]. Extensive work was done by Chen [45, 83] to understand the effect of interface roughness on both in-plane and cross-plane thermal conductivity. The study
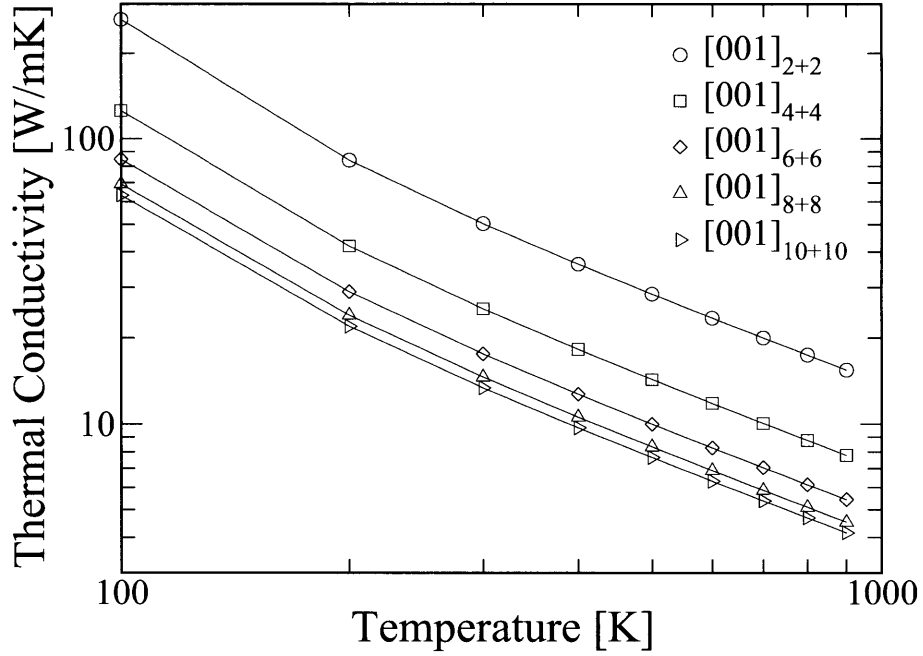
Figure 5-6: Temperature dependence of the computed superlattice thermal conductivity for superlattices of different period lengths.

found that interface roughness was the main cause of thermal conductivity reduction in superlattices, and that by enhancing the roughness, the thermal conductivity could be reduced to that of amorphous materials.

5.3 Temperature dependence of superlattice thermal conductivity

Fig. 5-6 shows the temperature dependence of the computed thermal conductivity. We find a dependence of $\sim 1/T$, as can be expected for thermal transport due to anharmonic three-phonon scattering processes. However the temperature dependence of the measured thermal conductivity is opposite of what is predicted (Fig. 5-3). The measured thermal conductivity increases with an increase in temperature at low temperatures and becomes nearly constant at higher temperatures (Fig. 5-3). This implies that while at 300 K the computed thermal conductivity disagreed with

112
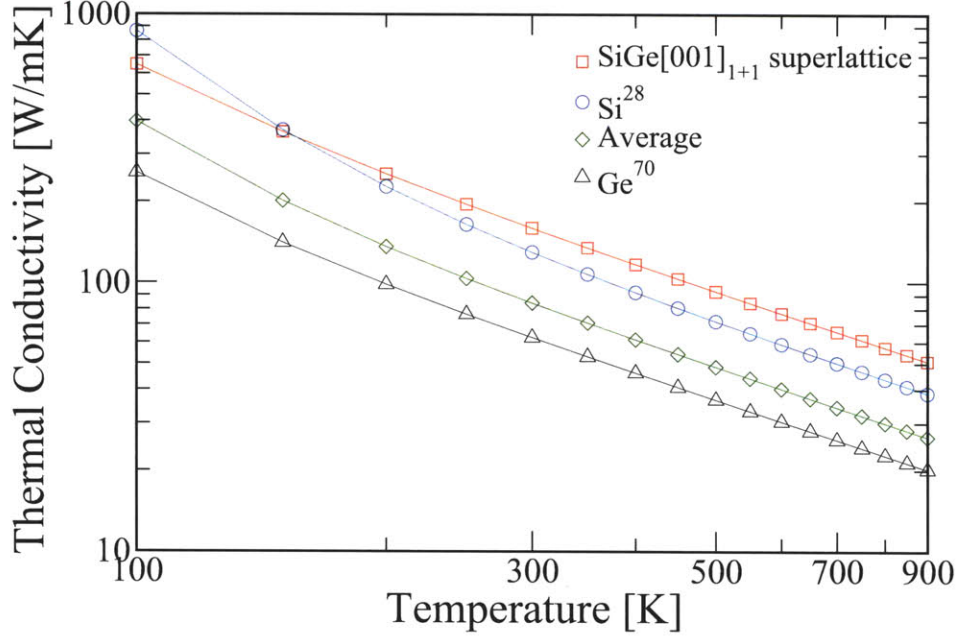
Figure 5-7: Thermal conductivity of SiGe[001]$_{1+1}$ superlattice, Si^{28}, Ge^{70} and the average material computed in the single-mode relaxation time approximation.

experiments by an order of magnitude, the disagreement at lower temperatures is much higher.

5.4   High thermal conductivity

We find that as the superlattice period is reduced from 4 atomic layers to 2 atomic layers the computed thermal conductivity increases dramatically. Fig. 5-2 shows that the average of the cross-plane and in-plane thermal conductivity in SiGe[001]$_{2+2}$ superlattice is about 55 W/mK at 300 K. The thermal conductivity of the SiGe[001]$_{1+1}$ superlattice, however, is computed to be about 160 W/mK (see Fig. 5-7) at the same temperature. Reducing the superlattice period from 4 to 2 atomic layers thus results in an increase in thermal conductivity by almost a factor of 3. More intriguingly, the thermal conductivity of the SiGe[001]$_{1+1}$ superlattice is found to exceed even that of isotopically pure silicon (Si^{28}) by about 20% at 300 K. This result is unexpected be-

cause the presence of heavy Ge^{70} atom in the silicon-germanium superlattice leads to lower phonon frequencies and lower phonon group velocities than in Si^{28} and should therefore result in lower thermal conductivity. However the opposite is found to be the case. Our approach provides an understanding of the cause of this high thermal conductivity.

Some increase in thermal conductivity is expected as the superlattice period is reduced. At small superlattice periods, phonon modes are able to tunnel through the small length scale variations in mass and the phonon group velocity increases resulting in an increase in thermal conductivity. However this by itself cannot explain an increase in thermal conductivity by more than a factor of 3 when the superlattice period is reduced from 4 atomic layers to 2 atomic layers. To show this more explicitly, we compare the thermal conductivity of $SiGe[001]_{1+1}$ superlattice with a system where the mass of each atom is an average of the masses of Si and Ge. We will use the term "average material" to describe this system henceforth. We first compare the phonon group velocities in the two materials. To make this comparison easier, we use the mean squared group velocities weighted by the density of states, as defined by Eq. 4.2. The comparison is presented in Fig. 5-8(a). At frequencies below 5 THz where most of the contribution to thermal conductivity occurs (see Figs. 3-10(a) and (b)) the phonon group velocities in the two materials (average and superlattice) are equal (Fig. 5-8(a)). This can be expected as at low frequencies, the phonon modes in the $SiGe[001]_{1+1}$ superlattice see the average mass and therefore have similar frequencies and group velocities as the average material. Based on the group velocity arguments alone, the thermal conductivity of the $SiGe[001]_{1+1}$ superlattice should be similar to that of the average material, about 84 W/mK, at 300 K (see Fig.5-7). However the superlattice thermal conductivity (160 W/mK) exceeds that of the average material by almost a factor of 2. Furthermore, due to the presence of heavier Ge atom, the group velocities in the superlattice are lower than in isotopically pure Si (see Fig. 5-8), implying that the thermal conductivity of the superlattice should be lower than Si^{28}. Again, the results are contrary to such an expectation. Group velocity increase cannot therefore completely explain the dramatic increase in thermal conductivity by a factor of 3 as
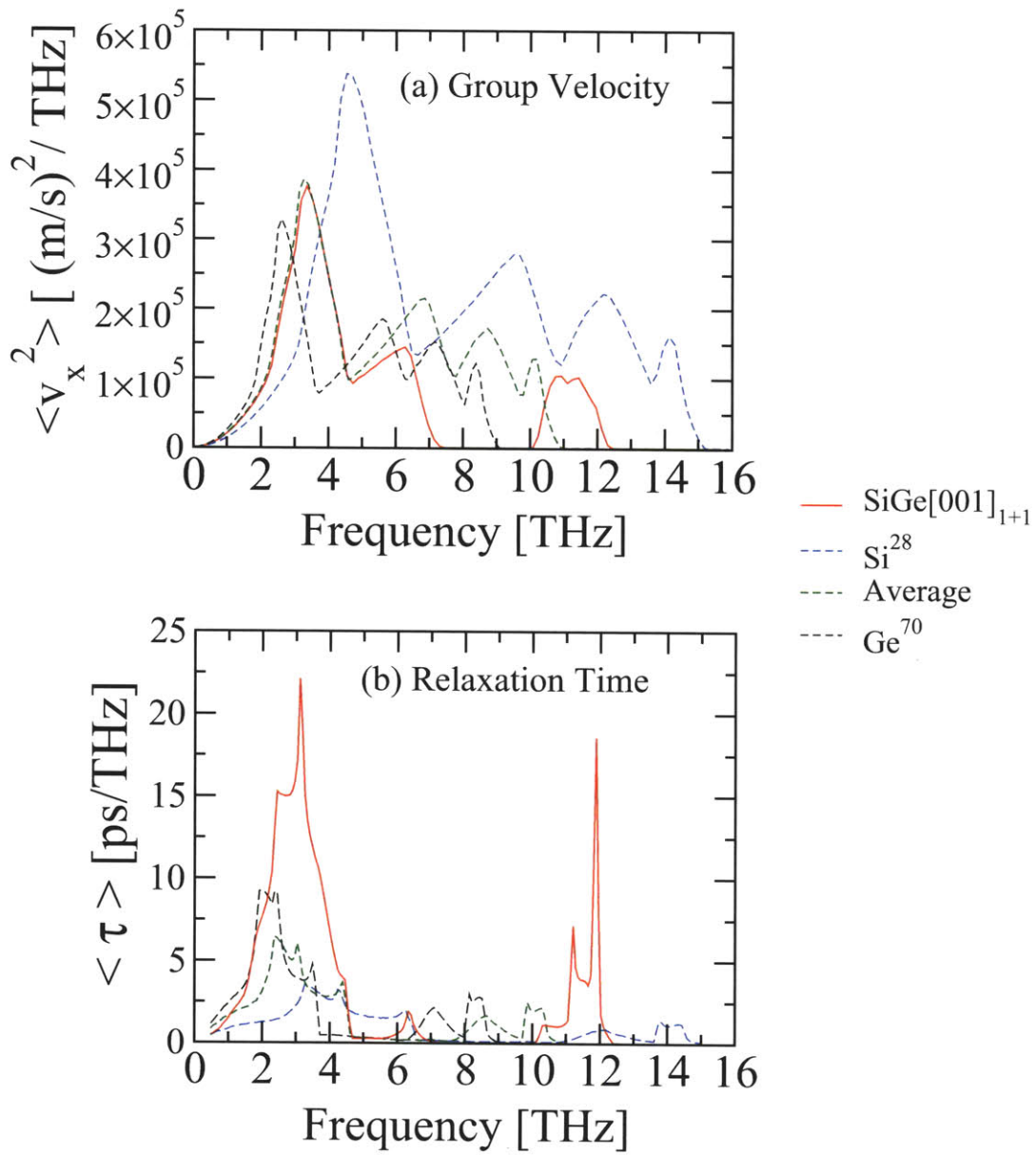
114

Figure 5-8: Comparison of (a) Mean squared group velocities (defined by Eq. 4.2) and (b) Mean relaxation times – in Si^{28}, Ge^{70}, average material and $SiGe[001]_{1+1}$ superlattice.

the superlattice period is decreased from 4 to 2 atomic layers.

We find that this enhancement in thermal conductivity occurs due to a large reduction in the scattering rates of acoustic phonons in the $SiGe[001]_{1+1}$ superlattice compared with the $SiGe[001]_{2+2}$ superlattice, Si^{28}, Ge^{70} and the "average material". This reduction in the scattering rates of acoustic phonons leads to an increase in their relaxation times. We discuss this in more detail in the following section.

5.4.1 Higher phonon relaxation times in the $SiGe[001]_{1+1}$ superlattice

Fig. 5-9 shows that the relaxation times of the individual phonon modes in $SiGe[001]_{1+1}$ superlattice are significantly higher than those in superlattices of larger periods as well as in isotopically pure silicon (Si^{28}). Similarly in Fig. 5-8(b) we compare $SiGe[001]_{1+1}$ superlattice with Si^{28}, Ge^{70} and the "average material" in terms of mean relaxation times weighted with the density of states. These are defined by replacing the squared group velocities with relaxation times in Eq. 4.2. At low frequencies these mean relaxation times in the $SiGe[001]_{1+1}$ superlattice are higher by 3 to 4 times compared to Si^{28}, Ge^{70} and the average material. In Figs. 5-13 and 5-14 we compare the phonon relaxation times of transverse and longitudinal acoustic modes along the directions of high symmetry. Fig. 5-13 shows that the relaxation times of the transverse acoustic modes in the $SiGe[001]_{1+1}$ superlattice are more than 5 times higher than in isotopically pure silicon (Si^{28}) and the "average material" at the Brillouin zone edge.

Thus while the long wavelength acoustic phonons in the $SiGe[001]_{1+1}$ superlattice have the same frequencies and group velocities as the average material (see Figs. 5-13 and 5-14), they scatter much less in the superlattice as compared to the average material. To understand how such an effect arises it is worthwhile to compare the phonon dispersions of the two materials along Γ-X-Γ in Figs. 5-10(a) and (b). In the case of the "average material" a dominant scattering mechanism for the transverse acoustic modes involves absorbing longitudinal acoustic modes and converting into optical modes. This is illustrated in Fig. 5-10(a). Such a scattering process has to

116
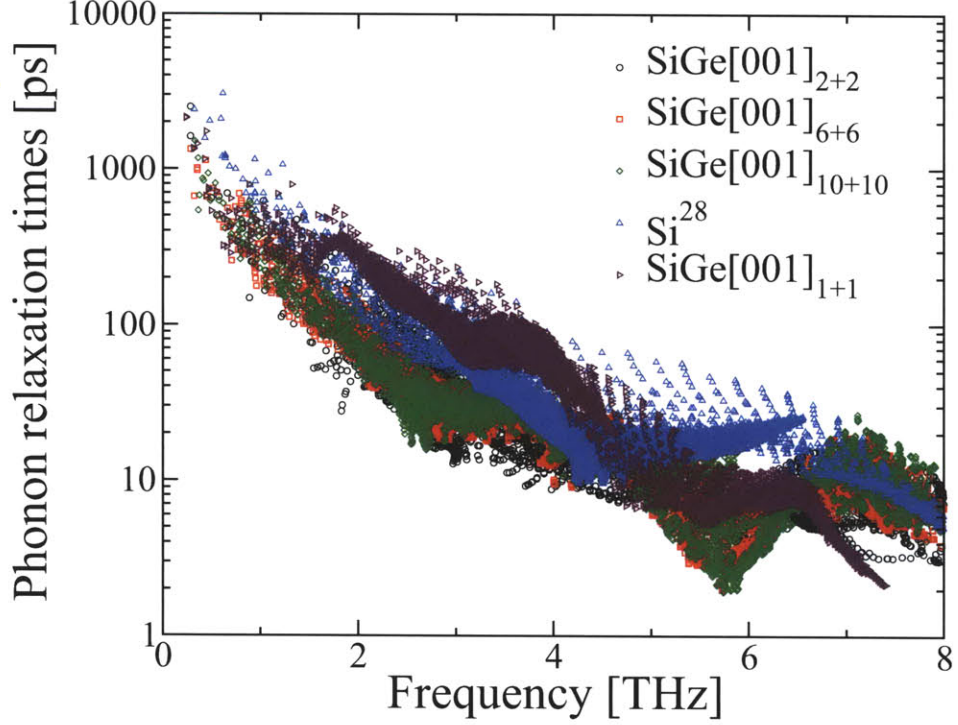
Figure 5-9: Anharmonic phonon relaxation times in SiGe$[001]_{1+1}$ superlattice at 300 K compared with Si^{28} and superlattices of larger periods

satisfy both momentum conservation: $\boldsymbol{q} + \boldsymbol{q}' = \boldsymbol{q}''$ and energy conservation: $\omega(TA) + \omega'(LA) = \omega''(O)$. We show one such channel for the scattering of transverse acoustic mode in the "average material" in Fig. 5-10(a). The channel satisfies both momentum and energy conservation as indicated below:

$$\boldsymbol{q}[(0,0,0.4)\frac{2\pi}{a}] + \boldsymbol{q}'[(0,0,0.71)\frac{2\pi}{a}] = \boldsymbol{q}''[(0,0,1.11)\frac{2\pi}{a}]$$

$$\omega(\boldsymbol{q}, TA)[2.4 \text{ THz}] + \omega'(\boldsymbol{q}', LA)[6.88 \text{ THz}] = \omega''(\boldsymbol{q}'', LO)[9.28 \text{ THz}].$$

(5.3)

However, in the SiGe$[001]_{1+1}$ superlattice, a large gap exists between the frequencies of optical and acoustic phonons (Fig. 5-10(b)). This frequency gap prohibits such a scattering channel. Due to this large gap, the frequency of the optical mode is typically larger than the sum of the frequencies of the relevant acoustic modes and the above scattering channel is no longer feasible as demonstrated below:

117

$$\boldsymbol{q}[(0,0,0.4)\frac{2\pi}{a}] + \boldsymbol{q}'[(0,0,0.71)\frac{2\pi}{a}] = \boldsymbol{q}''[(0,0,1.11)\frac{2\pi}{a}]$$

$$\omega(\boldsymbol{q},TA)[2.4 \text{ THz}] + \omega'(\boldsymbol{q}',LA)[6.45 \text{ THz}] = \omega''[8.85 \text{ THz}] < \omega''(\boldsymbol{q}'', \text{ Optical})$$

(5.4)

This is also shown in Fig. 5-10(b). This absence of scattering by optical phonon modes results in a decrease in the scattering rates of the TA modes and an increase in their relaxation times.

To show the importance of optical phonons in scattering transverse acoustic phonons in the "average material" we split the total scattering rate of the TA modes into three parts – first part involves absorbing another acoustic mode to yield an acoustic mode: TA + A = A, second part involves absorbing an acoustic mode to yield an optical mode: TA + A = O, and the third part involves absorbing an optical mode to yield another optical mode: TA + O = O. Other scattering processes contribute negligibly. Fig. 5-11 shows that the three scattering rates are almost equal in magnitude and therefore scattering by optical phonon contributes almost two thirds to the total scattering rate of the transverse acoustic mode in the "average material" along Γ-L at 300 K. However, in the SiGe[001]$_{1+1}$ superlattice due to the large gap in the frequencies of optical and acoustic phonons, Fig. 5-11 shows that the scattering by optical phonons is completely absent, resulting in the scattering rates of the transverse acoustic modes in the superlattice being about one-third of the scattering rates in the "average material". Similar comparison for the longitudinal modes is presented in Fig. 5-12.

To show the effect of this on the heat conduction ability of the acoustic modes, we compare all the ingredients that go into the computation of the thermal conductivity (Fig. 5-13). We make this comparison for the transverse acoustic mode in four different materials: Si^{28}, Ge^{70}, "average" and SiGe[001]$_{1+1}$ superlattice. While the phonon frequencies, group velocities and the populations of the transverse acoustic mode in the superlattice are equal to those in the average material, the phonon relaxation times are significantly larger. This leads to the transverse acoustic modes conducting
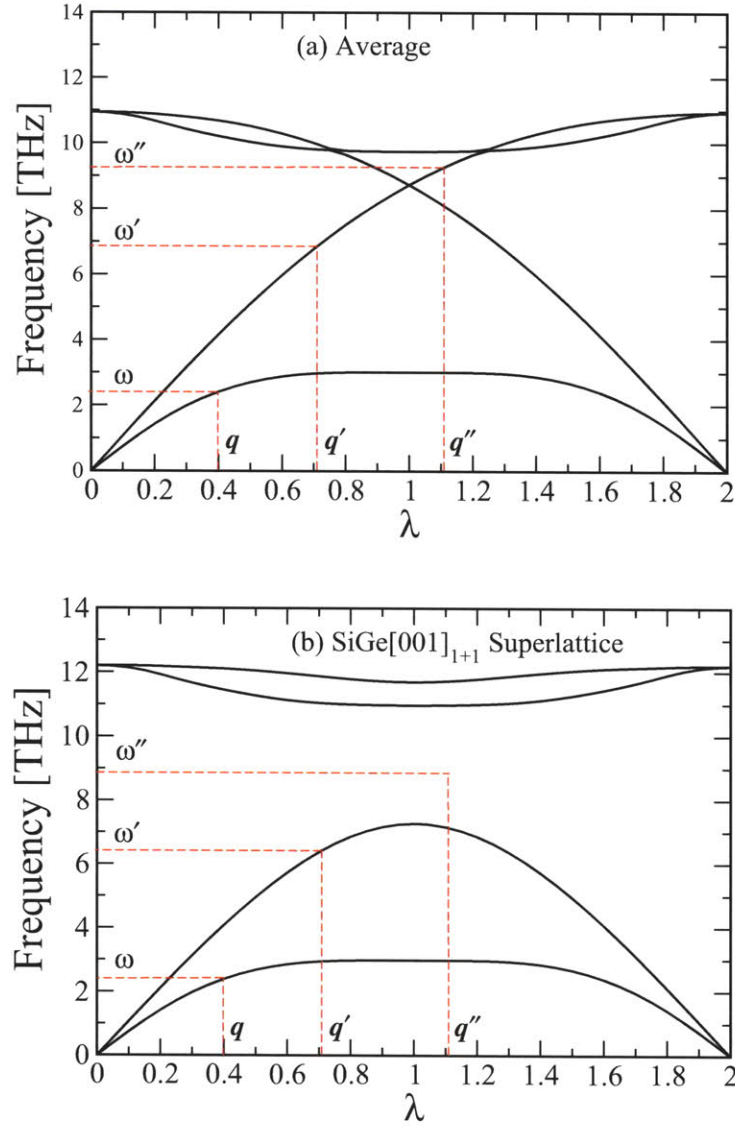
Figure 5-10: Effect of gap between frequencies of optical and acoustic phonon modes on scattering of acoustic modes by optical modes (a) In the average material where the frequency gap does not exist, a transverse acoustic mode can absorb a longitudinal acoustic mode and yield an optical phonon mode. This process satisfies both the energy and momentum conservation i.e. $\boldsymbol{q} + \boldsymbol{q'} = \boldsymbol{q''}$ $\omega(\boldsymbol{q}, TA) + \omega'(\boldsymbol{q'}, LA) = \omega''(\boldsymbol{q''}, LO)$ (b) In the case of SiGE[001]$_{1+1}$ superlattice, the large gap between frequencies of optical and acoustic modes prohibits such a scattering channel to be present and we find that for the same three phonons $\boldsymbol{q}, \boldsymbol{q'}$ and $\boldsymbol{q''}$ the energy conservation is not satisfied in the superlattice, $\omega(\boldsymbol{q}, TA) + \omega'(\boldsymbol{q'}, LA) = \omega'' < \omega''(\boldsymbol{q''}, Optical)$.
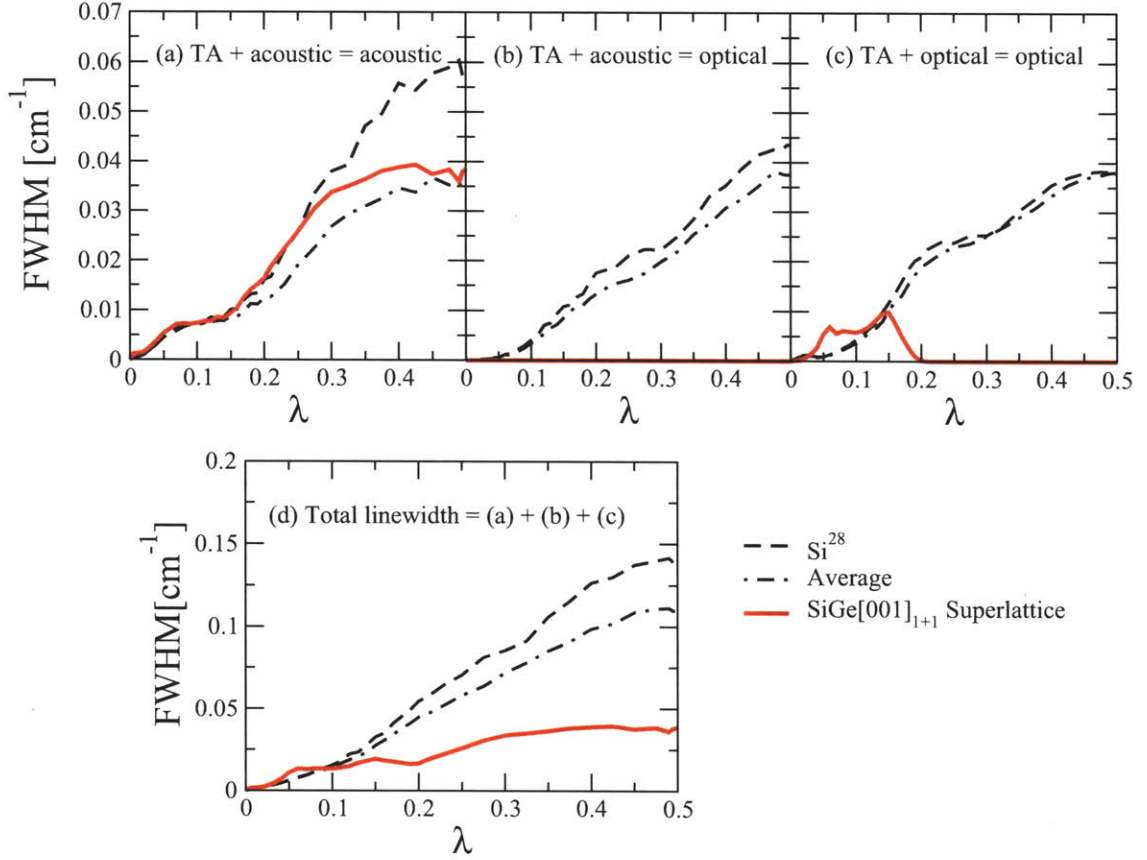
Figure 5-11: Comparison of the linewidth of the transverse acoustic mode at 300 K along the Γ-L direction $(\lambda,\lambda,\lambda)$ in three materials: Si^{28} (dashed line), average material (dashed-dotted line) and $SiGe[001]_{1+1}$ superlattice (solid line). Contribution to total linewidth of the transverse acoustic mode due to (a) absorption of an acoustic to yield an acoustic mode, (b) absorption of an acoustic mode to yield an optical mode and (c) absorption of an optical mode to yield an optical mode. (d) Total linewidth of the transverse acoustic mode, which is the sum of (a),(b) and (c). In the case of $SiGe[001]_{1+1}$ superlattice, scattering by optical modes, i.e. parts (b) and (c), is almost completely absent. This results in the total linewidth of the transverse acoustic mode being much lower in the $SiGe[001]_{1+1}$ superlattice leading to higher relaxation times.
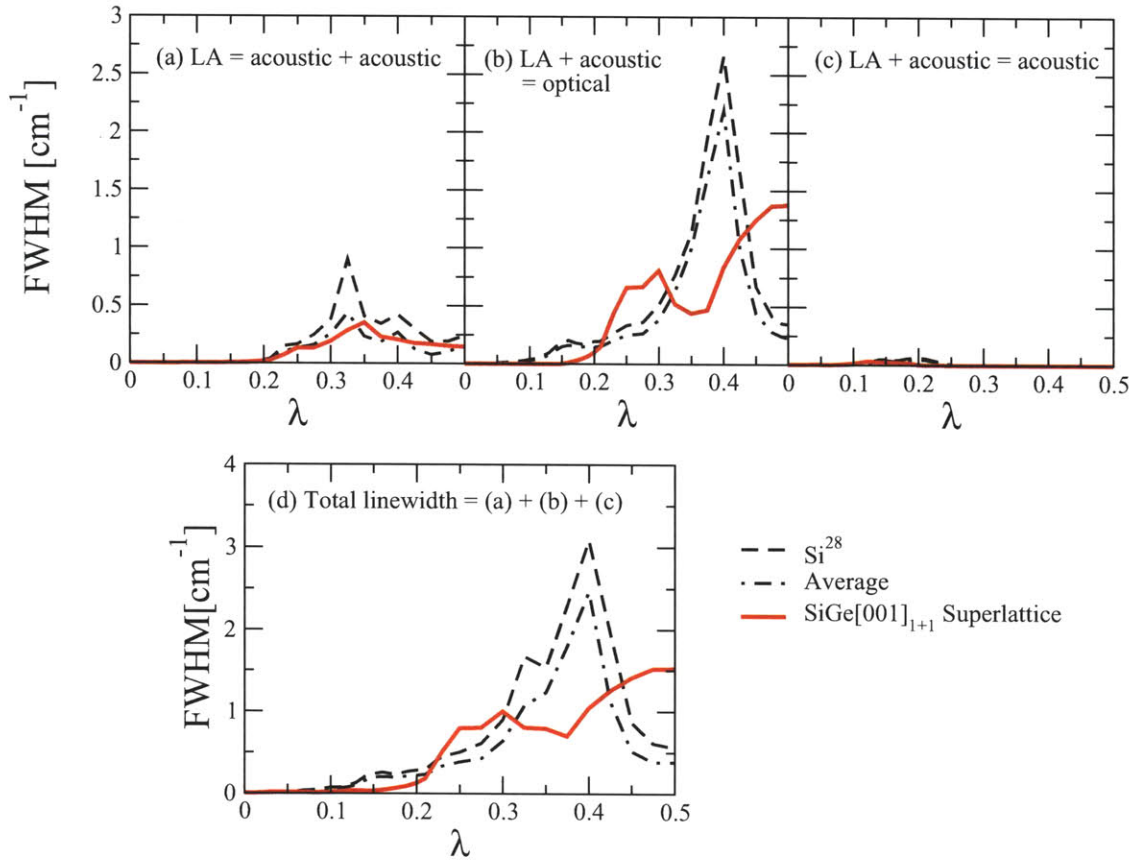
Figure 5-12: Comparison of the linewidth of the longitudinal acoustic mode at 300 K along the Γ-L direction $(\lambda, \lambda, \lambda)$ in three materials: Si^{28} (dashed line), average material (dashed-dotted line) and $SiGe[001]_{1+1}$ superlattice (solid line). Contribution to total linewidth of the longitudinal acoustic mode due to (a) decay into two acoustic modes (b) absorption of an acoustic mode to yield an optical mode (c) absorption of an acoustic mode to yield an acoustic mode. (d) Total linewidth of the longitudinal acoustic mode, which is the sum of (a),(b) and (c).

more heat in the SiGe[001]$_{1+1}$ superlattice than in the other materials. This increase in the heat conduction ability of acoustic modes due to an increase in their relaxation times leads to the large increase in the thermal conductivity of SiGe[001]$_{1+1}$ superlattice.

5.4.2 Engineering high thermal conductivity through varying mass-mismatch

The above result could have useful implications for the design of high thermal conductivity materials. To understand how the mass-mismatch between the materials constituting the alternate layers affects thermal conductivity, we consider a [001]$_{1+1}$ superlattice where we fix the mass of one atom in the unit cell to be that of Si, and vary the mass of the second atom (the unit cell of the [001]$_{1+1}$ superlattice is the 2 atom fcc unit cell). The variation of thermal conductivity at different temperatures is presented in Fig. 5-15. As the mass mismatch is increased beyond that of the Si/Ge superlattice, it is found that thermal conductivity increases even further. This is due to a further reduction in the scattering rates and increase in the relaxation times of acoustic phonon modes (Figs. 5-16 and 5-17]).
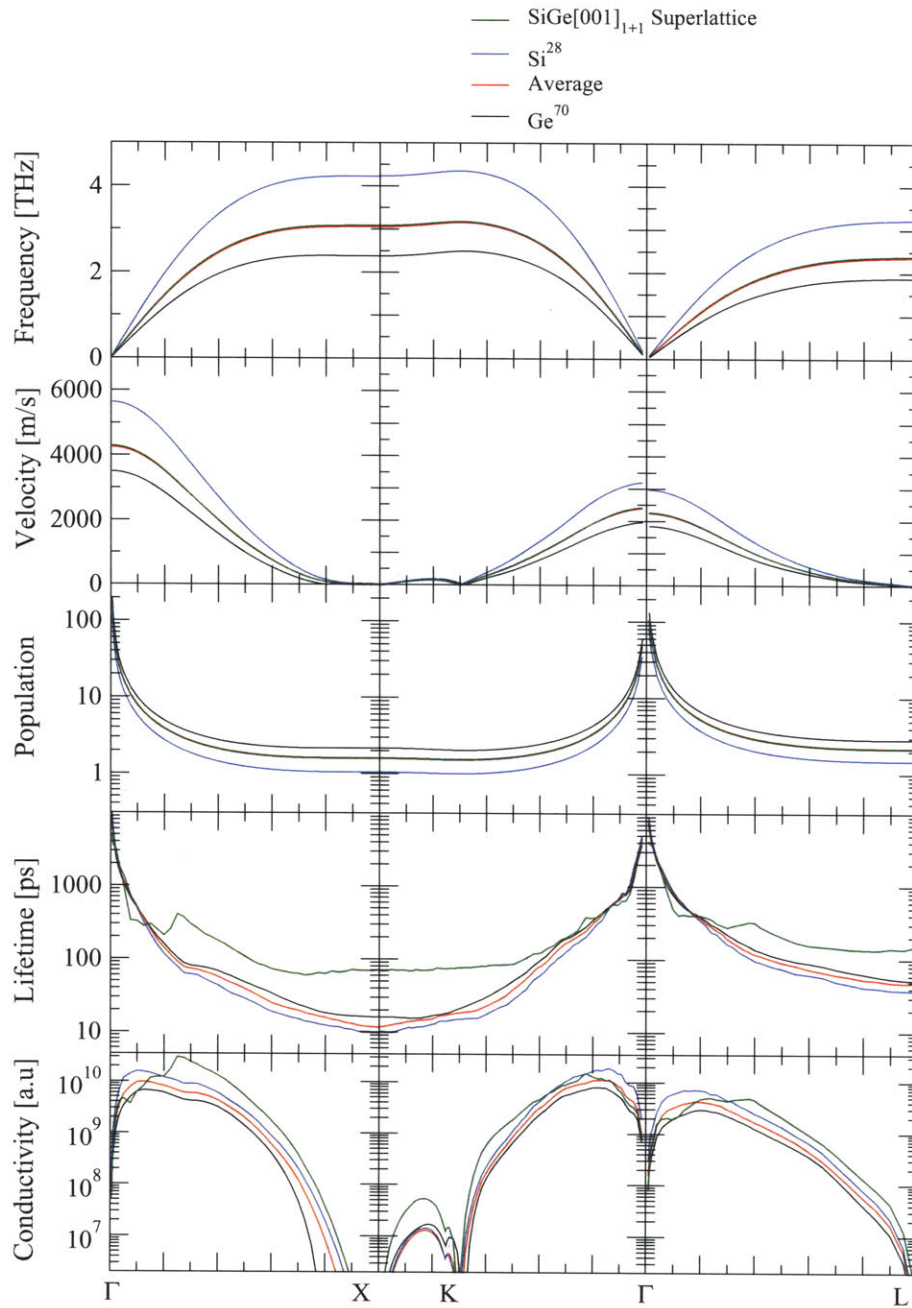
Figure 5-13: Comparison of the transverse acoustic modes between Si^{28}, Ge^{70}, average and $SiGe[001]_{1+1}$ superlattice, in terms of their phonon frequencies, group velocities, populations, relaxation times and contributions to thermal conductivity.
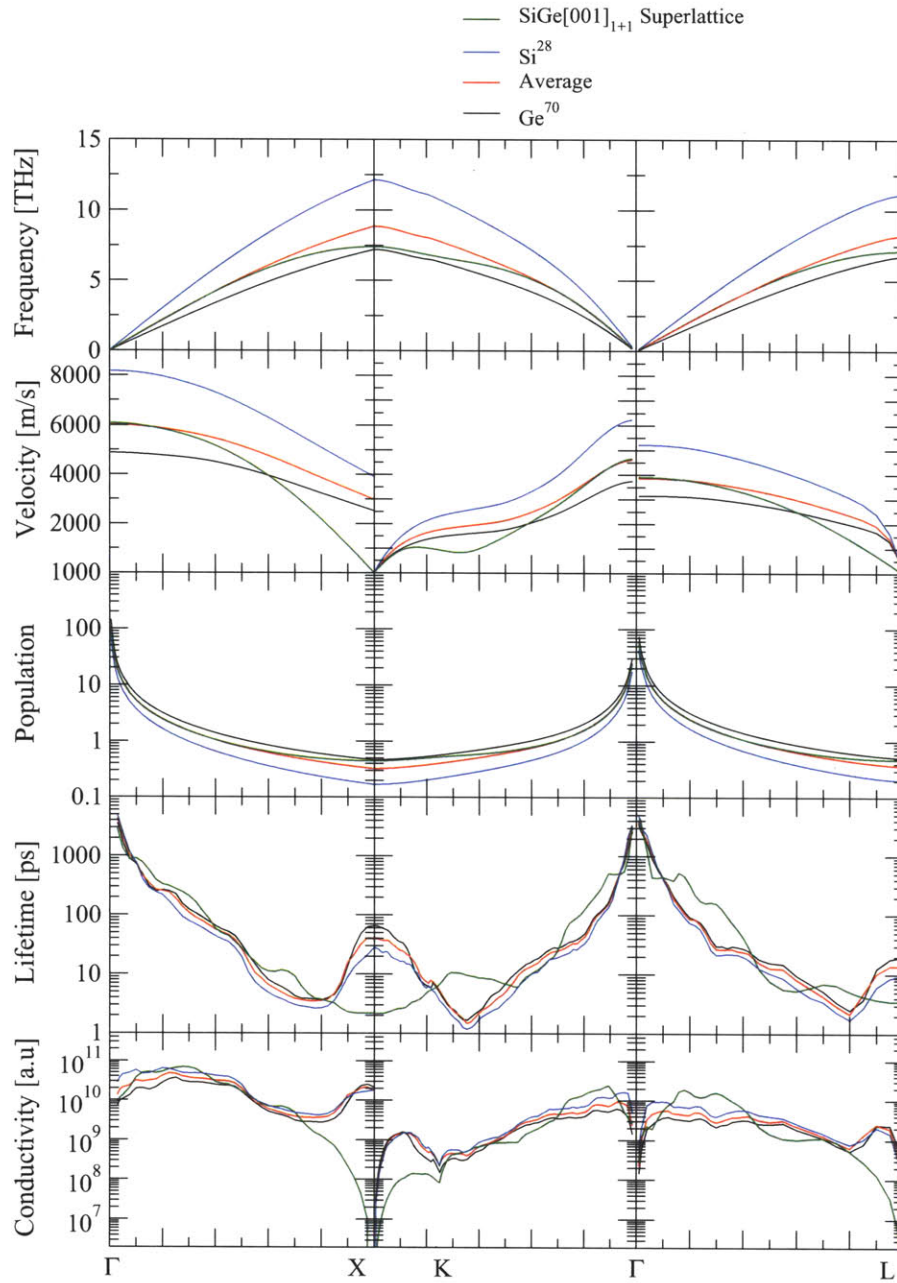
Figure 5-14: Comparison of the longitudinal acoustic modes between Si^{28}, Ge^{70}, average and $SiGe[001]_{1+1}$ superlattice, in terms of their phonon frequencies, group velocities, populations, relaxation times and contributions to thermal conductivity.
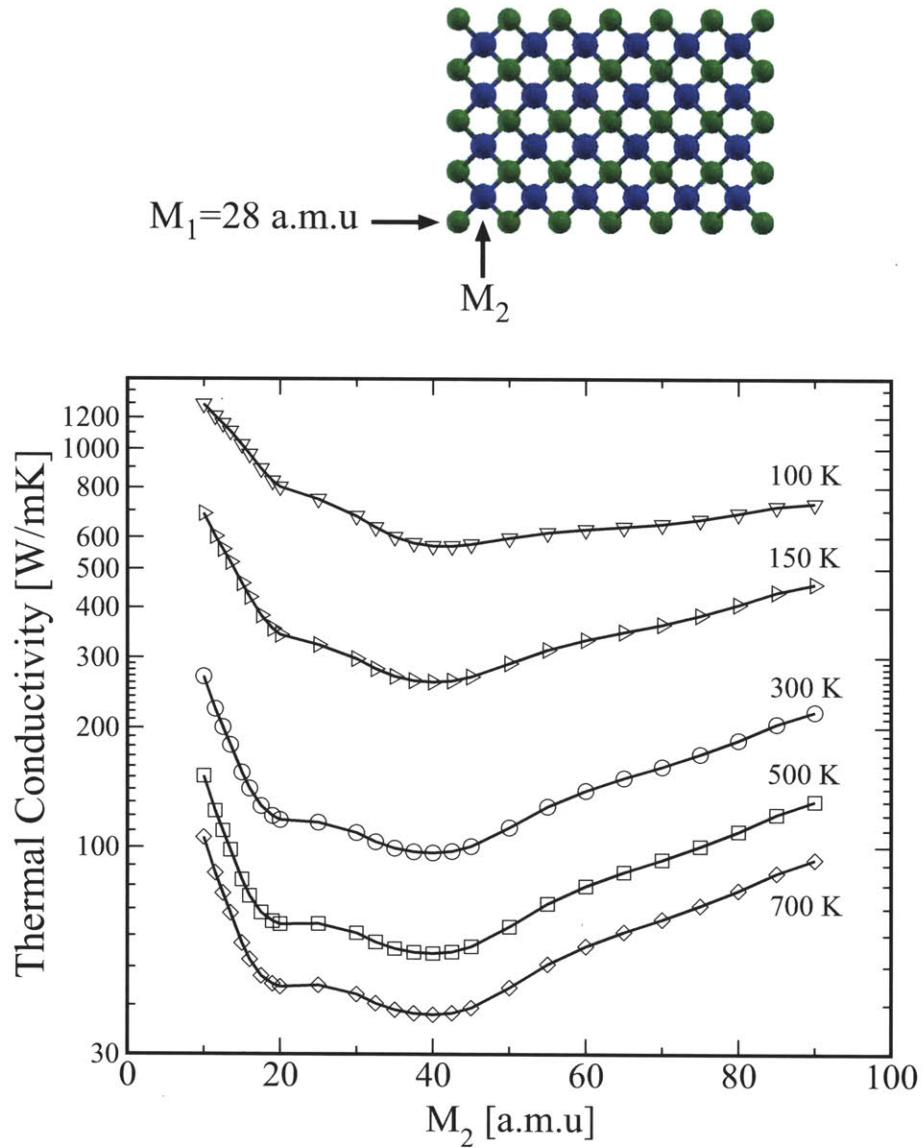
Figure 5-15: Variation of the thermal conductivity of the SiGe[001]$_{1+1}$ superlattice with magnitude of mass mismatch between the two atoms in the unit cell. The mass of one atom in the unit cell is fixed to be that of silicon, while the mass of the second atom is varied. Increasing the mass mismatch beyond that in the Si/Ge superlattice leads to further increase in thermal conductivity.

125
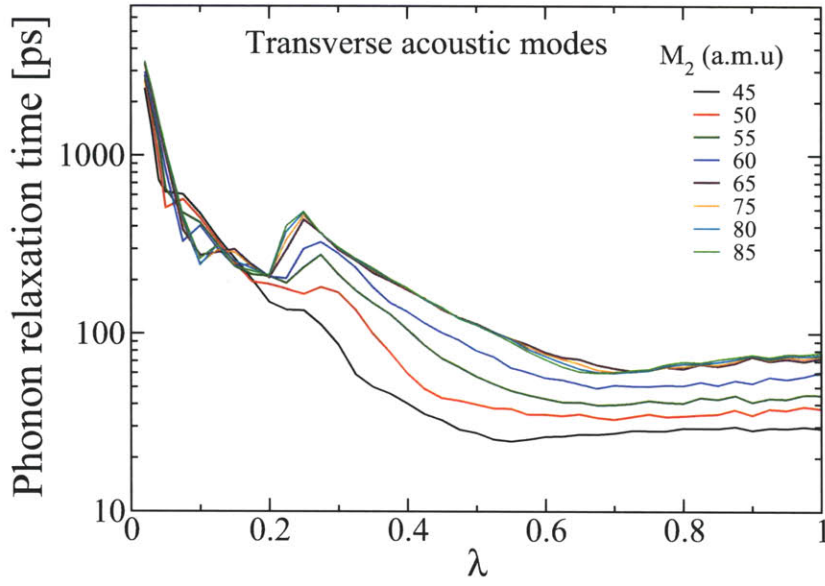
Figure 5-16: Variation of the relaxation time of transverse acoustic modes at 300 K along Γ-X $(0,0,\lambda)$ with increase in mass-mismatch between the two atoms in the unit cell ($M_1 = M_{Si} = 28.0$ a.m.u and M_2 is varied).
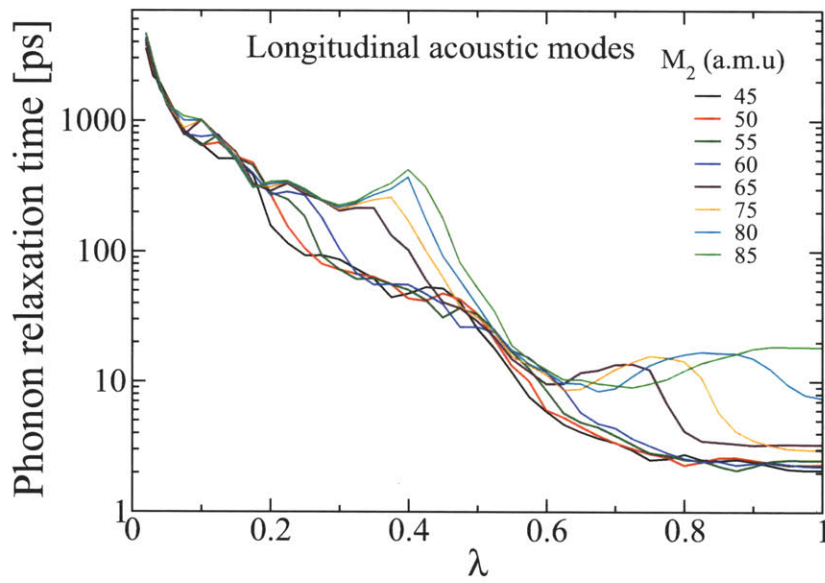
Figure 5-17: Variation of the relaxation time of longitudinal acoustic modes at 300 K along Γ-X $(0,0,\lambda)$ with increase in mass mismatch between the two atoms in the unit cell ($M_1 = M_{Si} = 28.0$ a.m.u and M_2 is varied).

Chapter 6

Conclusions

An accurate prediction of thermal conductivity is important for many applications, such as thermal management of microelectronics and nanoelectronics as well as for for higher energy conversion efficiency in thermoelectric devices. The most important inputs required to predict thermal conductivity accurately are the second-order and third-order interatomic force constants. Typically these are derived from empirical potentials, which are unable to produce the correct anharmonic behaviour, thereby limiting their ability to predict thermal conductivity.

In this thesis we presented a first-principles approach based on the use of density-functional perturbation theory to predict thermal conductivity in bulk, disordered and nanostructured materials. Density-functional perturbation theory as implemented in the Quantum-ESPRESSO package was used to estimate the second-order and third-order interatomic force constants. Thermal conductivity was then computed by solving the phonon Boltzmann equation (PBE). By separately estimating the contribution of each scattering channel to the scattering rate of a phonon mode, this approach provided the ability to acquire a very detailed understanding of the scattering processes that determine thermal conductivity at different length scales. Such an understanding is of fundamental importance in the ability to engineer materials with desired thermal conductivity.

We first applied this approach to estimate the thermal conductivity of isotopically pure silicon (Si^{28}) and germanium (Ge^{70}). The thermal conductivity was first com-

puted by solving the phonon Boltzmann equation in the single-mode relaxation time approximation (SMRT), and later the Boltzmann equation was also solved exactly using a self-consistent solution based on an iterative procedure developed by Omini and Sparavigna [30]. The predicted thermal conductivities were found to be in good agreement with experimentally measured values, with a disagreement of about 15% at 300 K. Our results agreed closely with the previous work of Broido [29]. In isotopically pure silicon it was found that transverse acoustic modes contribute about 62% and longitudinal acoustic modes contribute about 32% of the thermal conductivity at 300 K. These estimates are significantly different from the values predicted by molecular dynamics simulations based on the use of an empirical potential [21] and this result clearly outlines the importance of a first-principles approach for accurate predictions of thermal conductivity. Another significant advantage of this approach lies in the explicit calculation of the phonon frequencies, group velocities, populations and relaxation times to compute thermal conductivity. This allows to extract additional information, such as the dependence of thermal conductivity on phonon mean free paths. In Si^{28} it was found that more than 50% of the heat was conducted by phonons of mean free path longer than 200 nm, providing avenues to lower thermal conductivity through nanostructuring.

In silicon-germanium alloys, it was found that the thermal conductivity could not be computed using phonon modes of the supercell with random distributions of silicon and germanium masses. Such an approach fails to predict thermal conductivity because the group velocities decrease with the increase in supercell size due to more long range disorder being incorporated, leading to zero thermal conductivity in the thermodynamic limit. In this work, we presented another approach to compute alloy thermal conductivity at any composition, based on the idea first proposed by Abeles [39] in 1963, where the disordered crystal is replaced with an ordered one and thermal conductivity is computed using the phonon modes of the ordered crystal. For any composition Si_xGe_{1-x} the mass of an atom in this ordered crystal is taken to be a linear interpolation between the masses of Si and Ge, and the interatomic force constants are quadratically interpolated between those of Si, virtual crystal at

$x = 0.5$, and Ge. The potential of an atom in the virtual crystal is the average of the potentials of Si and Ge. Both disorder and anharmonicity are then treated as perturbations from the ordered crystal. The scattering rates of phonons due to mass-disorder were computed using the analytic perturbation theory [77] and first-principles results, while the anharmonic scattering rates were computed using density-functional perturbation theory for three-phonon scattering processes. This approach predicted more than an order of magnitude drop in thermal conductivity of silicon-germanium alloys compared with silicon, in excellent agreement with experimentally measured values.

The predictive power of first-principles calculations allowed to lay out design rules for low thermal conductivity materials, of central importance for applications in ther-moelectrics. For example, we showed that at 300 K most of the heat is conducted by phonons with mean free paths around 1 μm (60% between 0.2 and 3 μm). Additional scattering mechanisms introduced by the presence of grain boundaries or nanoparti-cles distributed around these optimal values can thus reduce the phonon mean free path and the thermal conductivity below the bulk alloy value. This result is sup-ported by experimental measurements made by Rowe *et al.* [40], who showed that introduction of grain boundaries can reduce the thermal conductivity of SiGe alloys by as much as $\sim 28\%$. Similarly, it was found that addition of only about 12% Ge to Si is sufficient to lower the thermal conductivity to the minimum value achievable in this binary system. This is of central importance to develop low-cost thermoelectric devices.

The first-principles approach was next applied to predict thermal conductivity in nanostructured materials such as superlattices where thermoelectric figure of merit (ZT) significantly higher than bulk materials has been measured. Thermal conduc-tivity was computed using the same approach as for isotopically pure silicon, with one main difference: the interatomic force constants were obtained by using the virtual crystal where the atomic potential at each site is the average of the silicon and germa-nium potentials. The phonon modes of the superlattice unit cell (which varies with the superlattice period) were used to compute the phonon frequencies, group veloci-

129

ties, Bose-Einstein populations and relaxation times which together yielded the thermal conductivity. In this work we ignored the roughness at the interfaces and treated them as perfectly planar. At small superlattice periods, the thermal conductivity was found to decrease sharply with increase in period and then reached a constant value at larger periods. The cross-plane thermal conductivity of the SiGe[001]$_{14+14}$ superlattice with a period of 28 atomic layers (where Si and Ge constitute the alternate layers in the superlattice, [001] represents the growth direction and the subscript $i + f$, here $14 + 14$, represents i atomic layers of Si and f atomic layers of Ge in one period of the superlattice) was computed to be about 13 W/mK, more than an order of magnitude lower than that of silicon. In our work, this sharp drop in thermal conductivity was found to be due to a decrease in phonon group velocity, in good agreement with the results of Tamura [84] and Hyldgaard and Mahan [46]. Furthermore, comparison with experimentally measured values shows that roughness present at the interfaces results in a further order of magnitude decrease in the thermal conductivity.

In the limit of very small superlattice period, we find the thermal conductivity to increase dramatically. The thermal conductivity of the SiGe[001]$_{1+1}$ superlattice was computed to be 160 W/mK at 300 K. The average of the cross-plane and in-plane thermal conductivity of the SiGe[001]$_{2+2}$ was obtained to be 55 W/mK. Thus reducing the superlattice period from 4 atomic layers to 2 atomic layers resulted in an increase in thermal conductivity by almost a factor of 3. More intriguingly, the computed thermal conductivity of the SiGe[001]$_{1+1}$ superlattice was found to exceed even that of isotopically pure silicon (Si^{28}) by almost 20%. This is surprising because the presence of heavier Ge in the superlattice leads to lower frequencies and lower group velocities than in pure silicon and should therefore result in lower thermal conductivity. Our approach provides an understanding of the processes that lead to the observed enhancement in thermal conductivity.

As the superlattice period is decreased, the phonon modes are able to tunnel through the short range variations in mass, resulting in an increase in group velocity and a corresponding increase in thermal conductivity. However, this alone cannot not explain the thermal conductivity of SiGe[001]$_{1+1}$ superlattice. To demonstrate this

more explicitly we compared SiGe[001]$_{1+1}$ superlattice with an average material where the mass of each atom was taken to be an average of Si and Ge masses. The thermal conductivity of this average material was computed to be 84 W/mK at 300 K. Below 5 THz where most of the heat conduction occurs, the phonon group velocities in the two materials (superlattice and average) were found to equal and lower than in silicon. Based on the group velocity arguments alone the thermal conductivity of SiGe[001]$_{1+1}$ superlattice is expected to be the same as that of the average material and lower than silicon. However, results presented above are contrary to such an expectation and therefore group velocity increase cannot completely explain the observed thermal conductivity behavior.

The large enhancement in thermal conductivity at small superlattice period was found to be due to a dramatic decrease in the scattering of acoustic phonons and a corresponding increase in their relaxation times. This decrease in scattering rates of acoustic phonons occurs due to a large gap between the frequencies of optical and acoustic phonons in the SiGe[001]$_{1+1}$ superlattice. In pure silicon and germanium, a dominant scattering mechanism for low energy transverse acoustic modes involves absorbing another acoustic mode to yield a higher energy optical phonon mode. For the above scattering process to be feasible, the sum of the phonon frequencies of the two acoustic modes has to be equal to the frequency of the optical mode ($\omega(TA) + \omega(A) = \omega(O)$). In the SiGe[001]$_{1+1}$ superlattice, however, the large separation between the optical and acoustic phonon mode frequencies leads to the frequency of the optical mode being typically larger than the sum of the frequencies of the relevant acoustic modes ($\omega(O) > \omega(TA) + \omega(A)$), and the above scattering channel is not feasible in this system. This eliminates a dominant scattering mechanism for transverse acoustic modes and leads to a large reduction in their scattering rates with a corresponding increase in their relaxation times. At the Brillouin zone edge the phonon relaxation times of transverse acoustic modes in SiGe[001]$_{1+1}$ superlattice were computed to be almost five times higher than in silicon at 300 K. This increase in phonon relaxation times of the acoustic modes leads to the observed enhancement in the thermal conductivity of SiGe[001]$_{1+1}$ superlattice.

131

Finally we explored the possibility of engineering this high thermal conductivity by varying the mass-mismatch between the two materials in SiGe[001]$_{1+1}$ superlattice. The unit cell of this superlattice is the fcc unit cell with the two atom basis. We fixed the mass of one atom in the superlattice unit cell to be that of silicon and computed the thermal conductivity as a function of the mass of second atom. It was found that as the mass-difference is increased beyond that in the SiGe superlattice, the thermal conductivity increases further. These results suggest the possibility of designing materials with high thermal conductivity and could have useful implications for thermal management of electronics.

Bibliography

[1] G. Chen, Annual Review of Heat Transfer **7**, 1 (1996).

[2] G. Chen, S. Volz, T. Borca-Tasciuc, T. Zeng, T. Zeng, D. Song, K. L. Wang, and M.S. Dresselhaus, Mater. Res. Soc. **545**, 357 (1998).

[3] A. Bar-Cohen, P. Wang, and E. Rahim, Microgravity Science and Technology **19**, 48 (2007).

[4] iNEMI, Electronics Manufacturing Initiative Technology Roadmap, http://www.nemi.org (2006).

[5] D. M. Rowe, .In: Rowe, D. M. (Ed.), CRC Thermoelectrics Handbook, Macro to Nano, CRC Press, Boca Raton, FL (2006).

[6] S.K. Bux, R.G. Blair, P.K. Gogna, H. Lee, G. Chen, M.S. Dresselhaus, R.B. Kaner, and J. Fleurial, Adv. Funct. Mater. **19**, 2445 (2009).

[7] C. B. Vining, W. Laskow, J. O. Hanson, R. R. Van der Beck, and P. D. Gorsuch, J. Appl. Phys. **69**, 4333 (1991).

[8] M.S. Dresselhaus, G. Chen, M.Y. Tang, R. Yang, H. Lee, D. Wang, Z. Ren, J. Fleurial, and P. Gogna, Adv. Mater. **19**, 1043 (2007).

[9] A. I. Hochbaum, R. Chen, R. D. Delgado, W. Liang, E. C. Garnett, M. Najarian, A. Majumdar, and P. Yang, Nature **451**, 163 (2008).

[10] A. I. Boukai, Y. Bunimovich, J. Tahir-Kheli, J. Yu, W. A. Goddard, and J. R. Heath, Nature **451**, 168 (2008).

[11] R. Venkatasubramanian, E. Siivola, T. Colpitts, and B. O'Quinn, Nature **43**, 597 (2001).

[12] W. Kim, J. Zide, A. Gossard, D. Klenov, S. Stemmer, A. Shakouri, and A. Majumdar, Phys. Rev. Lett. **96**, 045901 (2008).

[13] A. Debernardi, S. Baroni, and E. Molinari, Phys. Rev. Lett. **75**, 1819 (1995).

[14] S. Baroni, P. Giannozzi, and A. Testa, Phys. Rev. Lett. **58**, 1861 (1987).

[15] X. Gonze, Phys. Rev. A **52**, 1086 (1995).

[16] J. M. Ziman, Electrons and Phonons, Oxford University Press, London (1960).

[17] D. A. Broido, A. Ward, N. Mingo, Phys. Rev. B **72**, 014308 (2005).

[18] F. H. Stillinger and T. A. Weber, Phys. Rev. B **31**, 5262 (1985).

[19] J. Tersoff, Phys. Rev. B **38**, 9902 (1988).

[20] J. F. Justo, M. Z. Bazant, E. Kaxiras, V. V. Bulatov, and S. Yip, Phys. Rev. B **58**, 2539 (1998).

[21] A. S. Henry and G. Chen, J. Comput. Theor. Nanosci. **5**, 1 (2008).

[22] R Peierls, Ann. Phys. **3**, 1055 (1929).

[23] P. Giannozzi, S. de Gironcoli, P. Pavone, and S. Baroni, Physical Review B **43**, 7231 (1991).

[24] S. Narasimhan and D. Vanderbilt, Phys. Rev. B **43**, 4541 (1991).

[25] P. N. Keating, Phys. Rev. **145**, 637 (1966).

[26] X. Gonze and J. -P. Vigneron, Phys. Rev. B **39**, 13120 (1989).

[27] G. Lang, K. Karch, M. Schmitt, P. Pavone, A. P. Mayer, R. P. Wehner, and D. Strauch, Phys. Rev. B **59**, 6182 (1999).

[28] G. Deinzer, G. Birner, and D. Strauch, Phys. Rev. B **67**, 144304 (2003).

[29] D. A. Broido, M. Malorny, G. Birner, N. Mingo, and D. A. Stewart, Appl. Phys. Lett. **91**, 231922 (2007).

[30] M. Omini and A. Sparavigna, Phys. Review B **53**, 9064 (1996).

[31] A. Ward, D. A. Broido, D. A. Stewart, and G. Deinzer, Phys. Rev. B **80**, 125203 (2009).

[32] P. Giannozzi, S. Baroni, N. Bonini, M. Calandra, R. Car, C. Cavazzoni, D. Ceresoli, G. L. Chiarotti, M. Cococcioni, I. Dabo, A. Dal Corso, S. de Gironcoli, S. Fabris, G. Fratesi, R. Gebauer, U. Gertsmann, C. Gougoussis, A. Kokalj, M. Lazzeri, L. Martin-Samos, N. Marzari, F. Mauri, R. Mazzarello, S. Paolini, A. Pasquarello, L. Paulatto, C. Sbraccia, S. Scandolo, G. Sclauzero, A. P. Seitsonen, A. Smogunov, P. Umari and R. M. Wentzcovitch, J. Phys.: Condens. Matter **21**, 395502 (2009); http://www.quantum-espresso.org

[33] A. Skye and P. K. Schelling, J. Appl. Phys. **103**, 113524 (2008).

[34] P. C. Weakliem and E. A. Carter, Phys. Rev. B **45**, 13458 (1992).

[35] S. de Gironcoli, P. Giannozzi, and S. Baroni, Phys. Rev. Lett. **66**, 2116 (1991).

[36] H. Stohr and W. Klemm, Z. Anorg. Allgem. Chem. **241**, 305 (1954).

[37] A. M. Toxen, Physical Review **122**, 450 (1961).

[38] B. Abeles, D. S. Beers, G. D. Cody, and J. P. Dismukes, Physical Review **125**, 44 (1962).

[39] B. Abeles, Physical Review **131**, 1906 (1963).

[40] D. M. Rowe, V. S. Shukla and N. Savvides, Nature **290**, 765 (1981).

[41] S. M. Lee, D. G. Cahill, and R. Venkatasubramanian, Appl. Phys. Lett. **70**, 2957 (1997).

[42] H. Lee, Master's Thesis, Massachusetts Institute of Technology, (2005).

[43] L. Nordheim, Ann. Phys. (Leipzig) **9**, 607 (1931).

[44] N. Marzari, S. de Gironcoli and S. Baroni, Phys. Rev. Lett. **72**, 4001 (1994).

[45] G. Chen, Journal of Heat Transfer **119**, 220 (1997).

[46] P. Hyldgaard and G.D. Mahan Physical Review B **56**, 10754 (1997).

[47] P. Hohenberg and W. Cohen, Phys. Rev. **136**, B864 (1964).

[48] W. Kohn and L.J. Sham, Phys. Rev. A **140**, 1133 (1965).

[49] X. Gonze, and J.P. Vigneron, Phys. Rev. **96**, 951 (1989).

[50] R.M. Sternheimer, Phys. Rev. B. **39**, 13120 (1954).

[51] G. P. Srivastava, The Physics of Phonons Taylor and Francis Group, New York (1990).

[52] R Peierls, Quantum Theory of Solids, Clarendon Press, Oxford (1955).

[53] P. A. M. Dirac, Proc. Roy. Soc. (London) **A114**, 243 (1927).

[54] E. Fermi, Nuclear Physics, University of Chicago Press (1950).

[55] M. Asen-Palmer, K. Bartkowski, E. Grmelin, M. Cardona, A. P. Zhernov, A. V. Inyushkin, A. Taldenkov, V. I. Ozhogin, K. M. Itoh, and E. E. Haller, Phys. Rev. B **56**, 9431 (1997).

[56] G. P. Srivastava, Pramana **3**, 209 (1974).

[57] J. X. Cao, X. H. Yan, Y. Xiao, and J. W. Ding, Phys. Rev. B **69**, 073407 (2004).

[58] A. Khitun and K. L. Wang, Appl. Phys. Lett. **79**, 851 (2001).

[59] H. J. Monkhorst and J. D. Pack, Phys. Rev. B **13**, 5188 (1976).

[60] A. Dal Corso, S. Baroni, R. Resta, and S. de Gironcoli, Phys. Rev. B **47**, 3588 (1993).

[61] J. Menéndez and M. Cardona, Phys. Rev. B **29**, 2051 (1984).

[62] A. V. Inyushkin, A. N. Taldenkov, A. M. Cibin, A. V. Gusev, and H.-J. Pohl, Phys. Status Solidi C **1**, 2995 (2004).

[63] V. I. Ozhogin, A. V. Inyushkin, A. N. Taldenkov, A. V. Tikhomirov, and G. E. Popov, JETP Lett. **63**, 490 (1996).

[64] R. Hamilton and J. Parrot, Phys. Rev. **178**, 1284 (1969).

[65] N. Savvides and H.J. Goldsmid, J. Phys. **C6**, 1701 (1973).

[66] Y. Ju and K. Goodson, Appl. Phys. Lett. **74**, 3005 (1999).

[67] S. Uma, A. D. McConnell, M. Asheghi, K. Kurabayashi, and K. E. Goodson, Int. J. Thermophysics **22**, 605 (2001).

[68] G. Joshi, H. Lee, Y. Lan, X. Wang, G. Zhu, D. Wang, R. W. Gould, D. C. Cuff, M. Y. Tang, M. S. Dresselhaus, G. Chen, and Z. Ren, Nano Lett. **8**, 4670 (2008).

[69] C. Uher, J. Yang, S. Hu, D. T. Mortelli, and G. P. Meisner, Phys. Rev. B **59**, 8615 (1999).

[70] A. Chaudhuri, A. Kundu, D. Roy, A. Dhar, J.L. Lebowitz, and H. Spohn, Phys. Rev. B. **81**, 064301 (2010).

[71] P. B. Allen and J. L. Feldman, Phys. Review B **48**, 12581 (1993).

[72] J. R. de Laeter, J. K. Bohlke, P. De Bievre, H. Hidaka, H. S. Peiser, K. J. R. Rosman, and P. D. P. Taylor, Pure. Appl. Chem. **75**, 683 (2003).

[73] S. Baroni, S. de Gironcoli, and P. Giannozzi, Phys. Rev. Lett. **65**, 84 (1990).

[74] S. de Gironcoli, Ph.D. Thesis, Lausanne EPFL, (1992).

[75] P.A. Lee and T.V. Ramakrishnan, Review of Modern Physics **57**, 287 (1985).

[76] P. G. Klemens, Proc. Phys. Soc. (London) **A68**, 1113 (1955).

[77] S. Tamura, Phys. Rev. B **27**, 858 (1983).

[78] W. A. Kamitakahara and B. N. Brockhouse, Phys. Rev. B **10**, 1200 (1974).

[79] D. J. Ecsedy and P. G. Klemens, Phys. Rev. B **15**, 5957 (1977).

[80] D. G. Cahill, Rev. Sci. Instrum. **61**, 802 (1990).

[81] S. Yuan Ren and J.D. Dow, Physical Review B **25**, 3750 (1982).

[82] A. Majumdar, Journal of Heat Transfer **115**, 7 (1993).

[83] G. Chen, Physical Review B **57**, 14958 (1998).

[84] S. Tamura, Y. Tanaka, and H. J. Maris, Physical Review B **60**, 2627 (1997).

[85] M. V. Simkin and G. D. Mahan, Physical Review Letters **84**, 927 (1999).

[86] S. Tamura, D. C. Hurley, and J. P. Wolfe, Physical Review B **38**, 1427 (1988).

[87] G. Chen, Journal of Heat Transfer **121**, 945 (1999).

[88] B. Yang and G. Chen, Phys. Rev. B **67**, 195311 (2003).

[89] S. Ren, W. Cheng, and G. Chen, Journal of Applied Physics **100**, 103505 (2006).